

**Development of a multi-wavelength lensless digital holography
system for 3D deformations and shape measurements of
tympanic membranes**

A Thesis
Submitted to the faculty of the

Worcester Polytechnic Institute

as a partial fulfillment of the requirements for the
Degree of Master of Science
in
Mechanical Engineering
by

Weina Lu

Weina Lu

15 March, 2012

Approved:

Cosme Furlong-Vazquez

Prof. Cosme Furlong-Vazquez, Major Advisor

Allen H. Hoffman

Prof. Allen H. Hoffman, Member, Thesis Committee

Ryszard J. Pryputniewicz

Prof. Ryszard J. Pryputniewicz, Member, Thesis Committee

John J. Rosowski

Prof. John J. Rosowski, Mass. Eye & Ear Infirmary, Harvard-MIT Div. of Health
Science and Technology, Member, Thesis Committee

John J. Blandino

Prof. John J. Blandino, Graduate Committee Representative

Copyright © 2012

by

NEST- NanoEngineering, Science, and Technology
CHSLT-Center for Holographic Studies and Laser micro-mechaTronics
Mechanical Engineering Department
Worcester Polytechnic Institute
Worcester, MA 01609-2280

Abstract

Current methodologies for characterization of tympanic membranes (TMs) have some limitations. They: are qualitative rather than quantitative, consist of single point mobility measurements, or only include one-dimensional deformation measurements. Furthermore, none of the current clinical tools for diagnosis of hearing losses have the capability to measure the shape of TM, which is very useful for anatomical or pathological investigations.

The multi-wavelength lensless digital holography system (MLDHS) reported in this work consists of laser delivery (LD), optical head (OH), and computing platform (CP) subsystems, with capabilities of real-time, non-contact, full-field of view measurements. One version of the LD houses two tunable near-infrared external-cavity diode lasers with central wavelengths of 780.24nm and 779.74nm respectively, an acousto-optic modulator, and a laser-to-fiber mechanism. The output of the LD is delivered to an ultra-fast MEMS-based fiber optic switch and the light beam is directed to the OH, which is arranged to perform imaging and measurements by phase-shifting holography. The second LD version subsystem contains one tunable near-infrared diode laser in the range from 770nm to 789nm, an anamorphic prism pair, an acousto-optic modulator, a half-wave plate, and a fiber coupler assembly. The output of the LD is delivered to the OH directly. The OH is designed by 3D optical ray tracing simulations in which components are rotated at specific angles to overcome reflection issues. A high-resolution digital camera with pixel size of $6.7\mu\text{m}$ by $6.7\mu\text{m}$ in the OH is used for image recording at high-rates while the CP acquires and processes images in either time-averaged or double-exposure modes. The choice of working version depends on the requirements of the measurement and the sample under test.

MLDHS can obtain shape and one-dimensional deformations along one optical axis (z -axis). In order to recover 3D deformations, assumptions based on elasticity theory are prerequisites for the calculations: (a) the TM is analyzed as a thin shell; (b) shape before and after deformation is considered nearly the same since acoustic pressure typically introduces nanometer scale deformations; and (c) normal vectors remain perpendicular to the deformed mid-plane of the TM.

Another part of this Thesis is the design and prototyping of the MLDHS, which translates this holographic platform into a simple and compact holographic instrument for measurements of the visible tympanic-membrane motions in live patients. Therefore, the OH subsystem needs to be light and portable, as it can be mounted on a robotic arm near the ear canal, while the LD subsystem needs to be stable and safely protected.

Preliminary results of acoustically induced 3D deformations and shape measurements by a single instrument that demonstrate the capabilities of the devices developed in this Thesis are presented.

The Thesis is dedicated proudly to my family.

Acknowledgements

At this time, it is extremely important to extend my gratitude to a number of individuals and organizations which have aided me and made it possible for me to arrive at this moment with these results.

Most important, I'm very grateful for all the support and friendship, which were offered to me by my advisor Professor Cosme Furlong, for his patience, motivation, enthusiasm, and immense knowledge. Besides, I would like to show my gratitude to my thesis committee, who has demonstrated unwavering support during my thesis research, and the Center for Holographic Studies and Laser micromechaTronics (CHSLT) in WPI Mechanical Engineering Department, for the use of both their facilities and equipment, deserve much praise and recognition.

I wish to acknowledge the assistance of Professor John J. Rosowski and Dr. Jeffrey T. Cheng for their collaboration, advice and suggestions in my experimental work. Funding and support from Dr. Saumil Merchant and his generous patients at Massachusetts Eye and Ear Infirmary were extremely important in the project as well.

Accolades are also extended to Dr. Jorge M. Flores, Ellery Harrington, Ivo Dobrev, and Peter Hefti from the CHSLT laboratories for their enduring support and invaluable assistance.

Finally, but not the least, I would like to thank my parents, Huaiyu Lu and Xiaochun Li, for their love and unending support during my study over the past couple of years and more. Without them I would not have been able to accomplish anything.

Table of Contents

Abstract.....	ii
Acknowledgements.....	v
List of Figures.....	ix
List of Tables.....	xiv
Nomenclature.....	xv
Objective.....	xix
1 Introduction.....	1
1.1 Anatomy of the ear.....	1
1.1.1 Function of the tympanic membrane.....	2
1.1.2 Physical Characteristics of the Tympanic Membrane.....	4
1.1.3 Histology of the Tympanic Membrane.....	5
2 Significance of 3D deformations and shape measurements on human tympanic membranes.....	10
3 Optical techniques of deformation and shape measurements of tympanic membranes.....	11
3.1 Moiré topography.....	11
3.2 Laser Doppler vibrometer.....	15
3.3 Holographic interferometry.....	18
4 Digital optoelectronic holography system developed by WPI-MEEI.....	21
4.1 Fringe-locus function.....	21
4.2 Holographic interferometry modes of operation.....	24
4.2.1 Time-averaged mode.....	25
4.2.2 Double-exposure mode.....	26
4.3 Hardware.....	27
4.4 Software.....	30
4.4.1 LaserView.....	30
4.4.2 HoloStudio.....	32

4.5	Representative experimental results.....	34
4.6	Limitations	37
5	Theory of multi-wavelength lensless digital holography system	38
5.1	Shape measurements	38
5.1.1	Two-wavelength technique.....	38
5.1.2	Multi-wavelength technique	40
5.2	Out-of-plane deformation measurements.....	41
5.2.1	Fundamentals of thin shells	42
5.2.2	Main proposed approach	43
5.2.3	Validation of the proposed approach.....	45
5.2.4	Accuracy of the proposed approach	52
5.2.5	Effect of thickness on this thin shell formulation.....	54
6	Development of multi-wavelength lensless digital holography: experimental verifications	58
6.1	Laser delivery system.....	60
6.1.1	1 st version.....	61
6.1.2	2 nd version.....	72
6.1.3	Comparison of laser delivery systems	74
6.2	Optical head system	75
6.2.1	1 st generation.....	76
6.2.2	2 nd generation.....	78
6.2.3	Cameras	83
7	Sample preparation	85
7.1	Coating materials.....	85
7.2	Spectrometer.....	86
7.3	Multi-wavelength lensless digital holography system	91
8	Deformations and shape measurements	95
8.1	Measurements on artificial samples	95
8.2	In-vitro measurements on chinchilla tympanic membrane	99
9	Conclusions and future work.....	113

10 References 114

List of Figures

Fig. 1.1. Anatomy of the human ear: the cross section of human ear showing divisions of the outer, middle, and inner ears (Wikipedia, 2008).....	1
Fig. 1.2. Middle ear ossicles: (a) chain of ossicles and their ligaments, (b) the three bones: malleus (M) incus (I) and stapes (S) (Csillag, 2005).	2
Fig. 1.3. TM to stapes area ratio (Schubert, 1980).	3
Fig. 1.4. Human TM showing two parts (Wajnberg, 1987).....	4
Fig. 1.5. Relative sizes of mammalian TMs (Chole and Kodama, 1989).....	5
Fig. 1.6. Two sections of human TM: Upper - Pars Flaccida, and Lower - Pars Tensa (Lim, 1995).	6
Fig. 1.7. Artist's conception of the migrating pattern of the epidermis in the TM of humans and guinea pigs (Lim 1995).....	8
Fig. 1.8. A SEM photomicrograph of the outer radial and inner circular fibers and the parabolic fibers in the fibrous layer of the pars tensa (Lim, 1995).....	9
Fig. 1.9. Artist's conception of the fiber arrangement of the human TM. SP: short process of the malleus; U: umbo; TIR: trigonum interradiale; C: circular fibers; R(1): radial fibers which attach straight into the annular ring; R(2): a few radial fibers which cross paths; T: transverse fibers; P: parabolic fibers; SMR: sub-mucous fine radial fibers (Lim, 1995).....	9
Fig. 3.1. Schematic representation of classic shadow moiré apparatus: SM is the stage mount, TS is the translation stage, PM is the positioning mount, O is the object, G is the grating, LG is the light guide and C is the camera, (Dirckx and Decraemer 1991).....	12
Fig. 3.2. Schematic representation of classic projection moiré apparatus: G is the grating and L is the lens, (Dirckx and Decraemer 2000).	14
Fig. 3.3. Single-point LDV measurements of the TM, (Rosowski et al., 2008).....	16
Fig. 3.4. Classic holography setup, (Khanna and Tonndorf, 1972).	19
Fig. 4.1. Illumination and observation geometry for holographic interferometry: Rp, R1, and R2 are the position vectors whereas K1 and K2 are the illumination and the observation vectors, respectively. K is the sensitivity vector, (Hulli, 2008).....	22
Fig. 4.2. Optoelectronic-mechanical components of DOEHS deployed at the Massachusetts Eye and Ear Infirmary (MEEI): (1) the laser delivery (LD) system, (2) otoscope head (OH) system, and (3) mechatronic otoscope positioner (MOP), (Dobrev et al., 2010; Harrington et al., 2010; Dobrev et al., 2011; Harrington et al., 2011).....	28

Fig. 4.3. Schematic of DOEHS: (1) LD system and (2) OH system.	29
Fig. 4.4. Screenshot of LaserView’s main window, with descriptions of its primary features, (Harrington et al., 2011).....	31
Fig. 4.5. HoloStudio interface with color map applies to unwrapped phase, with descriptions of its primary features, (Harrington et al., 2011).....	33
Fig. 4.6. Schematic of the illumination system.....	34
Fig. 4.7. Experimental configuration of OH system and object of human temporal bone.	35
Fig. 4.8. The deformation of medial side of TM of phase 180° at sound excitation of 1 kHz: (a) modulation image, and (b) optical phase with location of umbo marked.	35
Fig. 4.9. Representative deformations of medial side of TM at sound excitation of 1 kHz, from phase 0 to $7\pi/4$	36
Fig. 5.1. The algorithm used to extract 3D deformations by measurements of shape and only one component of deformation.	44
Fig. 5.2. Configuration of decompositions of the resultant deformation and the normal vector. \mathbf{U} is the resultant deformation; \mathbf{Ux} , \mathbf{Uy} and \mathbf{Uz} are the decompositions of \mathbf{U} along x , y and z axes; \mathbf{n} is the normal vector; \mathbf{nx} , \mathbf{ny} and \mathbf{nz} are the decompositions of \mathbf{n} along x , y and z axes; α , β and γ are the angles between the direction of \mathbf{U} or \mathbf{n} and x , y , z axes.	44
Fig. 5.3. The flow chart of the validation approach that was applied.....	46
Fig. 5.4. 2D geometries of (a) ideal partial spherical object, and (b) TM model.	47
Fig. 5.5. FEA solutions for modal analysis of the 4th mode of vibration of an ideal object: (a) x -axis deformation (\mathbf{Ux}), (b) y -axis deformation (\mathbf{Uy}), (c) z -axis deformation (\mathbf{Uz}), (d) resultant deformation, and (e) object shape.	47
Fig. 5.6. (a) Predicted deformations in the x direction (\mathbf{Ux}'), and (b) predicted deformations in the y direction (\mathbf{Uy}'). Computed x and y components of deformations obtained by applying proposed approach. Results should be compared with these shown in Figs. 5.5(a) and 5.5(b).	48
Fig. 5.7. Comparisons of deformations between FEA solutions (\mathbf{Ux} , \mathbf{Uy}) and predictions (\mathbf{Ux}' , \mathbf{Uy}') after data normalization.	49
Fig. 5.8. Comparisons of deformations between FEA solutions (\mathbf{Ux} , \mathbf{Uy}) and predictions (\mathbf{Ux}' , \mathbf{Uy}') after data normalization.	51
Fig. 5.9. Normal vectors plot of analytical solution (original length) and Matlab solution (0.8 of original length).	53
Fig. 5.10. FEA solution of deformation along x axis (mode 1) computed by FEM (ANSYS) when the thickness to radius ratio is 1/20.	56
Fig. 6.1. Experimental setup of the multi-wavelength lensless digital holography system.	59

Fig. 6.2. Schematic of the multi-wavelength lensless digital holography system: LDD is the laser diode driver, L is the laser, M is the mirror, AOM is the acousto-optic modulator, FCA is the fiber coupler assembly, OS is the optical switch, C is the collimator, BS is the beam splitter cube, PZT is the piezoelectric transducer, P is the polarizer, NDF is the neutral density filter, CCD is the CCD camera, O is the object, and CP is the computer platform.....	59
Fig. 6.3. Power distribution of Vortex II-TLB 6900 (0055) and Vortex II-TLB 6900 (0078).....	62
Fig. 6.4. Power stability after laser light changed from Vortex II-TLB 6900 (0055) to Vortex II-TLB 6900 (0078) by OS.....	63
Fig. 6.5. Comparison of mirror with protected (a) aluminum, (b) silver, and (c) gold coating.....	64
Fig. 6.6. Power stability of the output beam of AOM.....	65
Fig. 6.7. FCA: product from (a) New Focus, and (b) OZOptics.....	66
Fig. 6.8. (a) Panda style polarized maintaining (PM) fiber from Thorlabs, (b) panda style armored polarized maintaining (PM) fiber from Thorlabs, and (c) style armored polarized maintaining (PM) fiber from OZ Optics.....	67
Fig. 6.9. Configuration of the test that the fiber is not touched by anything.....	67
Fig. 6.10. Configuration of the test that the fiber is touched during the whole test period.....	69
Fig. 6.11. Power stability of the laser beam coming out of the OS.....	70
Fig. 6.12. The laser beam transportation efficiency map of LD system.....	71
Fig. 6.13. 3D CAD model of the LD system package.....	72
Fig. 6.14. Power distribution in 2 nd version of LD system.....	73
Fig. 6.15 Cross-section of laser beam coming out of Velocity: (a) without APP, (b) to (d) with APP and the rotation degree of APP is from 0° to 270°.....	73
Fig. 6.16. Image quality of modulation, optical phase and unwrapped phase (with mask) of each LD system: (a) 1 st version of LD system, (b) only Vertex 0078 used in 1 st version of LD system, and (c) 2 nd version of LD system. Image contrast is shown in upper left side.....	75
Fig. 6.17. CAD model of the polarizing cage style OH system marked with laser beam path.....	76
Fig. 6.18. Interference fringes appear on a coated conical metal object in shape measurements. Laser wavelength of Vortex 0055 is 780.13 nm and laser wavelength of Vortex 0078 is 779.72 nm. Scratches are made for focusing purposes.....	77
Fig. 6.19. Reflection issue on images of two coated conical metal objects in two situations: (a) shape measurement situation, and (b) no fringes situation. Scratches are made for focusing purposes.....	78
Fig. 6.20. CAD model of the non-polarizing OH system.....	79
Fig. 6.21. Comparison of image quality of different rotation degrees.....	80

Fig. 6.22. Ray tracing result of OH system with BS rotated in 14 degree.....	82
Fig. 6.23. First generation of (a) 3D CAD model design and (b) prototype of OH system.	82
Fig. 6.24. Images captured by different cameras: (a) Pike F145, (b) Pike F505, and (c) Pixelink PL-A741-E. From top to bottom, images are modulation, optical phase and unwrapped phase. Image contrast is shown in the upper left side.	84
Fig. 7.1. (a) Chemicals diluted with water, and (b) different chemicals with different concentrations on clear slides.	87
Fig. 7.2. The spectroscopy setup.....	88
Fig. 7.3. Reflectance measurements of six coatings with green laser light.	89
Fig. 7.4. Reflectance measurements of six coatings with yellow laser light.	89
Fig. 7.5. Reflectance measurements of six coatings with orange laser light.	90
Fig. 7.6. Reflectance measurements of six coatings with red laser light.	90
Fig. 7.7. (a) Wax paper, (b) the drawing for creating the conical shaped sample, and (c) the coated conical shaped sample.	92
Fig. 7.8. Optical phase images of convex samples with different coatings. Image contrast is shown after every coating nomination.	93
Fig. 7.9. Optical phase images of concave samples with different coatings. Image contrast is shown after every coating nomination.....	94
Fig. 8.1. Samples tested by MLDHS for shape and deformation measurements.	96
Fig. 8.2. (a) The artificial object with white paint on the convex surface, and (b) the experimental setup.	98
Fig. 8.3. Experimental results at 80.417 kHz: (a) representation of the artificial object shape, (b) displacement measured along optical axis (z axis), (c) predicted displacement in x direction, and (d) predicted displacement in y direction.....	99
Fig. 8.4. Experimental setup for measurements on a chinchilla TM.	100
Fig. 8.5. Holographic images for shape measurements: (a) wrapped phase image, and (b) unwrapped phase image. Fig. (a) shows the location of the manubrium by a white contour.	101
Fig. 8.6. 3D plot of the measured shape. The arrow indicates external side of the TM.	101
Fig. 8.7. Wrapped optical phase of the measured z -axis deformations of different stimulus frequencies at phase π . For orientation, the posterior (Post.), anterior (Ant.), superior (Sup.) and inferior (Inf.) are shown.	103
Fig. 8.8. The resultant, z -axis, x -axis and y -axis deformations of the entire TM of different stimulus frequencies at phase π . The unit of deformations is μm	104
Fig. 8.9. Perspective 3D plots of the instantaneous resultant deformations of the entire TM surface at eight stimulus phases at 800 Hz. The orientation of the TM and the location of the manubrium are shown in the first plot.	106

Fig. 8.10. Perspective 3D plots of the instantaneous deformations of the entire TM surface at eight stimulus phases at 1.5 kHz. The orientation of the TM and the location of the manubrium are shown in the first plot.	107
Fig. 8.11. Perspective 3D plots of the instantaneous deformations of the entire TM surface at eight stimulus phases at 2 kHz. The orientation of the TM and the location of the manubrium are shown in the first plot.	108
Fig. 8.12. Perspective 3D plots of the instantaneous deformations of the entire TM surface at eight stimulus phases at 4.317 kHz. The orientation of the TM and the location of the manubrium are shown in the first plot.	109
Fig. 8.13. Perspective 3D plots of the instantaneous deformations of the entire TM surface at eight stimulus phases at 5 kHz. The orientation of the TM and the location of the manubrium are shown in the first plot.	110
Fig. 8.14. Perspective 3D plots of the instantaneous deformations of the entire TM surface at eight stimulus phases at 6.771 kHz. The orientation of the TM and the location of the manubrium are shown in the first plot.	111
Fig. 8.15. Perspective 3D plots of the instantaneous deformations of the entire TM surface at eight stimulus phases at 10 kHz. The orientation of the TM and the location of the manubrium are shown in the first plot.	112

List of Tables

Table 1.1. Contents of various mammalian TMs, (Chole and Kodama, 1989).	7
Table 5.1. Geometry, mechanical properties, and basic FEA parameters of an idea object.....	46
Table 5.2. RMS and STD of the difference between FEA solutions and predictions of different modes for an ideal object.	49
Table 5.3. Geometry, mechanical properties, and basic FEA parameters of a geometry similar to a human TM.....	50
Table 5.4. RMS and STD of the difference between FEA solutions and predictions in different modes	52
Table 5.5. FEA solution plot of mode 1 deformation in x axis with different thickness to radius ratio and the corresponding RMS of the difference between FEA solution and prediction.....	55
Table 5.6. FEA solution plot of mode 1 deformation in x axis with different thickness to radius ratio and the corresponding RMS of the difference between FEA solution and prediction.....	57
Table 6.1. The near-infrared tunable lasers used in LD system.....	61
Table 6.2. Wavelength with respect to voltage of Vortex series lasers.	62
Table 6.3. Results of the test with a stable configuration.	68
Table 6.4. The material property and surface property of relative components.	81
Table 6.5. Basic specifications of cameras that were considered.	83
Table 8.1. Synthetic wavelength according to the wavelength of Vortex 0055 and Vortex 0078.....	97
Table 8.2. Geometry and mechanical properties of the artificial object.	98

Nomenclature

AOM	acousto-optical modulator
APP	anamorphic prism pairs
A_S	area of the stapes footplate
A_{TM}	TM area
BS	beam splitter cube
C	camera
C	collimator
C	circular fibers
CP	computing platform
DOEHS	digital optoelectronic holographic system
DOF	degrees of freedom
D	cosinusoidal image
D_λ	dark intensity at wavelength λ
ESPI	electronic speckle pattern interferometry
F	force
FCA	fiber coupler assemblies
G	grating
h	thickness of the shell
I	incus
IS	illumination source
k	magnitude of the propagation vectors \mathbf{K}_1 and \mathbf{K}_2
\mathbf{K}	sensitivity vector
\mathbf{K}_1	illumination vector
\mathbf{K}_2	observation vector
\mathbf{L}	displacement vector
L	laser

L	lens
LD	laser delivery
LDD	laser diode driver
LDPE	low density polyethylene
LDV	laser Doppler vibrometer
LG	light guide
M	malleus
M	mirror
MEEI	Massachusetts Eye and Ear Infirmary
MLDHS	multi-wavelength lensless digital holography system
MOP	mechatronic otoscope positioned
n	fringe orders
\vec{n}	normal vector
N	sinusoidal image
NDF	neutral density filter
$\vec{n}_x, \vec{n}_y, \vec{n}_z$	decompositions of \vec{n} along x , y and z axes
O	object
O	observation point
OB	object beam
OH	optical head
OH	otoscope head
OPL	optical path length
OS	optical switch
P	parabolic fibers
P	polarizer
P	randomly selected point on the sample
PBS	polarizing beamsplitter cube

PM	polarization maintaining
PM	positioning mount
P_S	pressure in the inner ear
P_{TM}	sound pressure acting on the TM
PZT	piezoelectric transducers
R	radius of curvature
R_p, R_1, R_2, R_n	position vectors where $n = 1, 2, \mathbf{P}$
R_λ	reference intensity at wavelength λ
$\%R_\lambda$	percentage relative to the reflection from a standard reference substance
R(1)	radial fibers which attach straight into the annular ring
R(2)	few radial fibers which cross paths
RB	reference beam
RMS	root mean square
S	stapes
SFA	spatial filter assembly
SM	stage mount
SMR	sub-mucous fine radial fibers
SP	short process of the malleus
SPL	sound pressure levels
STD	standard deviation
S_λ	sample intensity at wavelength λ
T	transverse fibers
TiO ₂	Titanium dioxide
TIR	trigonum interradiale
TM	tympanic membrane
TS	translation stage
U	umbo

\vec{U}	resultant deformation
U_x, U_y, U_z	x -axis, y -axis, z -axis deformation
$\vec{U}_x, \vec{U}_y, \vec{U}_z$	decompositions of \vec{U} along x , y and z axes
U_x', U_y'	predicted deformation in x - and y - axes
ZnO	Zinc oxide
α, β, γ	angles between the direction of \vec{U} or \vec{n} and x , y , z axes
$\Delta\phi$	phase difference
Λ	synthetic wavelength
λ	wavelength
$\lambda/2$	half-wave plate
$\lambda/4$	quarter wave plate
Ω	fringe-locus function

Objective

The objective of this Thesis was to develop a multi-wavelength lensless digital holography system (MLDHS) to measure acoustically induced 3D nanometer-scale deformations and millimeter-scale shape measurements of tympanic membranes (TMs) by a single optical setup with the capabilities of real-time, non-contact, full-field of view measurement. This Thesis will demonstrate the effectiveness of MLDHS, validate 3D deformations theory, describe the design and prototyping of MLDHS, and present representative measurements on a chinchilla TM *in vitro*.

1 Introduction

1.1 Anatomy of the ear

Anatomically, the mammalian ear can be divided into three functional parts as shown in Fig. 1.1: the outer (external) ear, the middle ear and the inner ear. The external ear which consists of auricle or pinna (the visible part of the ear) and the external auditory canal collects sound waves and transmits them to the middle ear (Hulli, 2008).

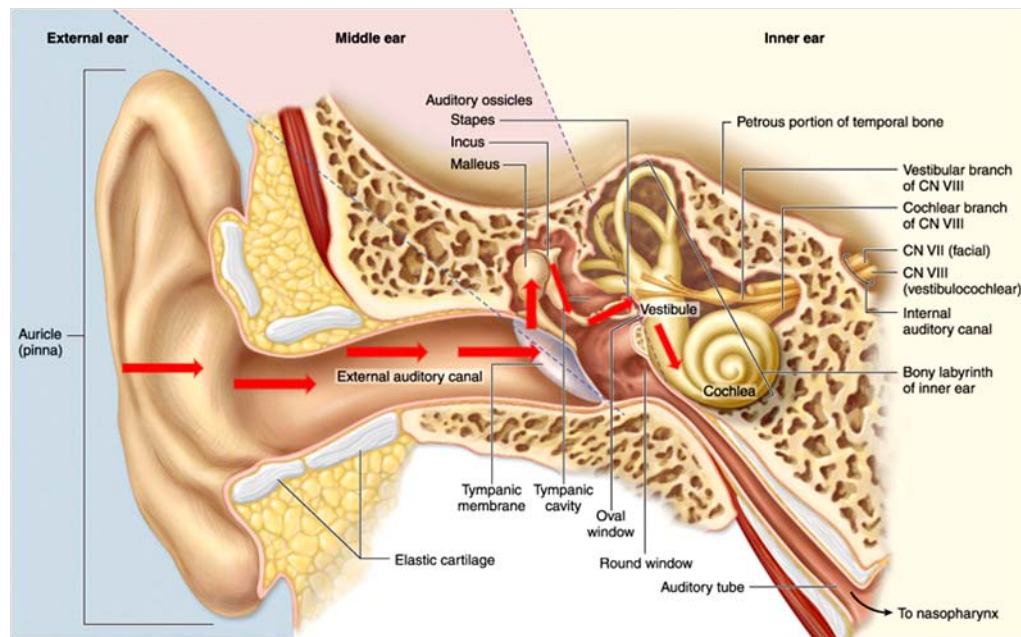


Fig. 1.1. Anatomy of the human ear: the cross section of human ear showing divisions of the outer, middle, and inner ears (Wikipedia, 2008).

1.1.1 Function of the tympanic membrane

To understand the function and importance of the tympanic membrane (TM), one must have a general knowledge of how a vibration in the air becomes a sound heard in the human brain. A sound wave travels into the ear via the auditory canal. It then contacts directly the TM. It is here that the sound energy is transferred from a gas (air) medium to a solid (the TM). This can be related to the opposite of how a loudspeaker functions (Schubert, 1980). The vibrating air causes the TM to vibrate in simple or complex patterns. Attached to the membrane is a bone, the malleus, which moves as the membrane vibrates. Next, the energy passes through two additional bones, the incus and then the stapes, see Fig. 1.2. The energy moves from the footplate (end) of the stapes to the inner ear, now traveling through a fluid. The energy is channeled through the cochlea, the auditory sensory organ within the inner ear. The sound energy stimulates hair cells, which produce synaptic activity that evokes action potentials that travel down the cochlea nerve to the brain (Schubert, 1980).

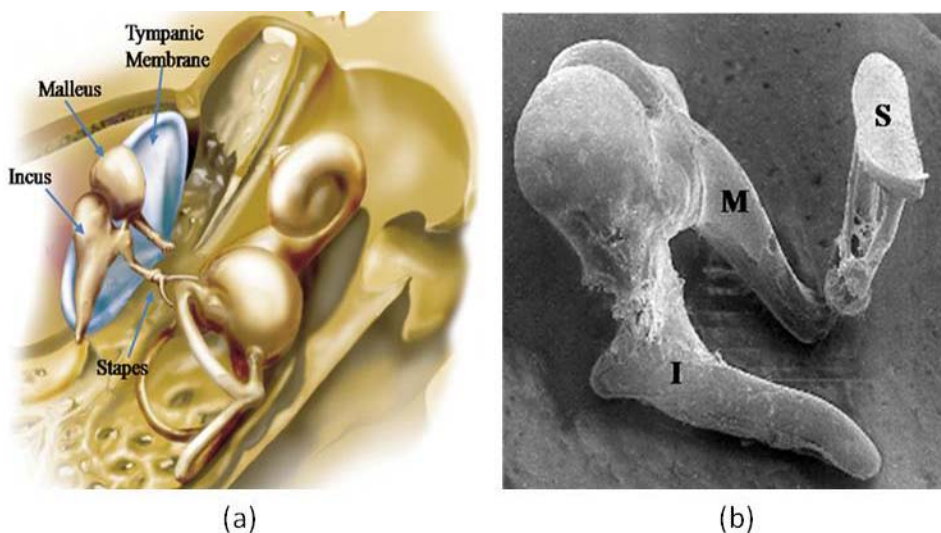


Fig. 1.2. Middle ear ossicles: (a) chain of ossicles and their ligaments, (b) the three bones: malleus (M) incus (I) and stapes (S) (Csillag, 2005).

Hearing requires the transfer of sound from a gaseous medium, to a solid, and finally the fluid, where it is translated into an electric potential (Katz, 2002). If one can imagine listening to someone speak in air while submerged underwater, one can appreciate the brilliance of how the ear functions. The primary purpose of the TM is to receive the sound energy from air, and then amplify it through solid tissue and bones. This amplification is possible due to what Katz calls the Areal relationship (Katz, 2002). For the sake of explanation, ignore the malleus and incus bones, as they do little to affect the sound energy and only link the TM to the stapes. The TM has a much greater area (15 to 20 times) than the footplate of the stapes, the bone responsible for transmitting the sound energy into a fluid (Standring and Gray, 2008). The sound pressure (P_{TM}) acting on the TM produces a force (F) equal to the product of the pressure and the TM area (A_{TM}). This force is conducted to the stapes footplate, which produces a pressure in the inner ear (P_S) equal to the ratio of the force and the area of the stapes footplate (A_S) as described by the relationship $P_S/P_{TM} = A_{TM}/A_S$. This transformer process helps overcome the difference in impedance between air and cochlear fluid (Karasic et al., 2009), see Fig. 1.3.

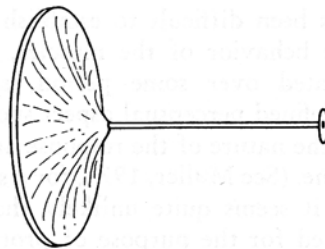


Fig. 1.3. TM to stapes area ratio (Schubert, 1980).

1.1.2 Physical Characteristics of the Tympanic Membrane

The human TM is elliptical in shape. TMs of all mammalian species consist of two parts: the Pars Flaccida and the Pars tensa, see Fig. 1.4. Although there is variation in shape and size among humans, it is generally accepted that the horizontal axis is 9 to 10 mm long and the vertical axis is 8 to 9 mm long (Wajnberg, 1987). The approximate density of the TM is 1200 kg/m^3 (Koike et al., 2002). The pars tensa portion of the TM has an approximate thickness of $34 \text{ }\mu\text{m}$ and the pars flaccida portion measures approximately $110 \text{ }\mu\text{m}$ (Chole and Kodama, 1989). Very loud sounds produce a displacement of the TM up to $1 \text{ }\mu\text{m}$ (Katz, 2002). Changes in pressure due to swallowing can produce displacements of up to 0.5 mm .

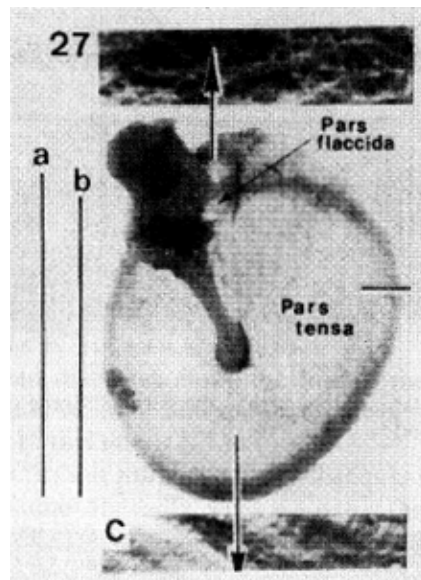


Fig. 1.4. Human TM showing two parts (Wajnberg, 1987).

The size and shape of the TM varies greatly in other mammalian species, see Fig. 1.5. In all species, the pars flaccida is thicker than the pars tensa. There are, however, large differences between species in regards to size and shape of the pars flaccid relative to the pars tensa (Chole and Kodama, 1989; Karasic and Largesse, 2009).

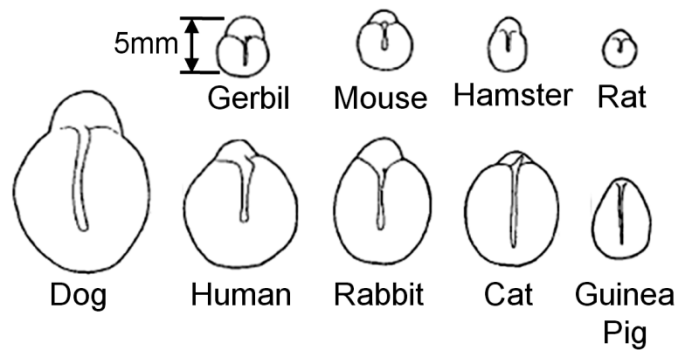


Fig. 1.5. Relative sizes of mammalian TMs (Chole and Kodama, 1989).

1.1.3 Histology of the Tympanic Membrane

The ultra-structure of the TM is made up of four primary components: collagen, keratin, elastin, and mast cells. The pars flaccida and pars tensa of the human TM are easily distinguishable from one another: the pars tensa contains tightly packed, highly ordered collagen bundles and the pars flaccida contains loose and inhomogeneous bundles. Collagen is a protein and is generally found in connective tissue in mammals. It exists as long fibers held together, forming a larger structure. Keratin, another fibrous protein, is found on the surface of both the pars tensa and pars flaccida. Elastin, a fibrous protein much like collagen, is found throughout the TM in lesser amounts than collagen. Finally, mast cells are found in the pars flaccida and not the

pars tensa (Lim, 1995). Mast cells are responsible for combating pathogens. A cross section of the human TM is shown in Fig. 1.6.

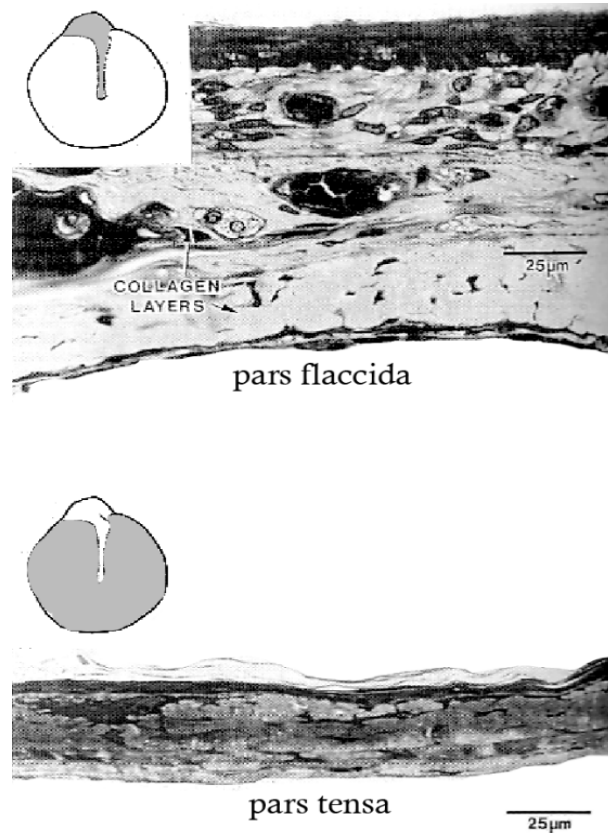


Fig. 1.6. Two sections of human TM: Upper - Pars Flaccida, and Lower - Pars Tensa (Lim, 1995).

In other mammalian species, amounts and locations of these substances varied greatly. Mast cells were found in all TMs, suggesting their importance to the healthy maintenance of the TM. A chart comparing the relative proportions of collagen, mast cells, keratin, and elastin species-to-species if found in Table 1. By further investigating the individual properties of these four

materials, and also quantifying their amounts in the TM, one could gain insight into mechanical and optical properties of the TM in a number of species (Chole and Kodama, 1989).

Table 1.1. Contents of various mammalian TMs, (Chole and Kodama, 1989).

PRESENCE OF VARIOUS SUBSTANCES IN TYMPANIC MEMBRANES						
	<i>Collagen</i>	<i>Elastin</i>	<i>Mast Cells</i>	<i>Macrophages</i>	<i>Keratin</i>	
Human						
Pars flaccida	++++	++	+	0	++	
Pars tensa	++++	++	+	0	++	
Dog						
Pars flaccida	+++	+	+	+	+++	
Pars tensa	++++	+	0	0	++	
Cat						
Pars flaccida	++	0	+	0	+++	
Pars tensa	++++	0	+	+	++	
Rabbit						
Pars flaccida	++	+	+	++	+	
Pars tensa	++++	+	+	+	+	
Guinea pig						
Pars flaccida	+	0	++	0	+	
Pars tensa	++++	0	0	0	+	
Rat						
Pars flaccida	+	0	+	+	++	
Pars tensa	++++	0	0	0	+	
Hamster						
Pars flaccida	+++	++	+	+	++	
Pars tensa	++++	+	0	0	++	
Gerbil						
Pars flaccida	+	+	++	+	++	
Pars tensa	+++	++	0	0	+	
Mouse						
Pars flaccida	+	0	+	0	++	
Pars tensa	+++	+	0	0	+	

Arbitrary scale indicates relative amounts.

The TM is composed of three distinct layers: the epidermis, mucosal epithelium, and lamina propria. The epidermis is a common keratinizing epithelium containing no hair follicles, glands, or other skin appendages. In humans, the epidermis slowly migrates away from the umbo towards the edges of the TM. It is believed that this behavior is a method of self cleaning, see

Fig. 1.7. This is not necessarily the case for other mammalian species, as a different behavior has been observed in guinea pig TM (Lim, 1995).

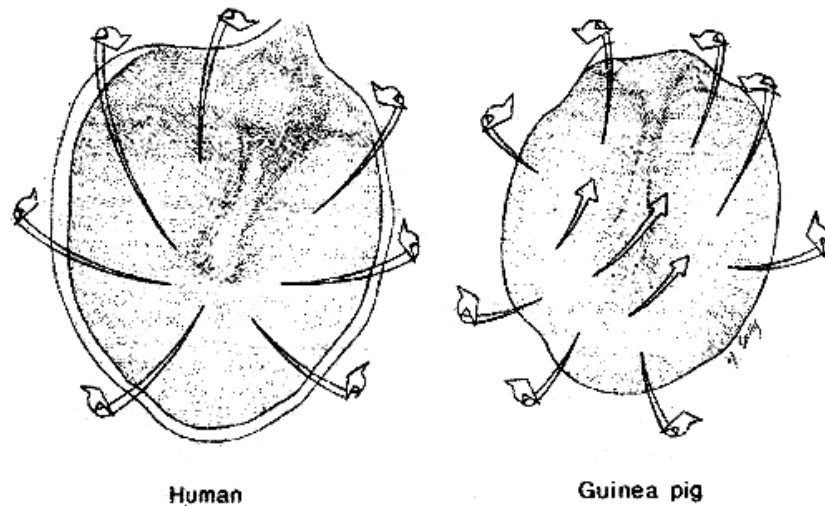


Fig. 1.7. Artist's conception of the migrating pattern of the epidermis in the TM of humans and guinea pigs (Lim 1995).

The lamina propria is the largest layer of the TM. It is largely consisting of loose connective tissue, collagen and elastic fibers. This layer is where mast cells are located, and it is responsible for the vascular and nerve supply to the TM. Most importantly, the fibers in the lamina propria are arranged in a very particular way that determines the precise patterns the TM creates when contacted by a sound. These fibers have been studied in a number of different methods including electron microscope and moiré shift interferometry (Lim, 1995). The majority of fibers are categorized as either radial or circular, all centered around the umbo. A smaller number of transverse and parabolic fibers also are present, see Fig. 1.8 and Fig. 1.9. It has also been

observed that spontaneously healed TMs are unable to re-create these complex fiber layers accurately (Lim, 1995; Karasic and Largesse, 2009).

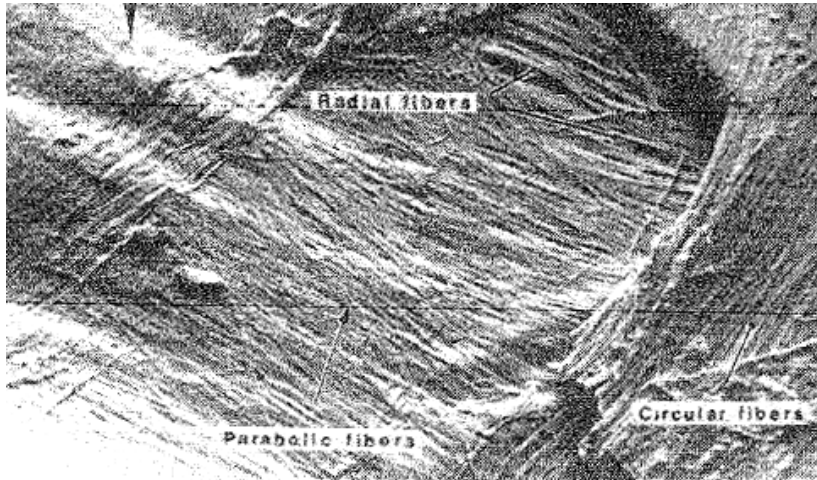


Fig. 1.8. A SEM photomicrograph of the outer radial and inner circular fibers and the parabolic fibers in the fibrous layer of the pars tensa (Lim, 1995).

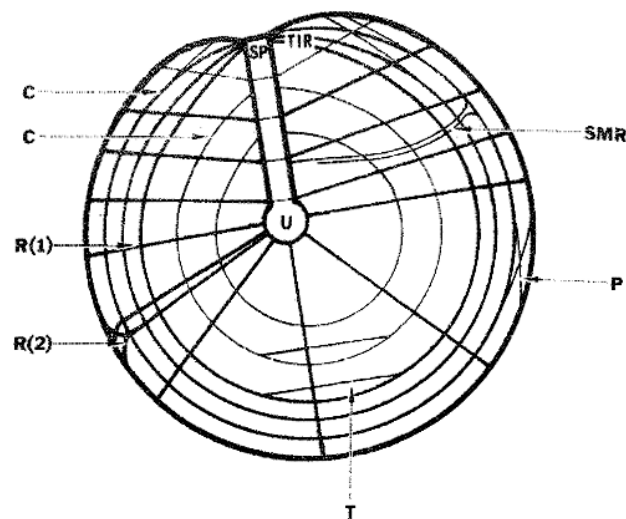


Fig. 1.9. Artist's conception of the fiber arrangement of the human TM. SP: short process of the malleus; U: umbo; TIR: trigonum interradiale; C: circular fibers; R(1): radial fibers which attach straight into the annular ring; R(2): a few radial fibers which cross paths; T: transverse fibers; P: parabolic fibers; SMR: sub-mucous fine radial fibers (Lim, 1995).

2 Significance of 3D deformations and shape measurements on human tympanic membranes

Since the most recent survey in 2005, the number of hearing impaired people in the US increased from 31.5 million to 35 million, a 9 percent increase in a period of time with just 4.5 percent population growth (Hear-it, 2011). The 2005 MarkeTrak VII report projected that the numbers of Americans with hearing loss will increase to 40 million by 2025 and 53 million by 2050 (Hear-it, 2011).

The TM is the most peripheral structure in the middle ear and is the first ear structure set in motion by airborne sound. It helps transmit sound energy into the inner ear to initiate the neurologic events associated with hearing. Current methodologies for characterization of the TM have some limitations, they are: qualitative rather than quantitative, usually consist of single point mobility measurements, or only include one-dimensional deformation measurements. Furthermore, none of the current clinical tools for diagnosis of hearing losses can measure the shape of the TM, which is very useful for anatomy and pathology. Therefore, medical researchers and doctors desire a tool that can measure both shape and deformations.

3 Optical techniques of deformation and shape measurements of tympanic membranes

3.1 Moiré topography

Moiré topography is a non-contact technique that measures shape, displacement, strain and more. It is based on overlapping images of two gratings that generates moiré fringes: the object grating and the reference grating. Moiré topography mainly consists of two techniques: shadow moiré and projection moiré. An advantage is that it is not necessary to use coherent light in moiré technique. However, a stringent requirement for moiré topography is that the surface must reflect light diffusely. To address this issue, a popular method is to apply a thin, diffusely reflective coating onto the surface of the object. Dirckx's group made many measurements of the shape and static displacement of the TM by moiré topography. In his early work, they worked mainly on shadow moiré; in recent years they worked more on projection moiré.

In classic shadow moiré (Fig. 3.1), a grating with parallel lines is cast onto an object. The shadow of the grating is a set of deformed lines and is modulated by the object's shape. Interference happens between the reference grating by means of un-deformed grating and deformed grating casted on the object when viewing through the original grating.

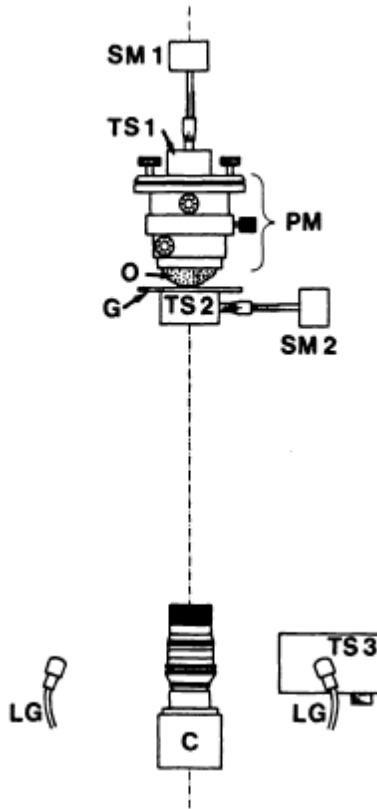


Fig. 3.1. Schematic representation of classic shadow moiré apparatus: SM is the stage mount, TS is the translation stage, PM is the positioning mount, O is the object, G is the grating, LG is the light guide and C is the camera, (Dirckx and Decraemer 1991).

A phase-shift moiré interferometer based on an automatic computer to measure the shape of human and cat TMs was built (Decraemer and Dirckx, 1991). This setup recorded four-step phase shifted moiré interferograms that were generated by small changes in the object-to-grating distance. The calculation of object height required at least three phase shifted interferograms to solve the problem automatically on every object point and it can be simplified by using four moiré interferograms. The resolution in object-to-grating direction was 20 μm . More details of the setup were described in other papers (Dirckx and Decraemer 1989). Using the same setup, they pursued further research and focused on very precise measurements of human TM structure,

including shape and curvature of the TM, shape and curvature of the manubrium, and other shape related measurements in the peripheral area (Decraemer et al., 1991). In displacement measurements of human TMs, they used a similar setup to obtain only three-step phase shifted interferograms (Dirckx and Decraemer, 1991). The final resolution depended on the accuracy of the object translation system and intensity level measurements. In this work, the resolution in object-to-grating direction was also 20 μm . The phase-shift shadow moiré interferometer was used to measure the shape of the cat TM with a normal mobil malleus and with an immobile malleus as it was cyclically loaded with static middle-ear pressures up to ± 2.2 kPa, and measurements were presented in the form of gray-level full-field shape and displacement images, of displacement profiles, and of pressure-displacement curves for selected points (Ladak et al., 2004).

A major weakness of shadow moiré is that the grating needs to be positioned as close as possible to the object due to the limitation of the depth of field of the shadow. Because of this weakness shadow moiré can not be utilized in the research on middle ear because it is difficult to place the grating close enough unless enough bone is removed. In contrast, projection moiré has the advantage that the object can be positioned freely.

For classic projection moiré (Fig. 3.2), the basic idea is to project straight equidistant lines through one grating onto the object. When viewing the bent projected lines on the object at an angle with respect to the projection direction through a second identical grating, interference appears between the deformed and un-deformed grating lines, producing moiré fringes which can be interpreted as contours of equal object height. In shadow moiré, only one grating is used, while in projection moiré, two separate gratings are used. Besides the moiré fringes, grid lines are also

seen in the interferograms. This effect is called grid noise. In order to eliminate this effect in the final interferograms, translation of the grating in its own plane when recording images is needed.

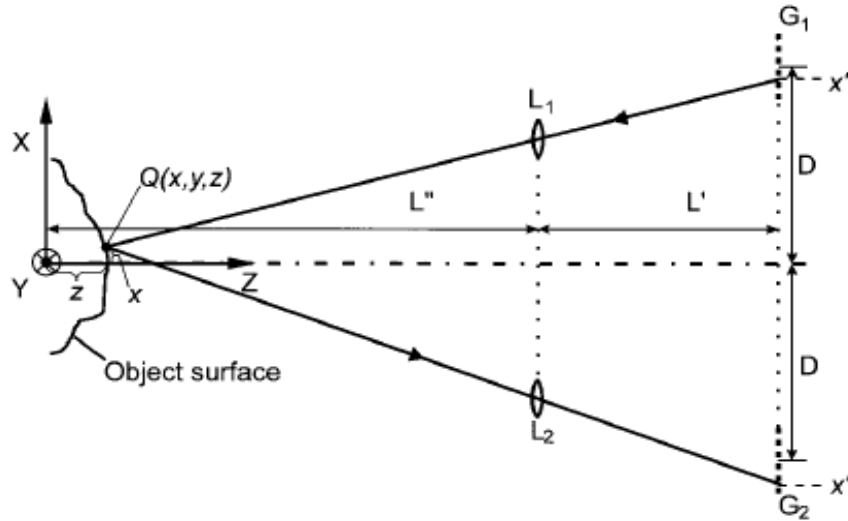


Fig. 3.2. Schematic representation of classic projection moiré apparatus: G is the grating and L is the lens, (Dirckx and Decraemer 2000).

Moiré contour-difference technique was used to obtain the displacement of the surface of the gerbil TM under different static pressure (von Unge et al., 1993). The moiré interference for displacement measurement generated two different sets of images of the object: one was recorded when the object was un-deformed, the other one was recorded when the object was in a deformed state that introduced a change of the fringe patterns. Different from a classic projection moiré, this setup contained no second grating, which meant the projected grid lines were not optically demodulated, but were recorded by the CCD camera. In 1995, the authors used the same setup to measure the shape and displacement of gerbil TM in experimental otitis media with effusion (von Unge et al., 1995). For shape measurement, interference appeared between the grid image on a

flat plate and the grid line image on the object. The same authors also brought projection moiré technique to the shape and displacement studies of the TM (Dirckx and Decraemer, 1997). At the same year, they measured and modeled the boundary shape and displacement of Mongolian gerbil pars flaccid (Dirckx and Decraemer, 1997); the methods are described in previous papers (Dirckx and Decraemer, 1997). In 1999, measurement at gerbil TM displacement patterns in experimental cholesteatoma was performed (von Unge et al., 1999) and used the same methods as in their earlier otitis media studies (Dirckx and Decraemer, 1997).

In 2000, Dirckx and Decraemer developed a slightly different configuration of the projection moiré setup by adding a second grating in front of the CCD (Dirckx and Decraemer, 2000). An endoscopic moiré interferometry overcoming the issue of difficult access ability was developed (Martínez-Celorio et al., 2004). A method using two liquid crystal light modulators to perform high-resolution phase-shifting moiré topography without any mechanically moving parts was implemented (Dirckx et al., 2010).

3.2 Laser Doppler vibrometer

Laser Doppler vibrometer (LDV) is a very sensitive, noncontact optical tool that measures velocities of vibrating objects with nanometer-scale resolutions (Fig. 3.3). It has been used in clinical research for examining middle-ear function under sound simulation by measuring velocity of the TM, especially the umbo in the center of the TM. Generally, the setup is that an ear speculum attached to a glass-backed coupler with a sound source and a probe microphone is placed in the external ear. Under microscopic observation, a helium-neon laser beam controlled by a prism is aimed through the ear canal at any point of interest. The reflected beam is analyzed

by the Doppler shift principle, which compares the frequency of emitted light with the frequency of reflected light on a moving object, and the output signal of LDV is voltage proportional to the object velocity. In most cases, velocity is used to compute displacements.

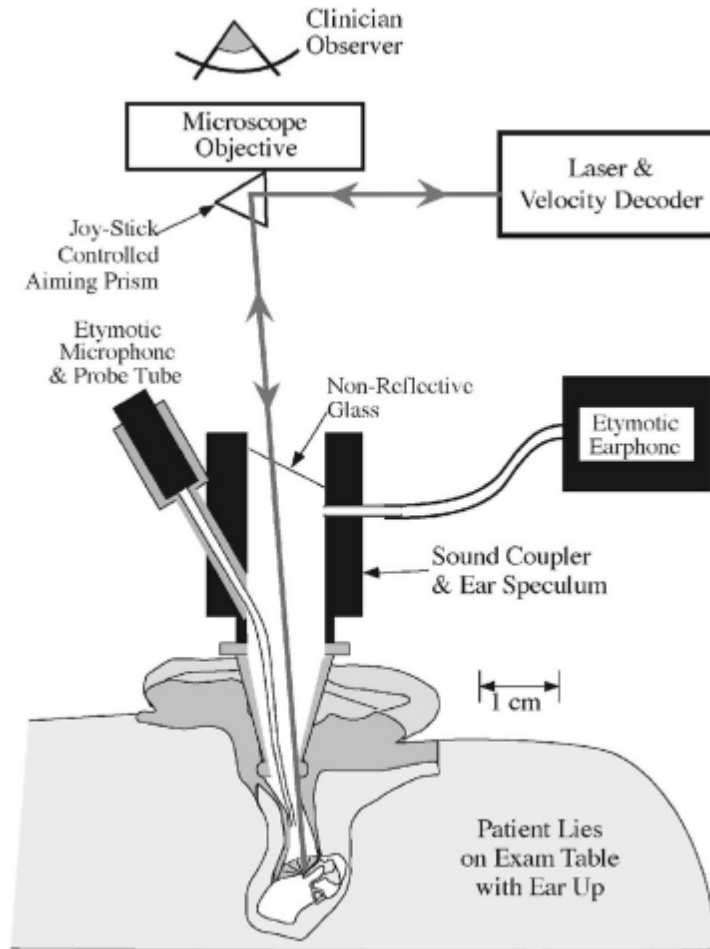


Fig. 3.3. Single-point LDV measurements of the TM, (Rosowski et al., 2008).

LDV has been applied to the investigations of sound-induced middle-ear deformations in animals, human temporal bones, and live human subjects. Some studies have investigated the motion of different targets, such as umbo, malleus, incus and stapes, and some studies have

focused on the diagnosis of different hearing diseases, such as sensorineural hearing loss, and conductive hearing loss, etc.

Umbo displacement of six live human subjects by LDV and measurements on fifteen fresh human temporal bones for comparison were performed (Goode et al., 1993). Sound pressure levels (SPL) were 60, 70, 80 dB and frequency range was from 140-19433 Hz. Both cases showed similar results. Three years later, the same research group reported umbo displacement in an additional 89 live human ears (Goode et al., 1996). In addition, they investigated measurements on TM, malleus and prosthesis head displacements at 80-100 dB SPL with 200-15000 Hz-frequency range. Results provided information about diagnosis and selection of the best reconstruction. In another study, 129 eardrums of 79 human subjects were divided into three groups: normal subjects, subjects with sensorineural hearing loss and subjects with conductive hearing loss (Huber et al., 2001). A total SPL was 94 dB with 500-8000 Hz-frequency range. Results showed that it was impossible to separate normal subjects and subjects with sensorineural hearing loss, but possible to differentiate between normal subjects and subjects with conductive hearing loss. Also it proved that LDV had the ability to differentiate normal middle ears, stapes fixation, malleus fixation, and incus luxation before surgery. And it came to the conclusion that LDV is a useful additional tool for routine audiological investigations for preoperative evaluation of the mobility and integrity of the ossicular chain. Separation of otosclerotic ears from normal ears with a sensitivity of 82% and specificity of 92% was achieved by evaluating 49 ears with conductive hearing loss and 150 normal ears (Jakob et al., 2009). SPL was from 80-90dB and frequency range was from 250-4000Hz. The authors also figured out the age variation did affect the umbo transfer function, and it was not sufficient for LDV to be a single diagnostic tool. However, another study found no effects of stimulus level, ear sidedness, gender, age or the

presence or absence of sensorineural hearing loss (Whittemore et al., 2004). These authors evaluated 56 normal hearing patients and 47 subjects with sensorineural hearing loss, and the repeatability was within 20% of magnitude and 30° of angle. The maximum sound level within the coupler was about 90dB SPL and frequency range was 250-6000 Hz. No functional difference was observed between velocity measurements in the normal hearing and sensorineural hearing loss groups, and umbo velocities were unrelated to auditory threshold in normal hearing groups. LDV was used to evaluate alterations of umbo velocity caused by different ossicular pathologic changes (Rosowski et al., 2003). Results showed that it was easy to distinguish normal ears and ears with ossicular interruption or malleus fixation, but it was not easy to differentiate normal ears and ears with stapes fixation. However, there were clear differences between measurements in ossicular interruption, malleus fixation and stapes fixation. Further studies of the same group showed that combination of LDV and air-bone gap can help distinguish normal ears and ears with stapes fixation (Rosowski et al., 2008). LDV can also help differentiate air-bone gap produced by ossicular fixations from air-bone gaps associated with inner-ear malformations.

3.3 Holographic interferometry

Holographic interferometry is widely used to study the displacement, stress and strain of components. There are main two types of holography interferometry: (1) classic holography that was developed at the initial stage of this technique and (2) digital holography that was developed in the late 1990's.

A typical classic holography setup is shown in Fig. 3.4. A highly coherent laser light is divided into two beams by means of a beam splitter. One of the beams that goes straight through the beam splitter, is directed to illuminate an object to be recorded. This beam is known as the object beam. The other beam that is reflected from the beam splitter is directed to the recording medium, a holographic plate, without any interference with the object. This beam is known as the reference beam. The interference pattern appears when the object beam superposes with the reference beam. In order to reconstruct this hologram, the holographic plate is illuminated by the original reference beam.

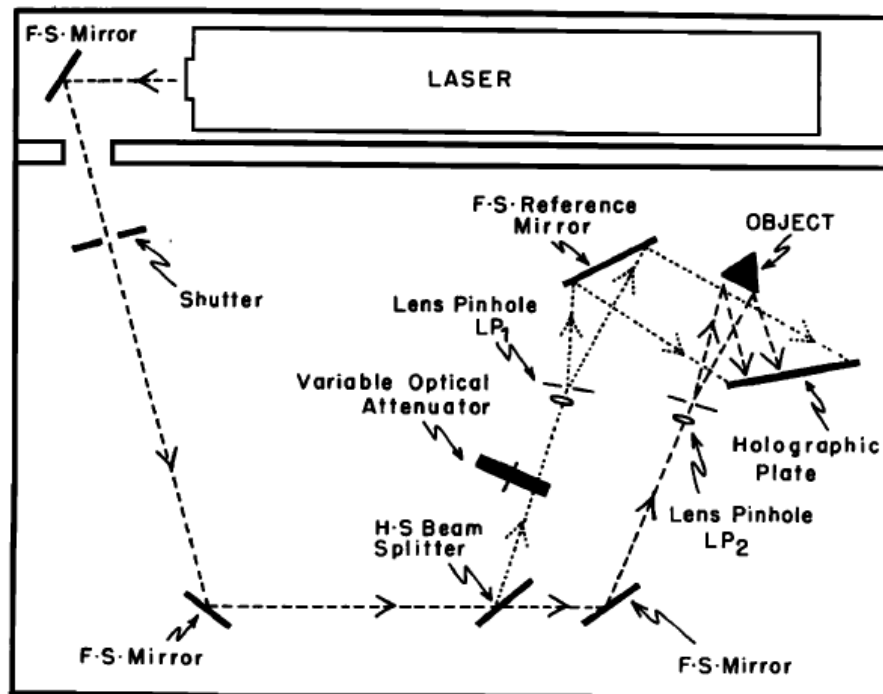


Fig. 3.4. Classic holography setup, (Khanna and Tonndorf, 1972).

In 1971, time-averaged holography was used to measure the TM vibrations in fresh cadavers of cats and living cats (Khanna and Tonndorf, 1972). The optical setup is shown in Fig. 3.4. In

this work, they investigated the effect of coatings applied to the TM with different thicknesses. Such coatings were necessary to image the nearly transparent TM. Then they compared the vibrations in fresh cadavers and in living animals, which indicated that there was no difference between these two kinds of samples. They also compared the anterior, posterior and malar amplitudes and results showed that at all frequencies, the TM vibrated maximally in the posterior-superior quadrant and less in the anterior and inferior ones. The TM displacements in guinea pig ears subjected to acoustic impulses were investigated (Dancer et al., 1975). They pointed out the motion of the umbilicus was approximately 7.5 times smaller than that of the maximum elongation point of the TM located between the umbilicus and the annulus fibrocartilagineus in the prolongation of the manubrium mallei. Holography was utilized to evaluate the influence of the indwelling tube on vibration of the TM (Maeta et al., 1991). Results showed that after insertion of a ventilation tube, the vibration pattern of the TM was not obviously changed, but the vibration amplitude of the TM was decreased.

In digital holography, CCD sensors are used instead of holographic plates and the reconstruction of the digitized holograms is performed numerically (Wagner et al., 2000). The vibration measurement on the human eardrum in vivo was investigated by electronic speckle pattern interferometry (ESPI) which is a digital holographic method (O. J. Løkberg et al., 1979; 1980). Preliminary experiments demonstrated that ESPI with a continuous laser could be used to measure TM vibration on living objects. Recently a group at WPI and the Massachusetts Eye and Ear Infirmary (MEEI) began using digital holography to investigate the TM motions. Test samples included cadaveric chinchillas, cats, humans, humans after cartilage tympanoplasty and the ear of a live anesthetized chinchilla (Aarnisalo et al., 2009; Furlong et al., 2009; Hernandez-Montes et al., 2009; Aarnisalo et al., 2010; Cheng et al., 2010).

4 Digital optoelectronic holography system developed by WPI-MEEI

An advanced computer-controlled digital optoelectronic holographic system (DOEHS) has been currently under development by WPI-MEEI with the capabilities for real-time, non-contact, full-field-of-view, and both qualitative and quantitative measurements (Hulli, 2008; Furlong et al., 2009; Hernandez-Montes et al., 2009; Karasic and Largesse, 2009; Dobrev et al., 2010; Goldish and Kunyz, 2010; Harrington et al., 2010; Bapat, 2011; Harrington et al., 2011; Dobrev et al., 2011; Flores-Moreno et al., 2011; Lu et al., 2011). The latest prototype was delivered to MEEI for the investigation and diagnosis of middle-ear conductive hearing loss and to study the cause of failed middle-ear surgical procedures.

In the following sub-sections, an overview of the modes of operation as well as description of the hardware and software of the DOEHS are presented.

4.1 Fringe-locus function

As an object deforms or is displaced during the recording of a hologram, the optical path length of the light reflected off the object changes. The path length changes in phase differences, which are recorded in the form of fringes. These fringes are described by a fringe-locus function (Ω) with constant values that define fringe loci on the object's surface (Pryputniewicz, 1996). The fringe-locus function relates directly to the fringe order (n)

$$\Omega = 2\pi n. \tag{4.1}$$

Additionally, the fringe-locus function can be related to the scalar product of the sensitivity vector \mathbf{K} with the displacement vector \mathbf{L} as

$$\Omega = \mathbf{K} \cdot \mathbf{L}. \quad (4.2)$$

The nature of the sensitivity vectors can be described with the help of Fig. 4.1, which shows the illumination \mathbf{K}_1 and the observation \mathbf{K}_2 vectors of a random object under test.

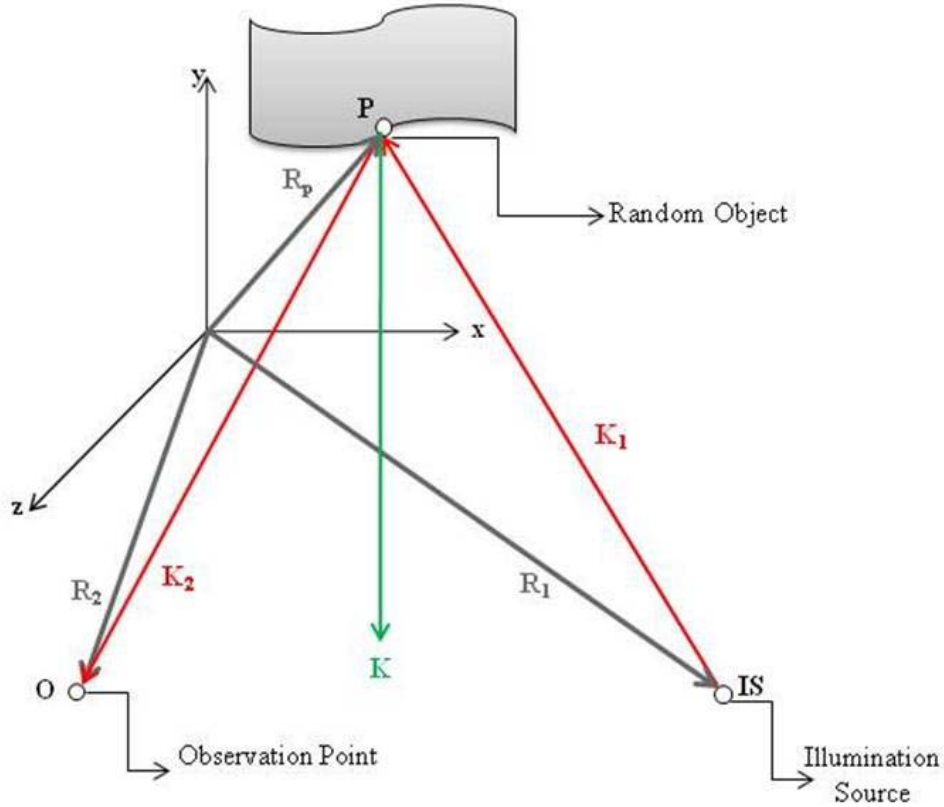


Fig. 4.1. Illumination and observation geometry for holographic interferometry: \mathbf{R}_p , \mathbf{R}_1 , and \mathbf{R}_2 are the position vectors whereas \mathbf{K}_1 and \mathbf{K}_2 are the illumination and the observation vectors, respectively. \mathbf{K} is the sensitivity vector, (Hulli, 2008).

In Fig. 4.1, \mathbf{IS} is the illumination source, e.g., a laser, \mathbf{O} is the observation point, e.g., a camera, detector, or simply an eye, and \mathbf{P} is randomly selected point on the sample, where \mathbf{R}_1 , \mathbf{R}_2 and \mathbf{R}_p are the position vectors which describe the spatial coordinates of these points.

These position vectors are described as

$$\mathbf{R}_n = R_n \hat{x} + R_n \hat{y} + R_n \hat{z} \quad n = 1, 2, \mathbf{P}. \quad (4.3)$$

The illumination and observation vectors \mathbf{K}_1 and \mathbf{K}_2 can be written, respectively, in Cartesian components as,

$$\mathbf{K}_1 = K_1 \hat{x} + K_1 \hat{y} + K_1 \hat{z}, \quad (4.4)$$

and

$$\mathbf{K}_2 = K_2 \hat{x} + K_2 \hat{y} + K_2 \hat{z}. \quad (4.5)$$

Correspondingly they can be expressed in terms of the position vectors depicted in Eq. 4.3 as

$$\mathbf{K}_1 = k \frac{R_p - R_1}{|R_p - R_1|}, \quad (4.6)$$

and

$$\mathbf{K}_2 = k \frac{R_2 - R_p}{|R_2 - R_p|}. \quad (4.7)$$

In Eq. 4.6 and Eq. 4.7, k , the wave number, is the magnitude of the propagation vectors \mathbf{K}_1 and \mathbf{K}_2 , and it is related to the wavelength (λ) of the laser light

$$|\mathbf{K}_1| = |\mathbf{K}_2| = k = \frac{2\pi}{\lambda}. \quad (4.8)$$

Based on the results of Eq. 4.6 and Eq. 4.7, the sensitivity vector \mathbf{K} , which specifies the direction of deformation to which a holographic setup will be most sensitive, can be calculated as the difference between the observation vector \mathbf{K}_1 , and the illumination vector \mathbf{K}_2 ,

$$\mathbf{K} = \mathbf{K}_2 - \mathbf{K}_1. \quad (4.9)$$

In DOEHS, the illumination point and the observation point is the same, and the out-of-plane deformation is along the light propagation axis defined as z-axis. Therefore, Eq. 4.9 can be simplified to

$$\mathbf{K} = K_2\hat{z} - K_1\hat{z} = 2K_2\hat{z}, \quad (4.10)$$

and taking into account the displacement vector \mathbf{L} redefined as

$$\mathbf{L} = L_x\hat{x} + L_y\hat{y} + L_z\hat{z} = L_z\hat{z}, \quad (4.11)$$

leads to the definition of the fringe-locus function for parallel illumination-observation conditions

$$\Omega = (2K_2\hat{z})(L_z\hat{z}). \quad (4.12)$$

4.2 Holographic interferometry modes of operation

The DOEHS can perform both static and dynamic measurements by time-averaged mode and double-exposure mode. More specifically, vibration measurements of the TM can be operated in time-averaged mode for qualitative view and double-exposure mode for quantitative data acquisition. In double-exposure mode, a stroboscopic technique is utilized for vibration measurements at a precise segment of the stimulus, which synchronized an acousto-optic modulator (AOM) to a stimulus. In addition, double-exposure mode embedded in multi-wavelength lensless digital holography system can perform shape measurements, which will be discussed in the next chapters.

4.2.1 Time-averaged mode

Time-average mode, which is for viewing the modes of motion of the object, utilizes phase stepping on one of the laser beams and produces fringes showing the shape of vibrations of the object of interest due to a stimulus (Harrington et al., 2010).

In time-averaged mode, measurements are obtained by continuous image acquisition and exposure of the camera to display intensity distributions of the form

$$I(x, y) = \frac{1}{\Delta t} \int_t^{t+\Delta t} I_t(x, y, t) dt. \quad (4.13)$$

Time-averaged mode allows for the viewing of the near-instantaneous movement of an object. This is accomplished by using a time varying fringe-locus function, $\Omega(x, y)$ related to the vibrating object (Pryputniewicz, 1985; 1987; 1989).

Images recorded contain information about the amplitude of an object's vibration in the form of fringes. Each reconstructed image requires four holograms recorded using a phase stepping technique, where the path length of the reference beams is controlled by a stepping function synchronized with the acquisition rate of the camera. The fringes obtained are contours of equal vibration amplitudes of the spatial vibration modes corresponding to the zeros of the square of the zero-order Bessel function of the first kind. This technique is also known as the real time holography technique (Powell and Stetson, 1965; Kreis, 2005; Bapat, 2011).

4.2.2 Double-exposure mode

Double-exposure mode allows quantitative measurement of shape and deformation between two loading states, and requires a set of four phase-shifted reference images together with four images in the deformed state to generate a phase map of deformations of the object (Harrington et al., 2010).

The result gives a difference between the two states in the form of a wrapped phase map. To utilize double exposures to view the entire motion of the TM's vibration, laser light illuminates the object only during a specified small percentage of the period. This stroboscopic illumination freezes the object at a specific place in its motion. To calculate the change from the reference to deformed state, the intensity of the reference state is described by

$$I_n(x, y) = I_r + I_0 + 2\sqrt{I_n I_0} \cos(\Delta\phi + \Delta\theta_n), \quad (4.14)$$

and the intensity of the deformed state is described by

$$I'_n(x, y) = I_r + I_0 + 2\sqrt{I_n I_0} \cos(\Delta\phi + \Omega + \Delta\theta_n). \quad (4.15)$$

where Ω is the fringe-locus function described in Sec. 4.1, which is the change in phase due to the change in shape or deformation of the object. Solution for Ω leads to two equations: D , a cosinusoidal image, and N , a sinusoidal image, of the form,

$$D = 64I_0I_r \cos(\Omega), \quad (4.16)$$

$$N = 64I_0I_r \sin(\Omega), \quad (4.17)$$

which are combined to produce and display double-exposure wrapped optical phase

$$\Omega = \tan^{-1}\left(\frac{N}{D}\right). \quad (4.18)$$

To obtain the complete motion of the TM over an excitation wave, stroboscopic mode uses an AOM to transmit light from the laser only during a portion (usually 5% to 15% duty cycle) of the excitation signal, giving the appearance to the camera that the object is continuously in the state of interest, while an image is acquired. The phase of the strobe pulse wave is adjusted relative to the tonal excitation to view a different part of the excitation.

Stroboscopic operation is implemented in software through a set of controls that allow the operator to select the frequency, amplitude, phase, duty cycle, and other relevant parameters. When signaled to start, the computer sends a series of commands to the function generator, connected through the USB. This starts the excitation and control of the AOM. Either manually or automatically, the phase can be swept, showing the movement of the object at all points of the stimulus.

Results of this process may be saved to individual image files or a single video file automatically, and can later be processed and analyzed.

4.3 Hardware

The DOEHS consists of laser delivery system (LD), otoscope head (OH), mechatronic otoscope positioner (MOP), and the computing platform (CP), shown in Fig. 4.2 and Fig. 4.3.

The LD system presently at MEEI houses a 532 nm wavelength laser with 50 mW of power. The laser beam coming out from this laser passes through an acousto-optical modulator (AOM) first which is controlled in stroboscopic mode, and then is split by a 100 mm³ beam splitter cube (BS) so that 80% of the beam is transmitted as the object beam (OB) and 20% is reflected as the reference beam (RB). Both of the split beams are redirected by mirrors, which are controlled by piezoelectric transducers (PZT), and then coupled to optical fibers by fiber coupler assemblies

(FCA). Shutters in both reference and object paths are used for beam ratio measurement. All components of the LD system are packaged onto an 18"×12"×1/2" breadboard and covered by an acrylic box.

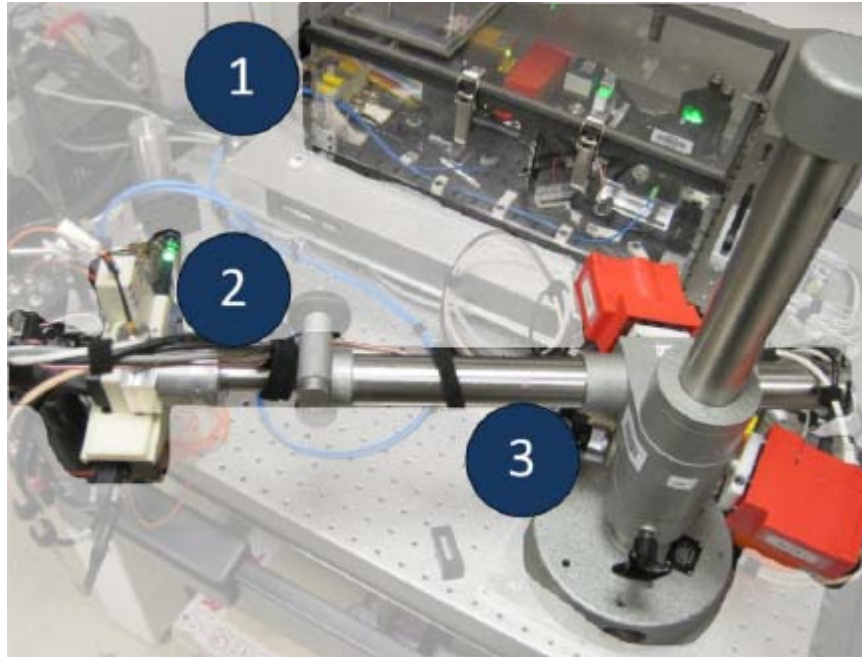


Fig. 4.2. Optoelectronic-mechanical components of DOEHS deployed at the Massachusetts Eye and Ear Infirmary (MEEI): (1) the laser delivery (LD) system, (2) otoscope head (OH) system, and (3) mechatronic otoscope positioner (MOP), (Dobrev et al., 2010; Harrington et al., 2010; Dobrev et al., 2011; Harrington et al., 2011).

The OH system is connected with LD system by single mode polarization maintaining (PM) fibers of 400-600 nm wavelength bands. Inside of the OH system, OB and RB are combined together by another 100 mm³ BS (80% for object beam and 20% for reference beam), and then the output beam is used to illuminate the object. The reflected beam from the object is observed by a high resolution CCD camera. The illumination beam and observation beams travel along the same direction.

The MOP is designed based on a commercially available microscope positioner whose mechanism is altered to fit the OH and it is also retrofitted with an adjustable braking system. The mechanical modifications are based on the required degrees of freedom (DOF) and workspace to position the otoscope in the patients' ear. The intuitive control system of the MOP allows it to be controlled by the examiner with a single button (Dobrev et al., 2011).

The computing platform (CP) consists of two physical parts: a driver and power unit, and PC that controls the whole system through the driver module (Dobrev et al., 2011; Harrington et al., 2011).

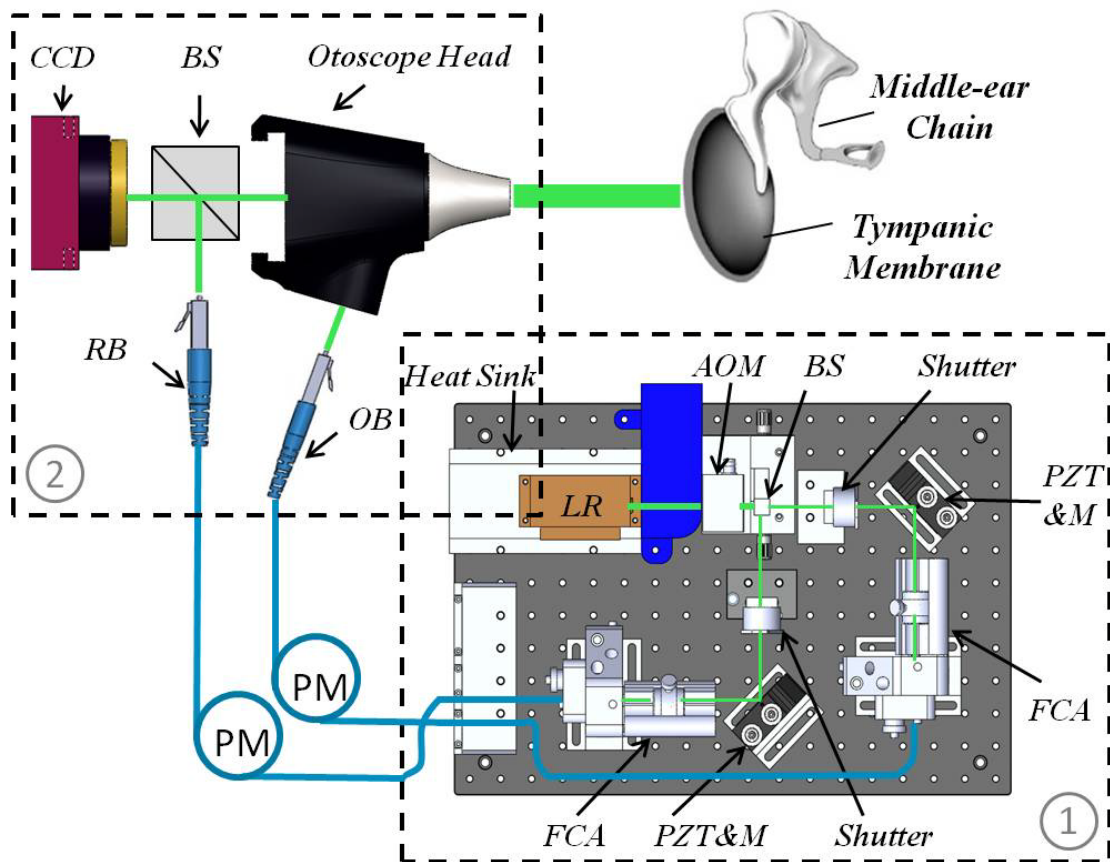


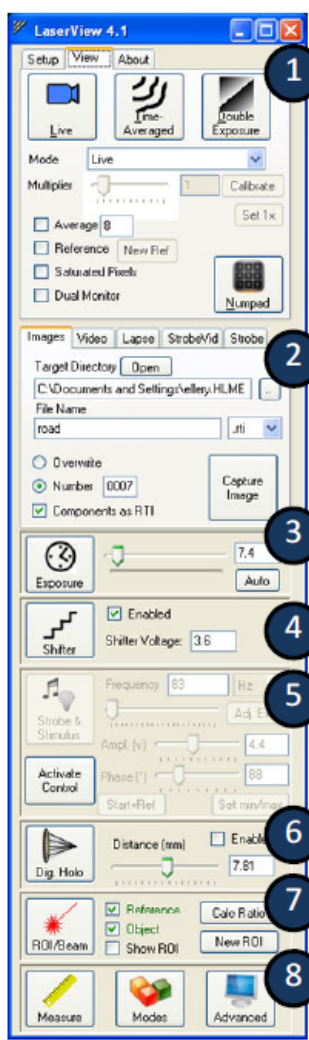
Fig. 4.3. Schematic of DOEHS: (1) LD system and (2) OH system.

4.4 Software

4.4.1 LaserView

LaserView, a control and acquisition software installed in the CP system and developed by our lab, is programmed in Visual C++ and has the ability to connect to one of five separate camera interfaces, a DAQ card, a function generator, laser controllers, and other hardware for other applications (Dobrev et al., 2011). LaserView can display live unprocessed images from the camera, and processed images in time-averaged mode, double-exposure mode and stroboscopic mode. With LaserView, the video from the camera is processed in real-time to show either the modulation level or the optical phase map of the object, based on four sequential phase-stepped images from the camera (Harrington et al., 2010).

LaserView can save a single set of these images, images at specific points of interest (e.g. points of the vibration in stroboscopic mode), or a continuous video stream, which can later be reconstructed and processed at any point in the video. Images and videos are saved in a proprietary formats (RTI for images and LVVID for videos) to allow for up to 16-bit grayscale camera raw images, as well as 32-bit floating point images for saving phase information in radians or actual units (Harrington et al., 2011). Every image, either individual or in a video file, contains application-specific metadata to save all relevant information about the camera's settings, reconstruction distance, active stimulus, and many other pieces of information (Harrington et al., 2011). Figure 4.4 shows a diagram of basics of LaserView's operation.



The screenshot shows the LaserView 4.1 software interface. It has a menu bar with 'Setup', 'View', and 'About'. Below the menu bar are three icons: 'Live', 'Time-Averaged', and 'Double Exposure'. The 'Live' icon is selected. Below these are 'Mode' (set to 'Live'), 'Multiplier' (set to 1), and 'Calibrate' buttons. There are checkboxes for 'Average 8', 'Reference', 'Saturated Pixels', and 'Dual Monitor'. A 'New File' button and a 'Numpad' icon are also present. The 'Images' section has tabs for 'Video', 'Lapse', 'StrobeVid', and 'Strobe'. It includes a 'Target Directory' (set to 'C:\Documents and Settings\valley.HLME'), a 'File Name' field (set to 'road'), a file type dropdown (set to '.rti'), and a 'Capture Image' button. There are radio buttons for 'Overwrite', 'Number' (set to '0007'), and a checked checkbox for 'Components as RTI'. The 'Exposure' section has a slider set to 7.4 and an 'Auto' button. The 'Shifter' section has a checked 'Enabled' checkbox and a 'Shifter Voltage' field set to 3.6. The 'Strobe & Stimulus' section has a 'Frequency' field set to 83 Hz, an 'Ampl. (v)' field set to 4.4, and a 'Phase (°)' field set to 88. There are 'Activate Control' and 'Start-Ref' buttons. The 'Dig Holo' section has a 'Distance (mm)' field set to 7.81 and an 'Enable' checkbox. The 'ROI/Beam' section has checked checkboxes for 'Reference', 'Object', and 'Show ROI', and buttons for 'Calc Ratio' and 'New ROI'. The bottom section has 'Measure', 'Modes', and 'Advanced' buttons. Eight numbered callouts (1-8) are placed over the interface, corresponding to the feature descriptions on the right.

1. View

Settings regarding how the image is shown

- View mode quick access buttons
- View modes: live, modulation, phase, picture-in-picture
- Image averaging for smoother video display
- Reference mode for double exposure mode
- Highlight of saturated pixels, for detecting sub-optimal camera conditions
- Dual monitor display for computer operator and experimenter to see video stream
- Button to toggle use of number pad for shortcut keys

2. Image / Video Capture

- Four modes of saving: Image, Video, Time-Lapse, Strobe Video, and Strobe Images
- Automatic sequential numbering, saving in multiple formats (JPEG, RTI) for images
- Video saved in LVVID format to allow for metadata on every frame
- Stroboscopic acquisition synchronizes with the phase of the strobe signal

5. Strobe & Stimulus

- Controls synchronized AOM and speaker: frequency, amplitude, and phase

6. Digital Holography

- Controls the reconstruction distance of the digital holography algorithm

3. Exposure

- Manually or automatically set the camera's exposure time
- "Auto" button sets the exposure to the maximum value that does saturates a minimal number of pixels, while giving a bright image

7. ROI / Beam

- Select a region of interest for beam ratio calculation and other tools
- Enable and disable reference / object beams individually
- Automatically calculate the ratio of the two beams in a region of interest using shutters to turn beams off and on, as needed

4. Shifter

- Enables, disables, and sets voltage of the piezo
- Additional controls in the button's menu give calibration routines to determine the optimal voltage settings

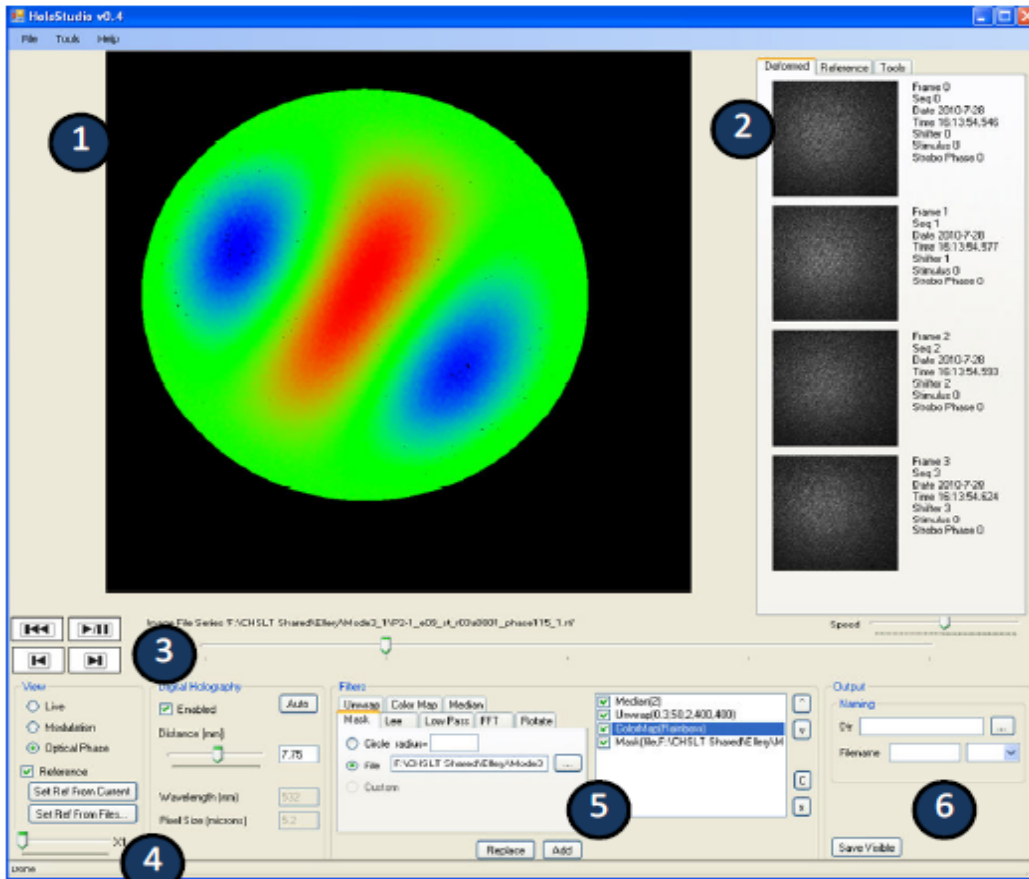
8. Additional Buttons

- Measure: gives live image analysis tools, such as histogram and cross section
- Modes: gives application-specific tools such as adjustable laser wavelength control and fringe projection .
- Advanced: Experimental tools being tested (ex. analog input triggering)

Fig. 4.4. Screenshot of LaserView's main window, with descriptions of its primary features, (Harrington et al., 2011).

4.4.2 HoloStudio

HoloStudio is a post-processing software to load and process holographic data by application of digital holographic algorithms and filters. It can load parameters and properties of holographic images or videos captured by LaserView, such as reconstruction distance, wavelength of light, pixel size of the camera, frames and so on. A collection of filters are used to convert the phase data into high-quality shape maps, such as unwrapping, mask, median, mean, lee, FFT, scaling, color map, 3D plot and so on. The image can be processed through different combination of filters in any order. After unwrapping and filtering, images can be saved into various formats, including RTI, JPEG, or LVVID. When saving in RTI or LVVID formats, the metadata from the recording is preserved and augmented by the filters applied (Harrington et al., 2011).



1. Resultant Image

- The image, after applying the selected holographic algorithms and filters.
- Updates on-demand, when filters or settings are changed.

2. Source Images

- Raw camera images used for this hologram

3. Timeline and navigation buttons

- When loading a video file or multiple image files, these controls scan the available frames

4. Holographic Algorithms

- Sets the algorithms to achieve the modulation or phase of the object with the proper reconstruction distance.

5. Filters

- Left, filter options
- Right, list of filters currently selected

6. Output

- Save the currently shown image to a file

Fig. 4.5. HoloStudio interface with color map applies to unwrapped phase, with descriptions of its primary features, (Harrington et al., 2011).

4.5 Representative experimental results

Representative deformation measurements of a human temporal bone were performed at MEEI. The temporal bone was from the left ear of a 65-year-old male without history of otologic disease. The incus, the extended facial recess, the roof of the epitympanum, the Eustachian tube and the jugular bulb were all drilled away to expose the medial side of the TM. The TM was painted with a solution of ZnO powder in saline to increase the amount of light reflected from the TM surface. In Fig. 4.6, the OH system illuminated the medial side of TM, which was oriented so that the surface of TM was perpendicular to the object beam. A sound and microphone coupler was placed on the lateral side of TM through the wall of ear canal. A glass sheet was used to seal the ear canal in order to isolate the sound environment. Finally, the TM was mounted onto a hollow metal tube with the dental cement, shown in Fig. 4.7.

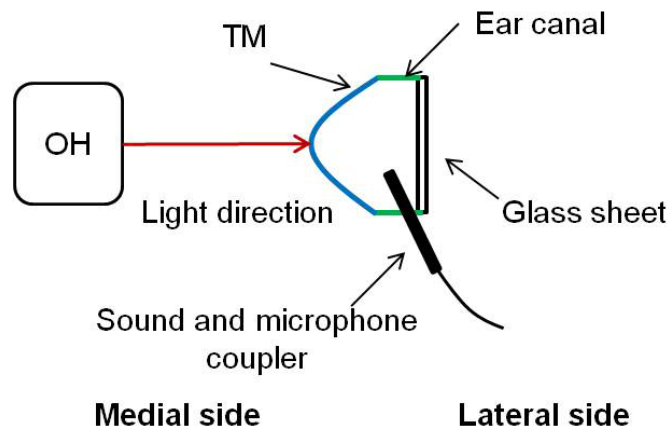


Fig. 4.6. Schematic of the illumination system.

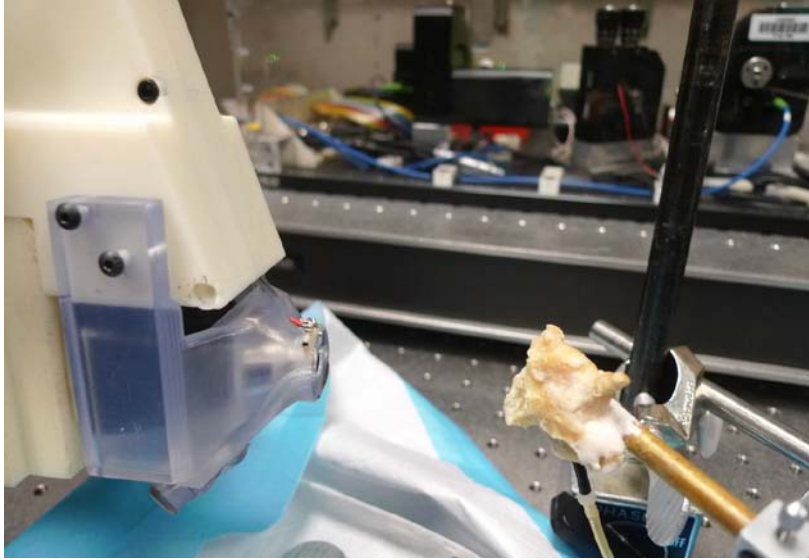


Fig. 4.7. Experimental configuration of OH system and object of human temporal bone.

Figure 4.8. shows the modulation and optical phase images that were viewed from LaserView. The umbo is the tip of manubrium of the malleus that attached to the TM, marked as U.

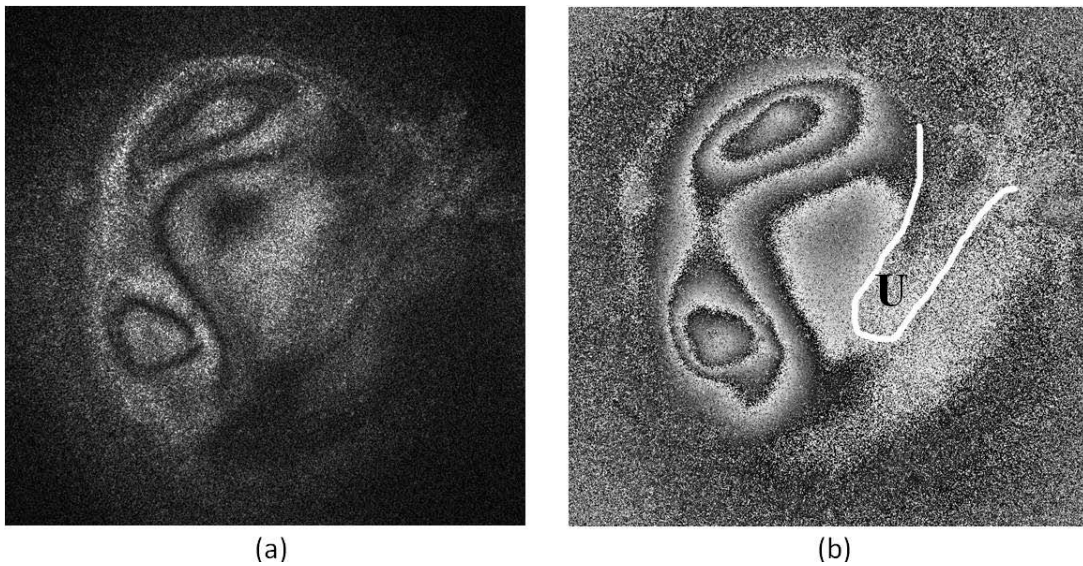


Fig. 4.8. The deformation of medial side of TM of phase 180° at sound excitation of 1 kHz: (a) modulation image, and (b) optical phase with location of umbo marked.

Figure 4.9. shows representations of deformations of medial side of TM at sound excitation of 1 kHz, from phase 0 to $7\pi/4$. Peak to peak value of the maximum is on the order of $1\mu\text{m}$.

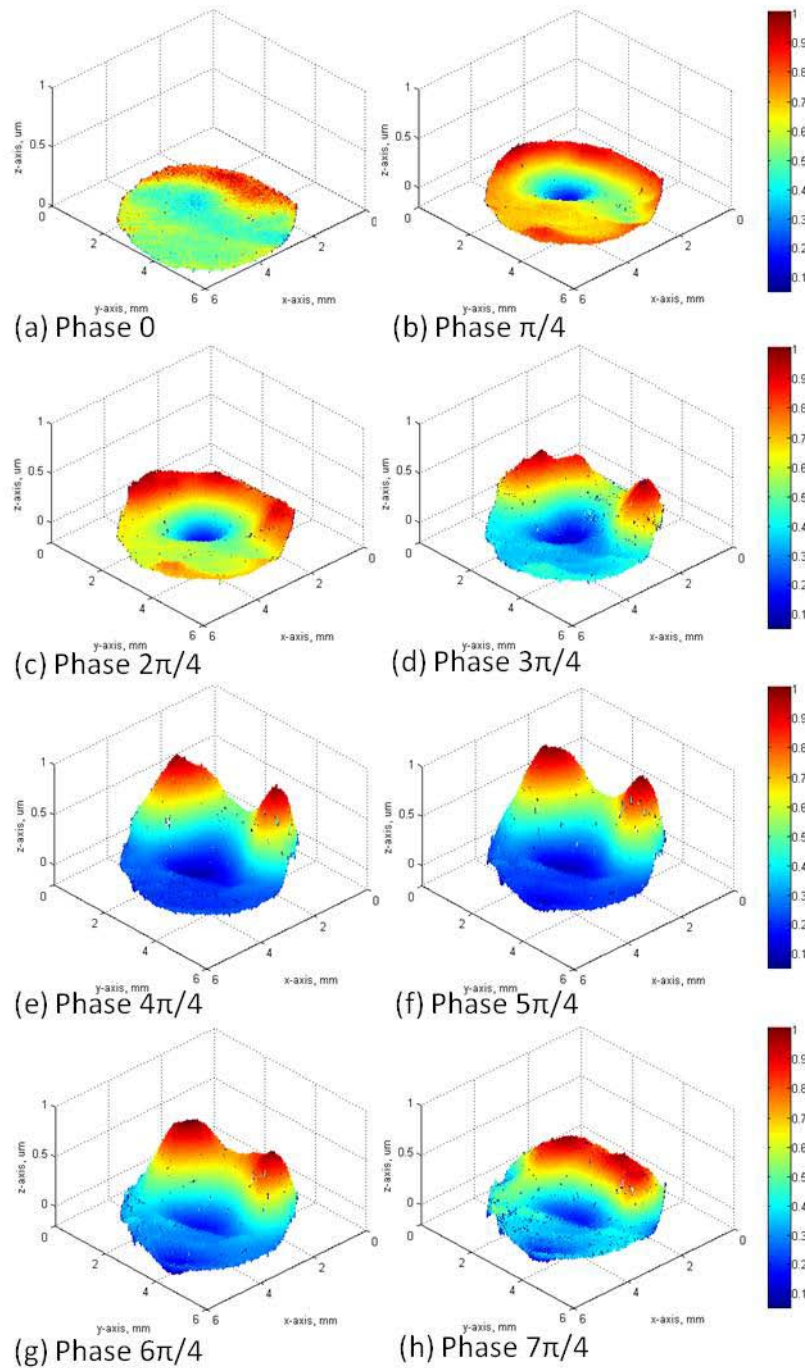


Fig. 4.9. Representative deformations of medial side of TM at sound excitation of 1 kHz, from phase 0 to $7\pi/4$.

4.6 Limitations

The DOEHS demonstrates its capabilities in lab experiments or medical research at MEEI.

However, there are two main limitations of this system:

(1) Sensitivity to external disturbances.

(2) Only one-dimensional deformation. Due to system capabilities, DOEHS can only measure one-dimensional deformation along light propagation direction, which is from object to CCD camera. However, researchers and doctors are also concerned about 3D deformations of the TM and how much these deformations influence the overall dynamic behavior of the TM.

5 Theory of multi-wavelength lensless digital holography system

5.1 Shape measurements

Shape measurements can be achieved by quantitative holographic contouring techniques. Contouring, in general, means that the modulation fringes of a three-dimensional object correspond to contours of constant elevation with respect to a reference plane (Kreis, 2005). In holographic contouring, the object under investigation is not displaced, but the two states, which by superposition form the fringe pattern, are produced by variation of either the wavelengths of the two illumination sources, the illumination or observation direction, or the refractive index that surrounds the object. In multi-wavelength lensless digital holography system (MLDHS), variation of wavelength is utilized. If the wavelength between two recordings is varied, the interference fringes can be interpreted as intersections of the object's surface with a set of ellipsoids (Kreis, 2005; Furlong and Pryputniewicz, 2000).

5.1.1 Two-wavelength technique

To determine the surface shape using MLDHS, the two-wavelength holographic contouring technique is applied to generate depth contours related to the geometry of the object. The technique is based on the utilization of a coherent and polarized light source with wavelength tuning capabilities (Furlong and Pryputniewicz, 2000). This requires acquisitions of a set of amplitude and phase information at wavelength λ_1 , considered as the reference or undeformed state, as well as acquisitions of a second set of amplitude and phase information at wavelength λ_2 , considered as the modified or deformed state. The phase difference of the two corresponding sets of data, $\Delta\phi$, is given by

$$\Delta\phi = \phi_2 - \phi_1 = \frac{2\pi}{\Lambda} OPL, \quad (5.1)$$

where ϕ_1 is the phase of the optical path length recorded at the first wavelength λ_1 , ϕ_2 is the phase of the optical path length recorded at the second wavelength λ_2 , and OPL is the optical path length defined as the distance from the illumination point to an object point and to an observation point and Λ is the synthetic wavelength given by

$$\Lambda = \frac{\lambda_1 \lambda_2}{|\lambda_1 - \lambda_2|}. \quad (5.2)$$

From Eq. 5.2, it is clear that the larger the synthetic wavelength the smaller the difference between the two wavelengths used.

In two-wavelengths contouring, the phase difference $\Delta\phi$ is equivalent to the fringe-locus function Ω described in Sec. 4.1. Therefore by applying Eq. 4.15 the phase information is a discontinuous wrapped function varying in the interval $(-\pi, \pi)$ and thus phase unwrapping algorithms are applied to obtain a continuous phase distribution for further processing (Furlong and Pryputniewicz, 2000).

If the sensitivity vector is along one axis and the illumination and the observation points are the same, then the distance between two consecutive contour lines is

$$\Delta z = \frac{\Lambda}{2}. \quad (5.3)$$

5.1.2 Multi-wavelength technique

The shape of the TM varies from patient to patient and in some cases, and extending the two-wavelength method to the multi-wavelength method has an advantage for shape measurements.

The basic idea of the multi-wavelength approach is to start with a large synthetic wavelength to avoid ambiguities of the phase because phase differences do not exceed 2π for any point on the object surface (Wagner et al., 2000). A systematic reduction of the synthetic wavelengths improves the accuracy of the measurement using the information of the preceding measurements to eliminate ambiguities (Wagner et al., 2000).

In this case, the various wavelength differences correspond to different synthetic wavelengths that have to satisfy

$$\Lambda_n = \frac{\Lambda_1 \Lambda_n}{|\Lambda_n - \Lambda_1|}, n \geq 2, \quad (5.4)$$

where Λ_n is the n 'th synthetic wavelength and so the phase difference resulting from measurement with the synthetic wavelength Λ_n is

$$\Delta\phi_n = \phi_n - \phi_1 = \frac{2\pi}{\Lambda_n} OPL, \quad (5.5)$$

leading to the depth between two consecutive contour fringes of

$$\Delta z_n = \frac{\Lambda_n}{2}. \quad (5.6)$$

5.2 Out-of-plane deformation measurements

In the original DOEHS, only out-of-plane deformations along the optical propagation axis can be measured. In this case, the four phase shifting technique is utilized with a phase shift of 90° per step and so the intensity distributions of the corresponding interferograms are

$$I_1 = I_a + I_b \cos [\psi(x, y)], \quad (5.7a)$$

$$I_2 = I_a - I_b \sin [\psi(x, y)], \quad (5.7b)$$

$$I_3 = I_a - I_b \cos [\psi(x, y)], \quad (5.7c)$$

$$I_4 = I_a + I_b \sin [\psi(x, y)], \quad (5.7d)$$

and solving the optical phase before deformations results in

$$\psi(x, y) = \tan^{-1} \left[\frac{\sin[\psi(x, y)]}{\cos[\psi(x, y)]} \right] = \tan^{-1} \left[\frac{I_4(x, y) - I_2(x, y)}{I_1(x, y) - I_3(x, y)} \right]. \quad (5.8)$$

The optical phase after deformation is

$$\begin{aligned} \psi(x, y) + \Omega(x, y) &= \tan^{-1} \left[\frac{\sin[\psi(x, y) + \Omega(x, y)]}{\cos[\psi(x, y) + \Omega(x, y)]} \right] \\ &= \tan^{-1} \left[\frac{I'_4(x, y) - I'_2(x, y)}{I'_1(x, y) - I'_3(x, y)} \right]. \end{aligned} \quad (5.9)$$

Therefore, the phase difference between these two states is

$$\Omega(x, y) = \tan^{-1} \left[- \frac{(I_1 - I_3)(I'_2 - I'_4) - (I_2 - I_4)(I'_1 - I'_3)}{(I_1 - I_3)(I'_1 - I'_3) + (I_2 - I_4)(I'_2 - I'_4)} \right], \quad (5.10)$$

which enables the measurements of out-of-plane deformations by application of Eq. 4.12.

5.2.1 Fundamentals of thin shells

The term shell is applied to bodies bounded by two curved surfaces, where the distance between the surfaces is small in comparison with other body dimensions. The locus of points that lie at equal distances from these two curved surfaces defines the middle surface of the shell. The length of the segment, which is perpendicular to the curved surfaces, is called the thickness of the shell, h . Depending the curvature of the surface, shells are divided into cylindrical (noncircular and circular), conical, spherical, ellipsoidal, paraboloidal, toroidal, and hyperbolic paraboloidal shells (Ventsel and Krauthammer, 2001).

Shells can be classified as thick or thin. A shell is classified as thin if the maximum value of the ratio of the thickness of the shell to the radius of curvature, R , of the middle surface is smaller than one. More specifically, a shell may be regarded as thin if the following condition is satisfied (Ventsel and Krauthammer, 2001):

$$\max\left(\frac{h}{R}\right) \leq \frac{1}{20}. \quad (5.11)$$

Hence, shells for which this inequality is not satisfied are referred to as thick shells. Equation 5.11 very roughly defines the boundary between thin and thick shells. In reality, it also depends on other geometrical parameters of the shells, such as boundary conditions, smoothness of a variation of external loads over the shell surface, etc (Ventsel and Krauthammer, 2001).

The theory of thin elastic shell is based on Love's assumptions (Kraus, 1967; Saada, 2009), which indicate that a shell is thin:

- (1) If the ratio of the thickness of the shell to the radius of curvature of the middle surface is smaller than one.

(2) If the deflections of the shell are small, and the strains in the direction of the normals are small enough to be neglected. This assumption allows us to refer the analyses to the initial configuration of the shell.

(3) The transverse normal stress is negligible.

(4) The shear strains that cause the distortions of the normals to the middle surface can be neglected. This means that the normals to the undeformed middle surface remain normal to it after deformations.

5.2.2 Main proposed approach

Conventional methods for measurement of 3D deformations of objects by holographic interferometry use at least three illumination points or three observation points to define three sensitivity direction vectors. In our case, a new method has been developed in which we utilize one-dimensional deformation measurements together with object shape information, to calculate deformations in the other two orthogonal directions. This is a big hypothesis of this project. The information captured from holographic system is the shape of an object before applying the acoustic signal and the deformation along optical axis (z axis) when the sound is turned on. 3D decompositions of surface normal vectors can be calculated based on shape information. Therefore by combining with z -axis deformation, x -axis and y -axis deformations can be computed (Fig. 5.1).

The hypothesis is followed by three assumptions: (1) the TM is analyzed as a thin shell. Based on the literature research, in many cases, the ratio of the TM thickness to the radius is less than $1/50$, which is very small; (2) the motions of the TM are along the directions of the surface

normal vectors; (3) the deformation of the TM is very small so that the shape before and after deformation can be considered as the same. Based on the experiment results, the deformation of the TM is in nanometer scale, while the shape of the TM is in millimeter scale.

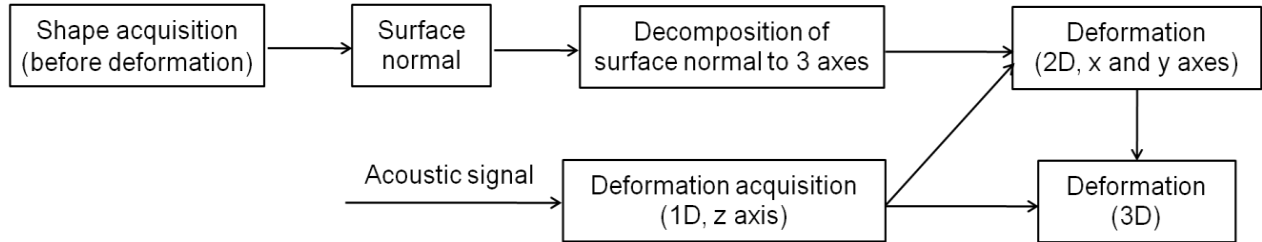


Fig. 5.1. The algorithm used to extract 3D deformations by measurements of shape and only one component of deformation.

Based on the proposed approach, angles between deformations in x , y , z directions and the resultant deformation are the same as angles between normal vectors in x , y , z directions and the normal vector (Fig. 5.2).

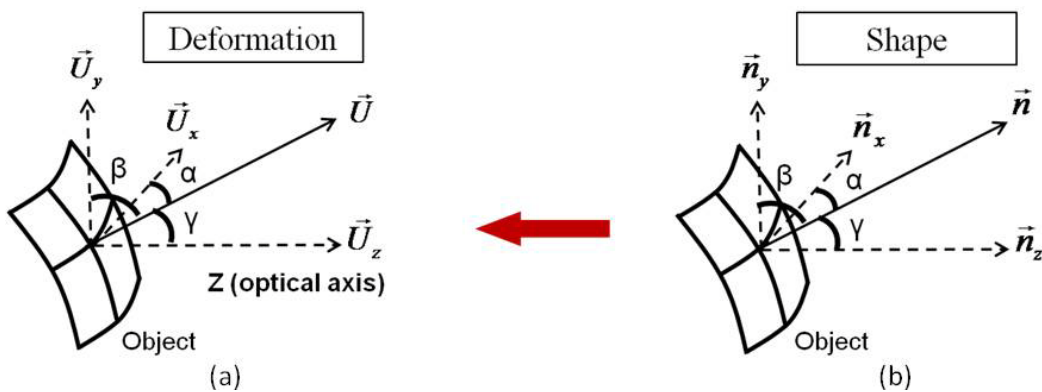


Fig. 5.2. Configuration of decompositions of the resultant deformation and the normal vector. \vec{U} is the resultant deformation; \vec{U}_x , \vec{U}_y and \vec{U}_z are the decompositions of \vec{U} along x , y and z axes; \vec{n} is the normal vector; \vec{n}_x , \vec{n}_y and \vec{n}_z are the decompositions of \vec{n} along x , y and z axes; α , β and γ are the angles between the direction of \vec{U} or \vec{n} and x , y , z axes.

The main equations that correlate the decomposition of deformations with the decomposition of the normals are as follows:

$$\cos\alpha = \frac{\vec{U}_x}{\vec{U}} = \frac{\vec{n}_x}{\vec{n}}, \quad (5.12a)$$

$$\cos\beta = \frac{\vec{U}_y}{\vec{U}} = \frac{\vec{n}_y}{\vec{n}}, \quad (5.12b)$$

$$\cos\gamma = \frac{\vec{U}_z}{\vec{U}} = \frac{\vec{n}_z}{\vec{n}}. \quad (5.12c)$$

After transformation,

$$\frac{\vec{U}_x}{\vec{n}_x} = \frac{\vec{U}_y}{\vec{n}_y} = \frac{\vec{U}_z}{\vec{n}_z} = \frac{\vec{U}}{\vec{n}}, \quad (5.13)$$

in which \vec{U}_z is measured directly by the optical setup, and \vec{n}_x , \vec{n}_y , \vec{n}_z are calculated from shape information. Thus, x -axis and y -axis deformations can be calculated

$$\vec{U}_x = \vec{n}_x \frac{\vec{U}_z}{\vec{n}_z}, \quad (5.14a)$$

$$\vec{U}_y = \vec{n}_y \frac{\vec{U}_z}{\vec{n}_z}. \quad (5.14b)$$

5.2.3 Validation of the proposed approach

In order to validate the proposed approach, under analysis by either finite element analysis (FEA) or analytical solutions can be utilized. In this work, validation by FEA is done in SolidWorks' simulation, and all additional calculations and data plotting are processed in Matlab.

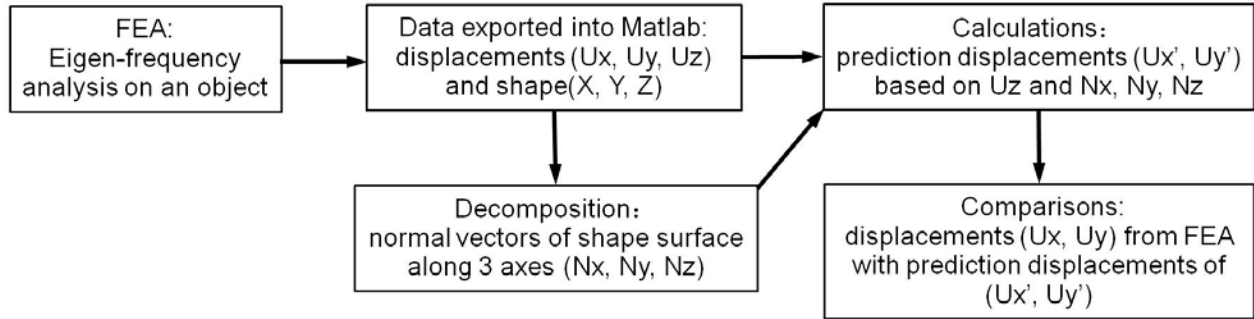


Fig. 5.3. The flow chart of the validation approach that was applied.

(1) Validation on an ideal object.

The ideal object is a semi-spherical shell that meets all of the assumptions described in previous Sections. Geometry, mechanical properties, and modeling parameters incorporated into the FEA model analysis of this object are listed in Table 5.1 and the geometry of a cross-section is shown in Fig. 5.4. Damping is not considered in this case.

Table 5.1. Geometry, mechanical properties, and basic FEA parameters of an idea object.

Geometry		Mechanical properties		FEA parameters	
Spherical radius	5mm	Young's modulus	115GPa	Degrees of freedom	44895
Thickness	17.8 μ m	Poisson's ratio	0.33	No. of nodes	15697
Central angle	60°	Mass density	8890kg/m ³	No. of elements	7747

Boundary conditions: fully constrained along entire perimeter.

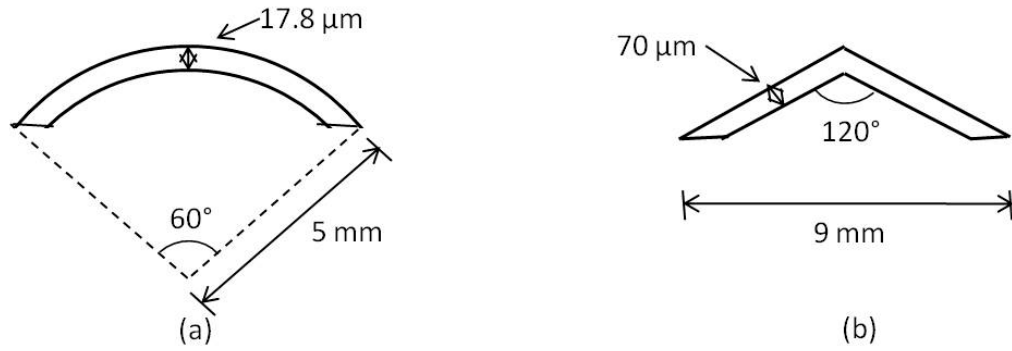


Fig. 5.4. 2D geometries of (a) ideal partial spherical object, and (b) TM model.

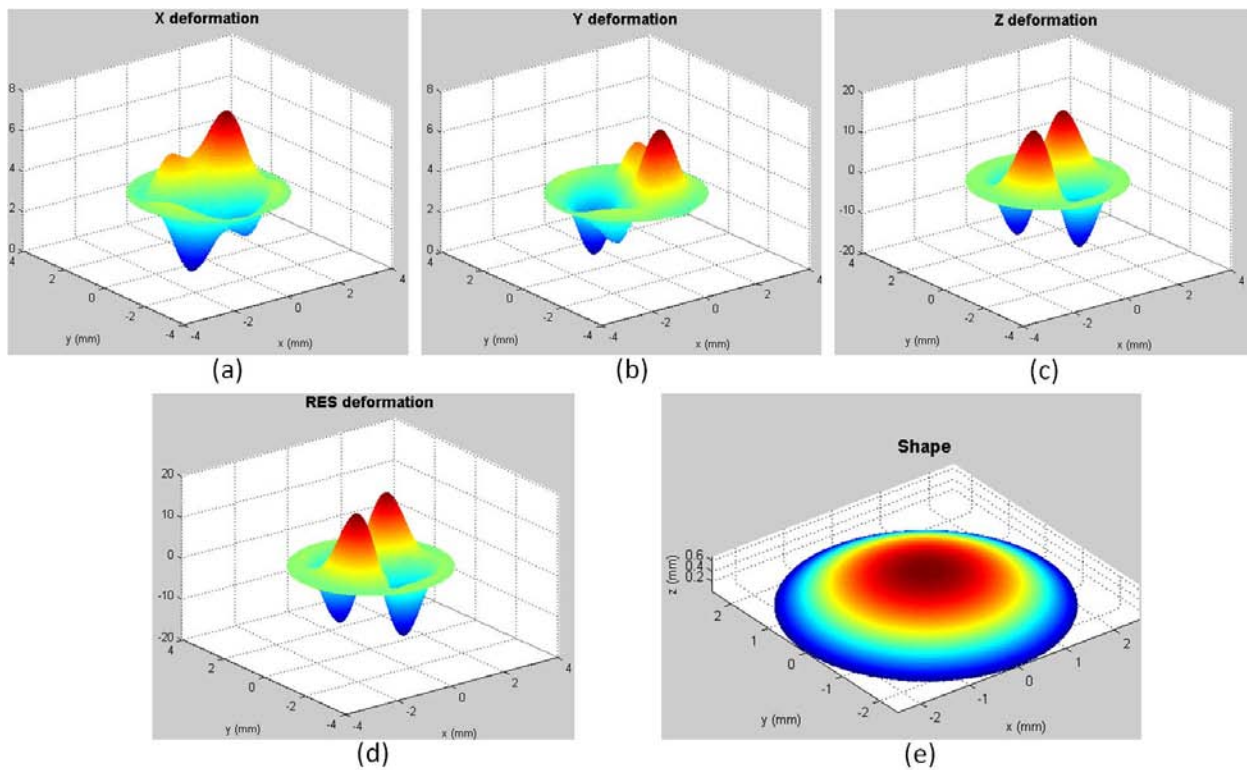


Fig. 5.5. FEA solutions for modal analysis of the 4th mode of vibration of an ideal object: (a) x -axis deformation (\mathbf{U}_x), (b) y -axis deformation (\mathbf{U}_y), (c) z -axis deformation (\mathbf{U}_z), (d) resultant deformation, and (e) object shape.

Output data of modal analysis solutions from FEA are the resultant deformations as well as deformations along the x , y , and z axes, and object shape coordinates. By taking the 4th mode of vibration for example (Fig. 5.5), and by applying Eq. 5.14, the predicted deformations U_x' and U_y' are calculated and plotted in Fig. 5.6.

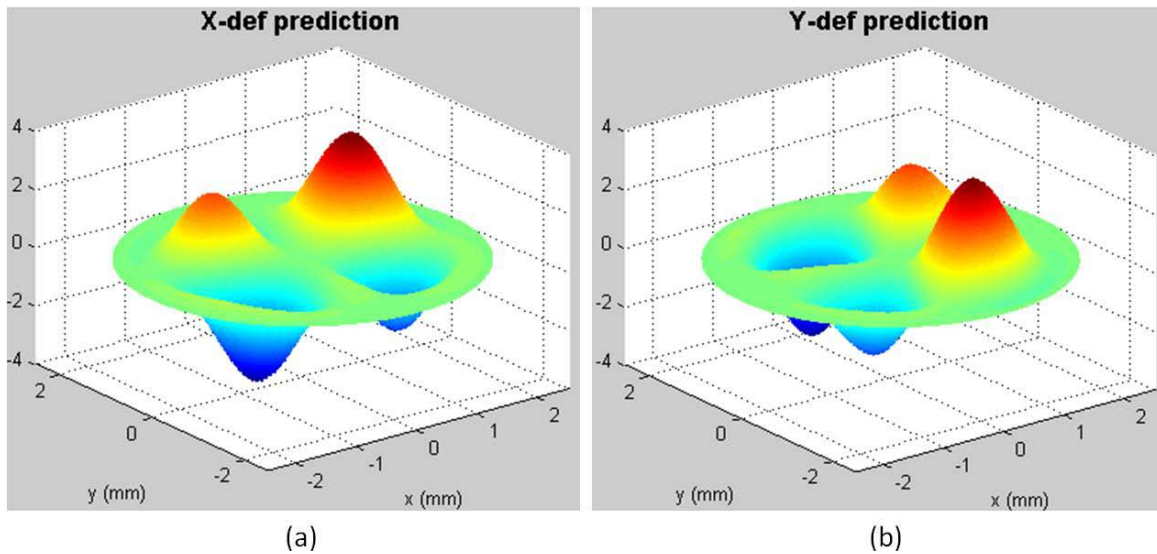


Fig. 5.6. (a) Predicted deformations in the x direction (U_x'), and (b) predicted deformations in the y direction (U_y'). Computed x and y components of deformations obtained by applying proposed approach. Results should be compared with these shown in Figs. 5.5(a) and 5.5(b).

A significant criterion for validating the proposed approach is the difference between the deformations from FEA solutions (U_x, U_y) and the predictions (U_x', U_y'). A possibility that would affect the difference is the amplitude of the FEA solutions and the amplitude of the predictions. Since eigenvectors provided by FEA are not normalized, therefore, in order to eliminate this effect, data from both FEA solutions and predictions need to be normalized. The comparisons after normalization are shown in Fig. 5.7.

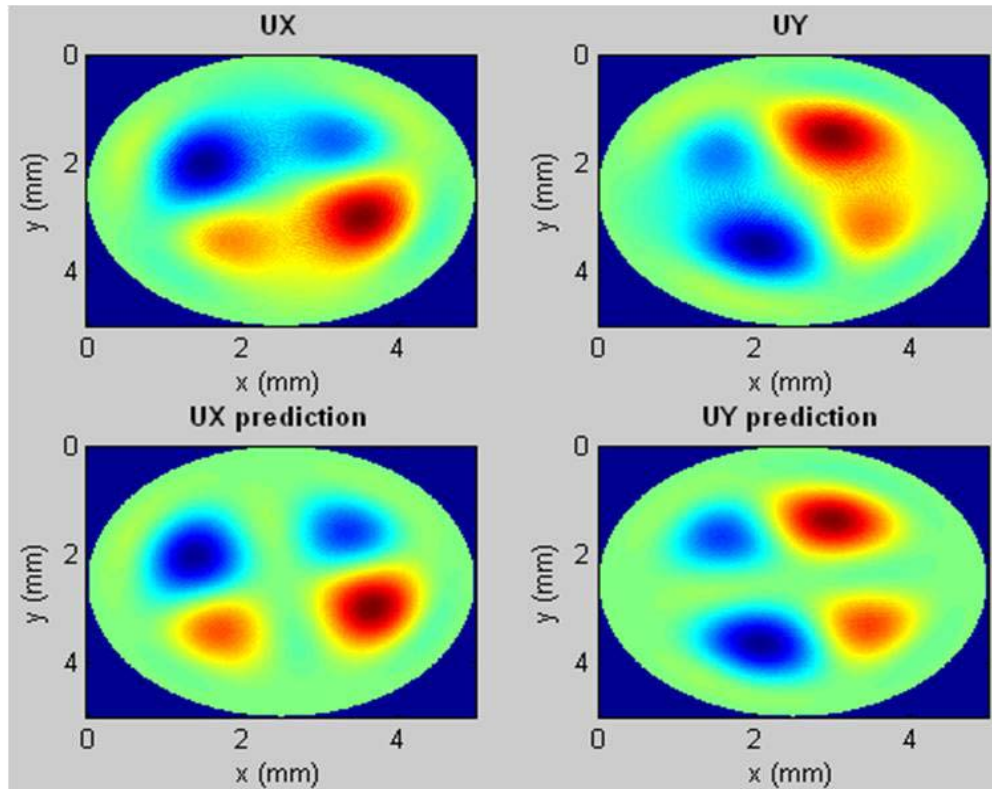


Fig. 5.7. Comparisons of deformations between FEA solutions ($\mathbf{U}_x, \mathbf{U}_y$) and predictions ($\mathbf{U}_x', \mathbf{U}_y'$) after data normalization.

Table 5.2. RMS and STD of the difference between FEA solutions and predictions of different modes for an ideal object.

Difference		Mode 1	Mode 2	Mode 3	Mode 4
x	RMS (%)	3.08	3.52	3.18	0.71
	STD (%)	3.10	4.18	2.91	0.90
y	RMS (%)	3.11	3.38	3.52	0.71
	STD (%)	3.12	3.07	4.30	0.91

Table 5.2 shows the root mean square (RMS) and standard deviation (STD) of the differences between FEA deformations and predicted deformations for different modes of vibration after data normalization. Results show that the maximum difference is less than 5%, which indicates that the predicted deformations correlate with the computed FEA deformations well within accurate numerical resolutions.

(2) Validation on a TM model

Assumptions have been validated successfully on an ideal object. The next step is to validate the proposed approach on an object that has a similar geometry as the one of a human TM. This TM model made in conical shape is shown in 2D in Fig. 5.4(b). Geometry, mechanical properties, and basic parameters are listed in Table 5.3. By taking the 4th vibration mode of vibration for example, the differences between FEA solutions (U_x, U_y) and predictions (U_x', U_y') are computed and are shown in Fig. 5.8.

Table 5.3. Geometry, mechanical properties, and basic FEA parameters of a geometry similar to a human TM.

Geometry		Mechanical properties		FEA parameters	
Radius	4.5mm	Young's modulus	50MPa	Degrees of freedom	44292
Thickness	70 μ m	Poisson's ratio	0.45	No. of nodes	15457
Central angle	120°	Mass density	1100kg/m ³	No. of elements	7640

Boundary conditions: fully constrained along entire perimeter. Geometry and mechanical properties are selected based on Decraemer's paper (Decraemer and Funnell, 2008).

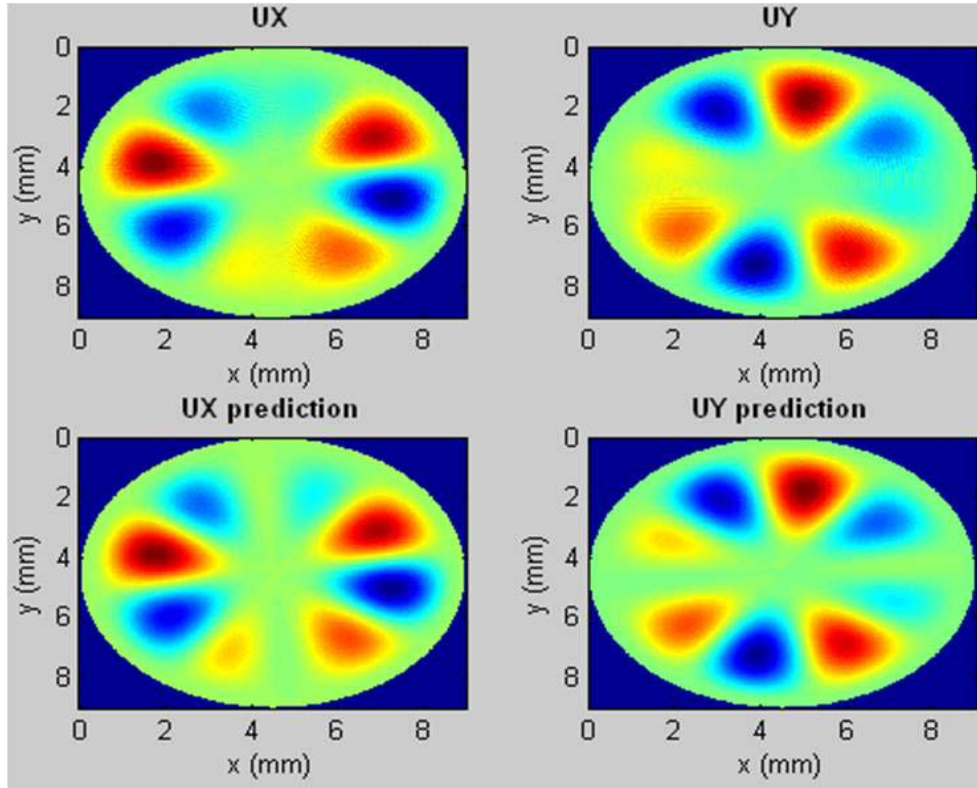


Fig. 5.8. Comparisons of deformations between FEA solutions (U_x, U_y) and predictions (U_x', U_y') after data normalization.

Table 5.4 shows the RMS and STD of the difference between FEA solutions and predictions after data normalization from mode 1 to mode 4. Results indicated that the difference is within 1% and the proposed approach works better on the conical object than on the spherical ideal object.

Table 5.4. RMS and STD of the difference between FEA solutions and predictions in different modes

Difference		Mode 1	Mode 2	Mode 3	Mode 4
<i>x</i>	RMS (%)	0.43	0.45	0.22	0.22
	STD (%)	0.61	0.61	0.34	0.34
<i>y</i>	RMS (%)	0.44	0.45	0.23	0.23
	STD (%)	0.60	0.64	0.35	0.35

5.2.4 Accuracy of the proposed approach

An important parameter that influences the predicted deformations is the surface normal vector of the object. Normal vectors calculations are implemented in Matlab are based on a bicubic fit of the data in *x*, *y*, *z* axes. In order to measure the accuracy of this calculation, normal vectors computed with Matlab are compared with analytical solutions of normal vectors on the ideal object shown in Fig. 5.4(a).

If *x* axis is fixed, a circle centered at the origin (0, 0) in two dimensions is

$$y^2 + z^2 = r^2 \quad (5.15)$$

and the normal vectors of this circle are computed through the first partial derivatives

$$f_y = 2y, \quad (5.16a)$$

$$f_z = 2z. \quad (5.16b)$$

After normalization, the normal vectors in y and z axes are given by

$$N_y = \frac{2y}{\sqrt{(2y)^2 + (2z)^2}}, \quad (5.17a)$$

$$N_z = \frac{2z}{\sqrt{(2y)^2 + (2z)^2}}. \quad (5.17b)$$

Figure 5.9 shows comparisons between the analytical solution and Matlab solution of normal vectors of the semi-spherical object. The blue curve represents the surface contour of the object in 2D; green arrows represent the analytical solution of normal vectors in original length; red arrows represent the Matlab solution of normal vectors in a ratio of 0.8 with respect to the original length. It is clear to see that the Matlab solutions overlap with the analytical solution. The RMS of the differences is on the order of 0.04%.

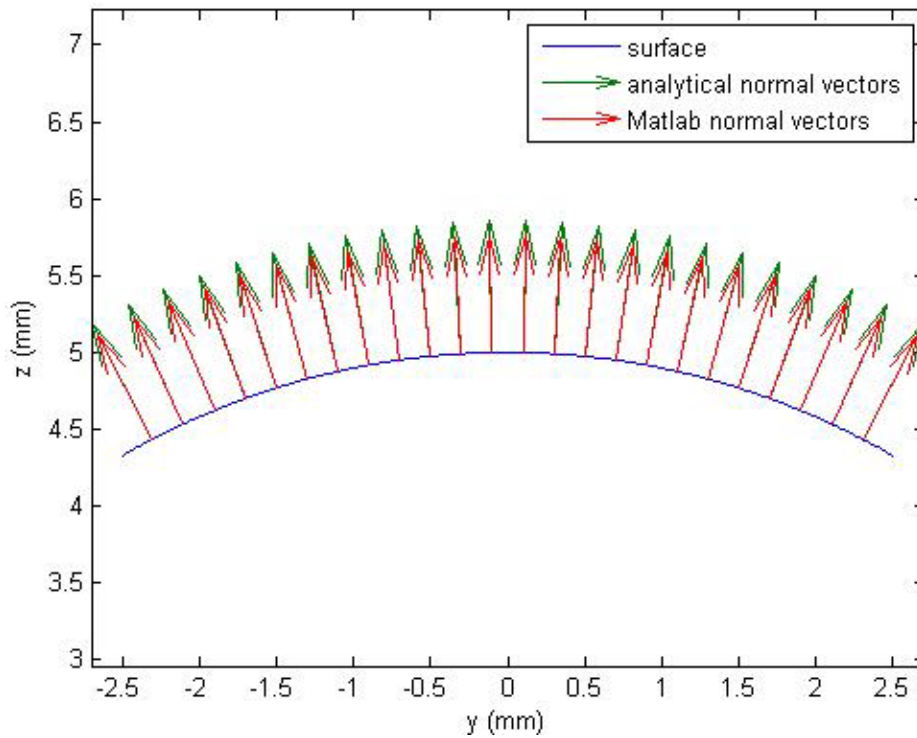


Fig. 5.9. Normal vectors plot of analytical solution (original length) and Matlab solution (0.8 of original length).

5.2.5 Effect of thickness on this thin shell formulation

Although the thickness to radius ratio of a thin shell obtained from many practical engineering applications is smaller than $1/20$ (Eq. 5.11), it is highly recommended to find out an appropriate ratio for our own application. Therefore, we changed the thickness to radius ratio starting from $1/20$, and compute the difference between the FEA solutions and predictions of deformations in modal analysis module both on a spherical object and a conical object. In this case, this difference highly relies on the FEA solution, which is considered as the standard.

Geometries of the objects used in the simulation are shown in Fig. 5.4. The only parameter changed is the thickness. Mechanical properties used are listed in Table 5.2. The entire perimeter of the object is specified as fully-constrained as a boundary condition.

(1) Spherical object

In Table 5.5, the difference between the FEA solutions and predictions of first mode deformations is presented and the RMS of each case is not big. However, by analyzing the data, when the thickness to radius ratio is $1/20$ the deformation plot is very noisy. And the bigger the ratio is, the noisier the deformation plot is. This phenomenon is due to the numerical resolution of the commercial FEA software used. To eliminate the influence of this limitation, the same simulation is run in ANSYS and in COMSOL. Figure 5.10 shows the x -axis deformation plot of mode 1 generated by ANSYS when the thickness to radius ratio is $1/20$. It is obvious to see that the plot is very noisy similar to the one obtained by SolidWorks, which means that changing FEA software does not make any difference in this case.

Table 5.5. FEA solution plot of mode 1 deformation in x axis with different thickness to radius ratio and the corresponding RMS of the difference between FEA solution and prediction.

Thickness/radius	RMS (%)	FEA solution of deformation along the x -axis (mode 1)
1/20	x axis: 11.05 y axis: 11.08	
1/40	x axis: 10.90 y axis: 12.26	
1/80	x axis: 10.09 y axis: 4.71	
1/160	x axis: 4.12 y axis: 4.16	

A trend seen from Table 5.5 is that as the thickness to radius ratio decreases, the magnitude of x -axis deformation increases. It means at a small thickness to radius ratio like 1/20, the magnitude of deformation is so small that the algorithm in FEA software does not provide sufficient resolution.

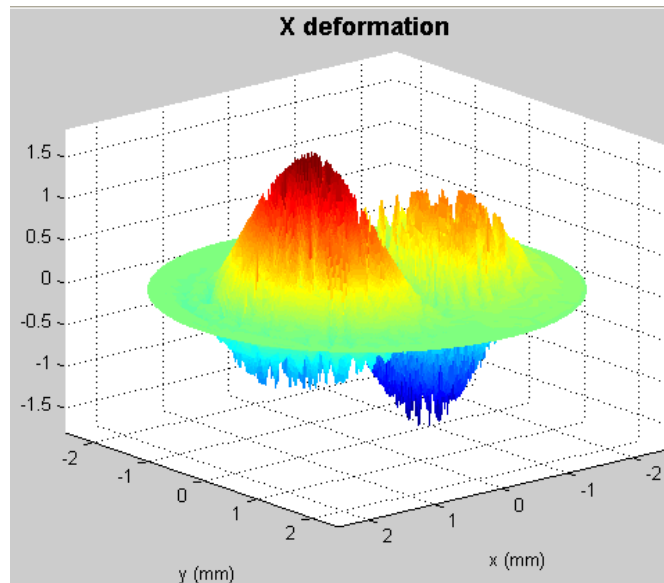


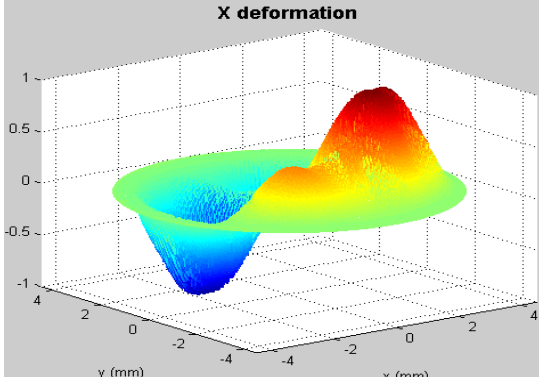
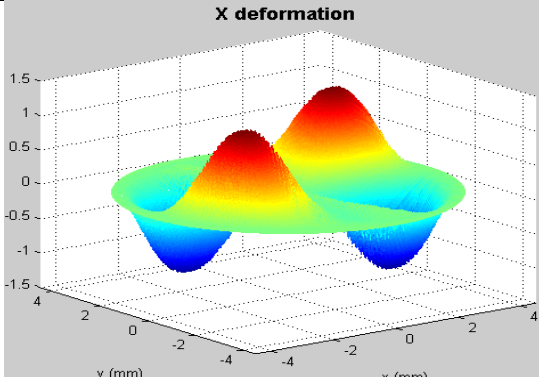
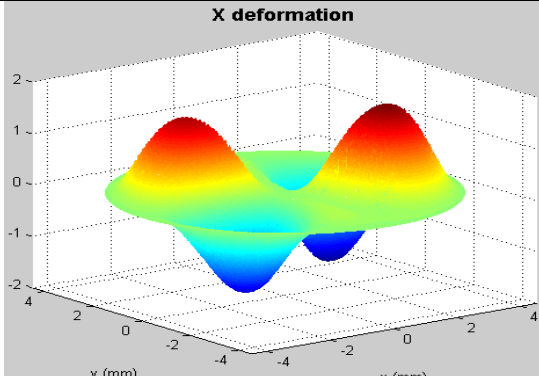
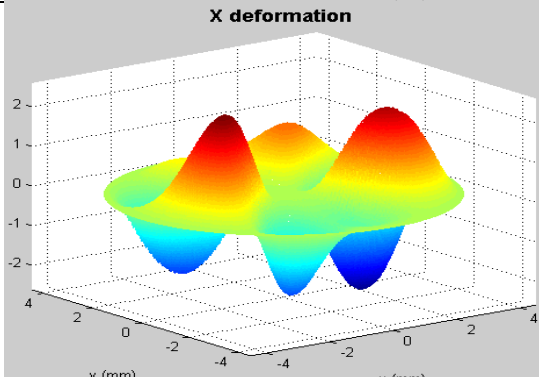
Fig. 5.10. FEA solution of deformation along x axis (mode 1) computed by FEM (ANSYS) when the thickness to radius ratio is 1/20.

(2) TM model

Table 5.6 shows the differences between FEA solutions and predictions of the first mode of vibration with respect to different thickness to radius ratio. Though there is the same trend that the bigger the ratio is the noisier the deformation plot is, the x -axis component of deformation for the TM model is much smoother than the one of spherical object. This phenomenon is due to the geometry of the object itself.

In order to find more accurate thickness to radius ratio of a thin shell, further research needs to be done needs to be done by analytical solution in the future.

Table 5.6. FEA solution plot of mode 1 deformation in x axis with different thickness to radius ratio and the corresponding RMS of the difference between FEA solution and prediction.

Thickness/radius	RMS (%)	FEA solution of deformation along the x -axis (mode 1)
1/20	x axis: 2.09 y axis: 2.09	
1/40	x axis: 1.90 y axis: 2.25	
1/80	x axis: 1.36 y axis: 1.91	
1/160	x axis: 0.45 y axis: 0.38	

6 Development of multi-wavelength lensless digital holography: experimental verifications

The multi-wavelength lensless digital holography system (MLDHS) consists of a laser delivery (LD), optical head (OH), and computing platform (CP) subsystems. One version of the LD, shown in Fig. 6.1 and Fig. 6.2, houses two tunable near-infrared external-cavity diode lasers with central wavelength of 780.24 nm and 779.74 nm, an acousto-optic modulator, and a laser-to-fiber mechanism. The output of the LD is delivered to the ultra-fast MEMS based fiber optical switch and the light beam comes out to the OH, which is arranged to perform imaging and measurements by phase-shifting holography.

The second version of the LD subsystem contains one tunable near-infrared diode laser in the range from 770 nm-789 nm with central wavelength 779 nm, an anamorphic prism pairs, an acousto-optic modulator, a half-wave plate, and a fiber coupler assembly. The output of LD is delivered to the OH directly. The OH is designed by 3D optical ray tracing simulation in which components are rotated in specific angles to overcome reflection issues. A high-resolution digital camera with pixel size of 6.7 μm by 6.7 μm in OH is used for image recording at high-rates while the CP acquires and processes images in either time-averaged or double-exposure modes. Working version depends on the requirements of the measurement and the tested sample.

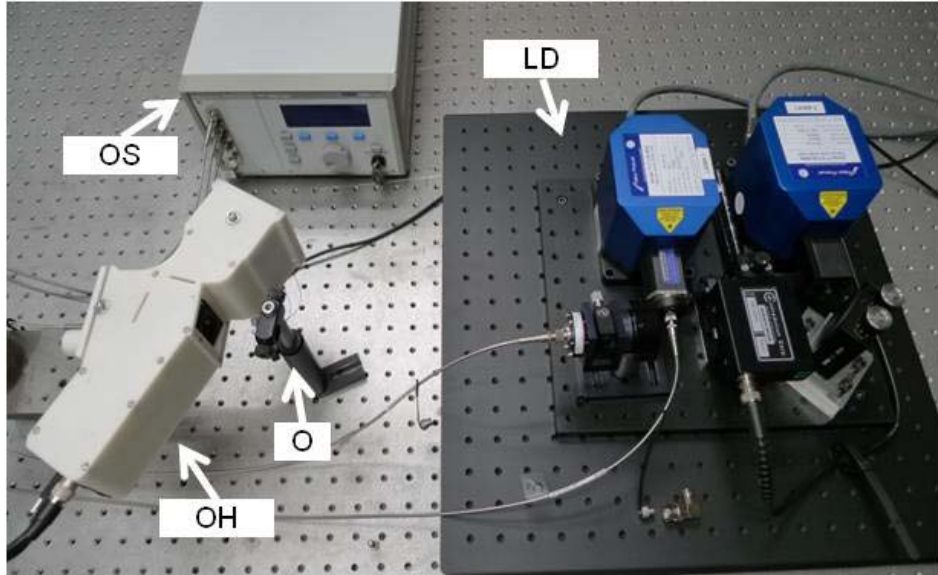


Fig. 6.1. Experimental setup of the multi-wavelength lensless digital holography system.

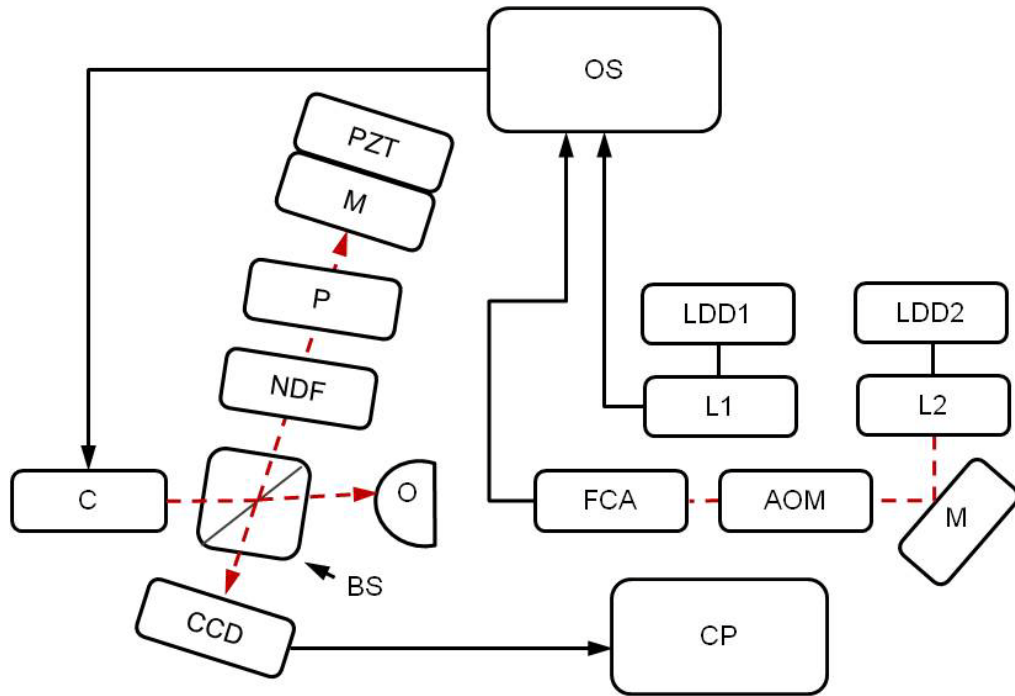


Fig. 6.2. Schematic of the multi-wavelength lensless digital holography system: LDD is the laser diode driver, L is the laser, M is the mirror, AOM is the acousto-optic modulator, FCA is the fiber coupler assembly, OS is the optical switch, C is the collimator, BS is the beam splitter cube, PZT is the piezoelectric transducer, P is the polarizer, NDF is the neutral density filter, CCD is the CCD camera, O is the object, and CP is the computer platform.

6.1 Laser delivery system

The LD system is the light source system. The design requirements for the LD system are the stability of light, high light transportation efficiency, enough light power to support good contrast of the observation image, and compactness. Therefore, choosing appropriate components for the LD system is a key factor in the whole design.

Two versions of the LD system are developed in the lab. Different generations mainly depend on different lasers that come along with different configurations and components. In order to measure the shape of the TM, holographic contouring techniques are used, which needs at least two different wavelengths for measurements. There are two options for the laser system:

(1) Use two lasers (Vortex II-TLB 6900 (0055) and Vortex II-TLB 6900 (0078)) with different wavelengths and an OS that can switch between these two lasers. It is very crucial to choose the best synthetic wavelength for a specific shape of the object. Therefore, these two lasers need to be tunable so that the LD system can generate different synthetic wavelengths for different cases.

(2) Use only one tunable laser (Velocity TLB 6312) in LD system with a wide range of wavelength and one can change from one wavelength to the other by changing the settings of the laser diode controller.

The near-infrared tunable lasers used in LD system are shown in Table 6.1.

Table 6.1. The near-infrared tunable lasers used in LD system.

	Velocity TLB 6312	Vortex II-TLB 6900 (0055)	Vortex II-TLB 6900 (0078)
Wavelength range	770-789 nm	780.04-780.36 nm	779.54-779.86 nm
Central wavelength	779 nm	780.24 nm	779.74 nm
Output power	8.7 mW	50 mW	50 mW

6.1.1 1st version

Figure 6.2 shows the components contained in the 1st version of LD system: two tunable lasers, a mirror that transports the light beam to the next component, an acousto-optic modulator (AOM), a fiber coupler assembly, fibers and an optical switch (OS).

6.1.1.1 Components

1. Laser

Two tunable external cavity diode lasers (TLB-6900 Vortex series) are used to generate the light source. Vortex II-TLB 6900 (0055) is a laser that has a fiber connector so that the output beam can be directly delivered into a fiber. Vortex II-TLB 6900 (0078) has no fiber connector in the outlet and it needs a FAC to aim the beam into the fiber. In order to measure deformations of an object, an AOM, which is used in the stroboscopic mode for deformation measurement, needs to be inserted between the laser and the fiber. Therefore, Vortex II-TLB 6900 (0078) is eligible for the deformation measurement. Figure 6.3 shows the power distribution in LD system. The

output power of Vortex II-TLB 6900 (0078) is 22.4 nm and the output power of Vortex II-TLB 6900 (0055) is adjusted to 22.1 mW when the current of both is 100 mA.

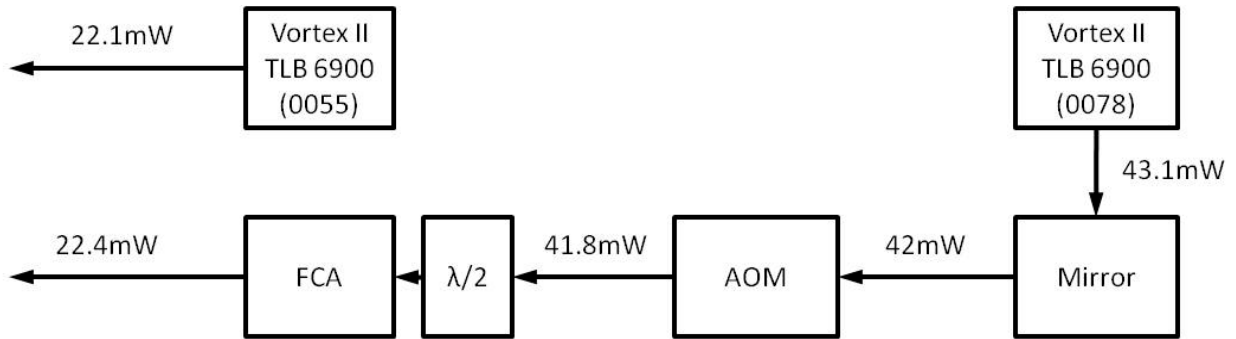


Fig. 6.3. Power distribution of Vortex II-TLB 6900 (0055) and Vortex II-TLB 6900 (0078).

The wavelength is mainly controlled by the voltage to the Vortex lasers which is from 0 V to 100 V. Based on the manual, it is recommended to use voltage range 40 V-100 V. Table 6.2 shows the wavelength with respect to a certain voltage of Vortex series lasers measured by Burleigh WA-1500 wavemeter.

Table 6.2. Wavelength with respect to voltage of Vortex series lasers.

Voltage (V)	40	50	60	70	80	90	100
Wavelength(0055) (nm)	780.09	780.13	780.16	780.20	780.24	780.27	780.31
Voltage (V)	40	50	60	70	80	90	100
Wavelength(0078) (nm)	779.70	779.72	779.74	779.77	779.80	779.84	779.86

Strengths of using these two tunable lasers: first, they have enough light power for measurements on the translucent TM; second, it has a relative wide synthetic wavelength range, from 1.00 mm to 2.65 mm; third, no instability issue when switching from one wavelength to the other. Figure 6.4 shows power stability after laser light changed from Vortex II-TLB 6900 (0055) to Vortex II-TLB 6900 (0078) by OS in a time window of 60 seconds. Sample was taken every 1 second and was read by a photodiode power meter. It is clear that the OS won't influence the stability of each laser and the wavelength change process can be finished within a second.

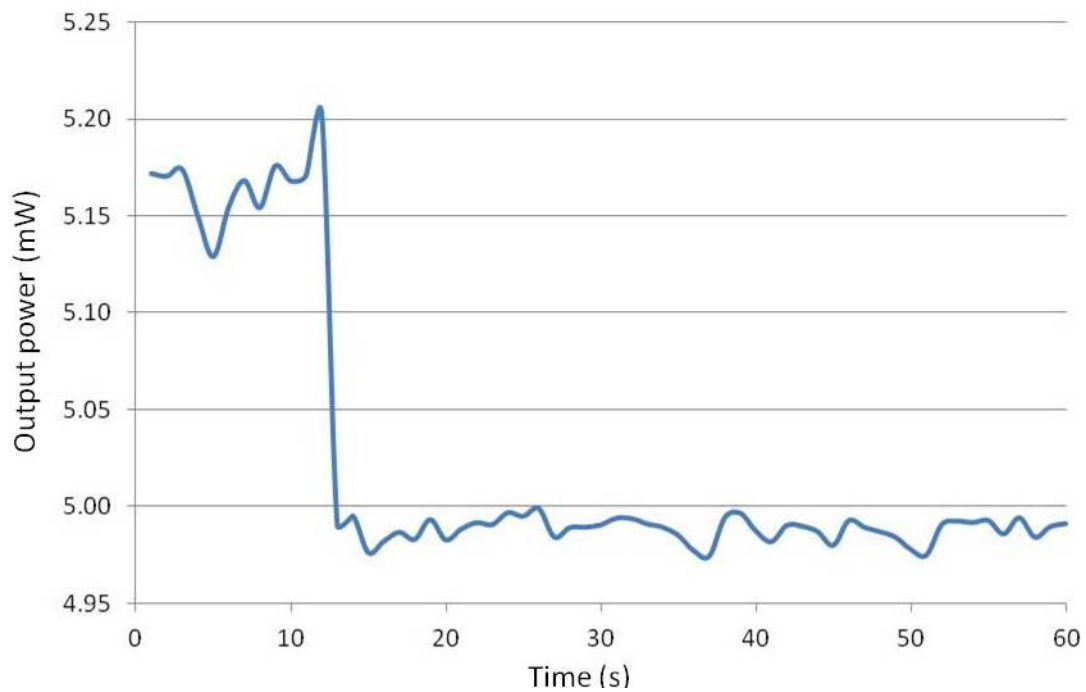


Fig. 6.4. Power stability after laser light changed from Vortex II-TLB 6900 (0055) to Vortex II-TLB 6900 (0078) by OS.

2. Mirror

A mirror placed at a 45° angle with respect to the output beam from a laser can rotate a 90° angle of the beam trail, so that it greatly reduces the room and compacts the LD system. There are three types of commercial mirrors with protected aluminum, silver or gold coatings and based on the product introduction each one can be used in the near-infrared laser situation. In order to find out which one has the highest reflectivity for 780 nm wavelength laser beam, three experiments were performed, and results are shown in Fig. 6.5. The beam power was measured by a photodiode power meter and the reflective efficiency was calculated in percentage. Results show that mirrors with protected gold or silver coating are more efficient than the protected aluminum coating mirror. After comparison, a protected gold coated mirror is an appropriate choice, with a reflective efficiency around 97.46%. Model number is ME1-M01, from Thorlabs Inc.

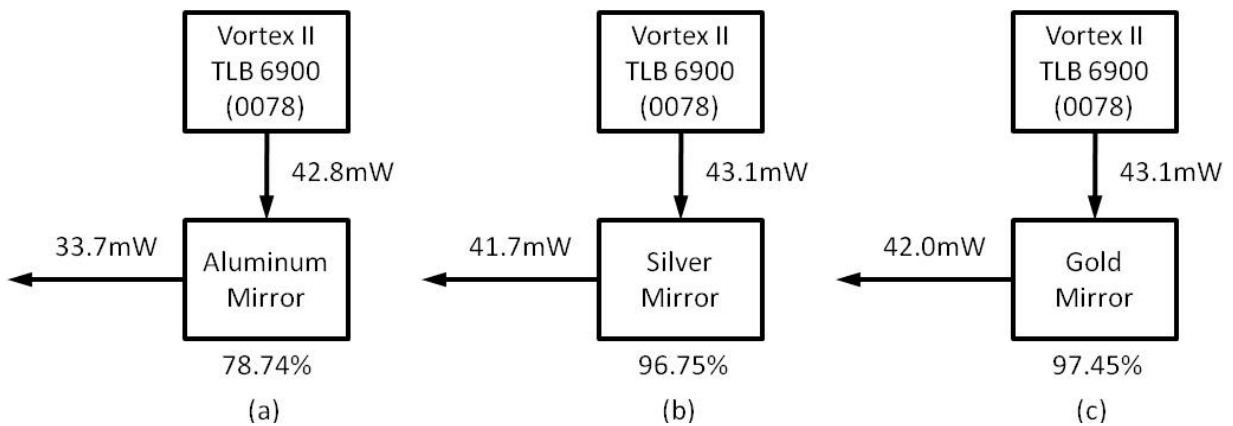


Fig. 6.5. Comparison of mirror with protected (a) aluminum, (b) silver, and (c) gold coating.

3. Acousto-optic modulator (AOM)

We use a flint glass based AOM with 3 mm active aperture height bought from IntraAction Corp. The model number is AOM-403AF3. After test, the percent of laser beam passing through AOM is around 99.5% and AOM can keep the output power very stable. Figure 6.6. shows the power stability of the output beam of AOM measured by photodiode power meter. The time window was 30000 seconds and the sample was taken every 1second. Results show that the variation is about 0.1 mW with respect to almost 34 mW beam power which means the beam power is around 0.3% variation after using AOM.

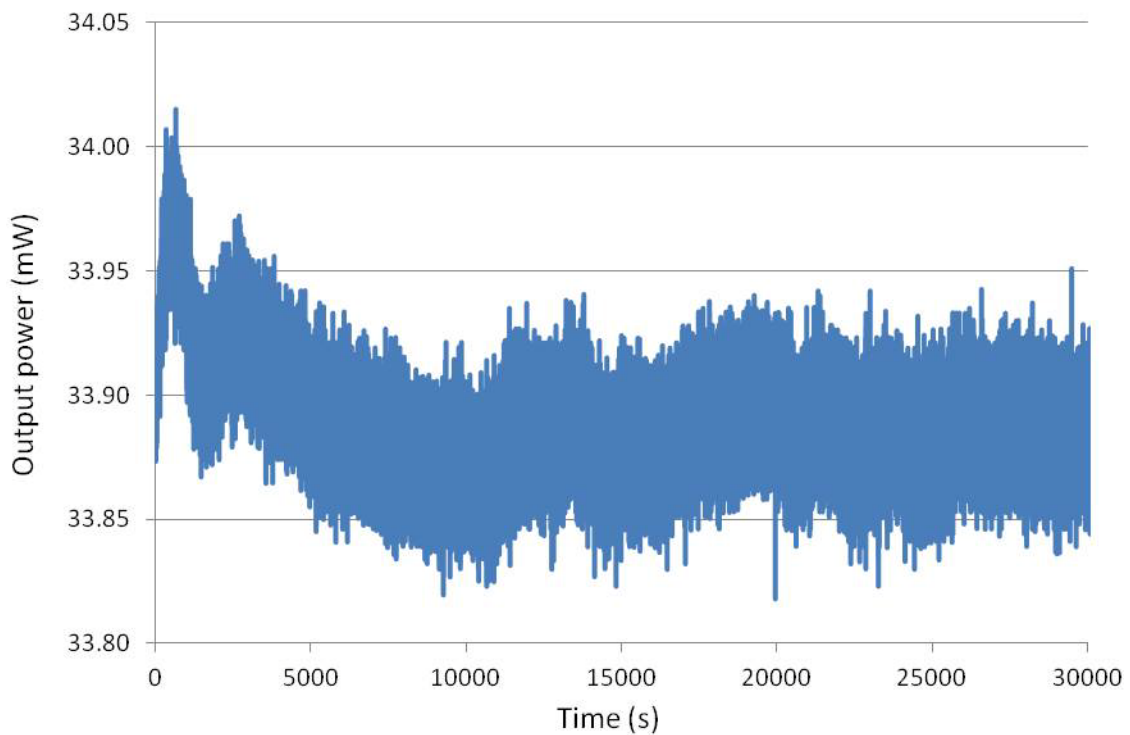


Fig. 6.6. Power stability of the output beam of AOM.

4. Fiber coupler assembly (FCA) and fibers

There are two choices for the FCA in the lab: FCA from New Focus, Inc and FCA from OZ Optics LTD (Fig. 6.7). The New Focus FCA has much larger dimension than the OZ Optics. Based on the experimental experience, both of them take at least half a day for the alignment work. For FCA of New Focus, the whole process is to aim the laser beam and refine the coupling work. As long as the fiber is unplugged, the coupling work needs to be started from the beginning. However, although it also takes a long time to finish the alignment, the most time consuming part of coupling the FCA from OZ Optics is to aim the laser beam into a fiber and once faint light power appears on the power meter, the fine work to achieve the highest coupling efficiency can be done within a few minutes. Furthermore if the fiber is unplugged from the FCA, the coupling work needn't be started from the beginning. What's more, the FCA of OZ Optics is more stable than the FCA of New Focus. In addition, the FCA from OZ Optics is a customized product that has a half wave plate inside which shrinks the space a lot. Therefore, FCA of OZ Optics is utilized in LD system.

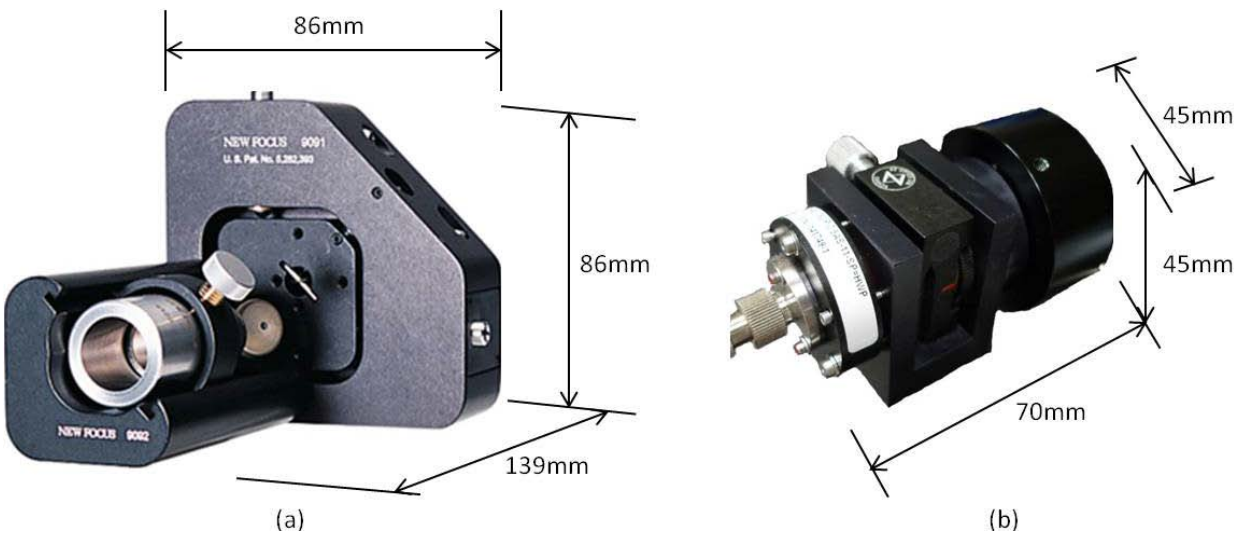


Fig. 6.7. FCA: product from (a) New Focus, and (b) OZOptics.

For optical fibers, there are three choices in the lab: polarized maintaining (PM) fiber from Thorlabs, Inc (P5-780PM-FC-2), customized armored polarized maintaining (PM) fiber from Thorlabs, Inc (TS0633833-PM780-HP) and armored polarized maintaining (PM) fiber from OZ Optics LTD (PMJ-3AF3S-780-5/125-3AS-2.5-1-ER=25), shown in Fig. 6.8. All of them are panda style with PC/APC connectors. The side of a fiber with the APC connector is connected to the FCA.

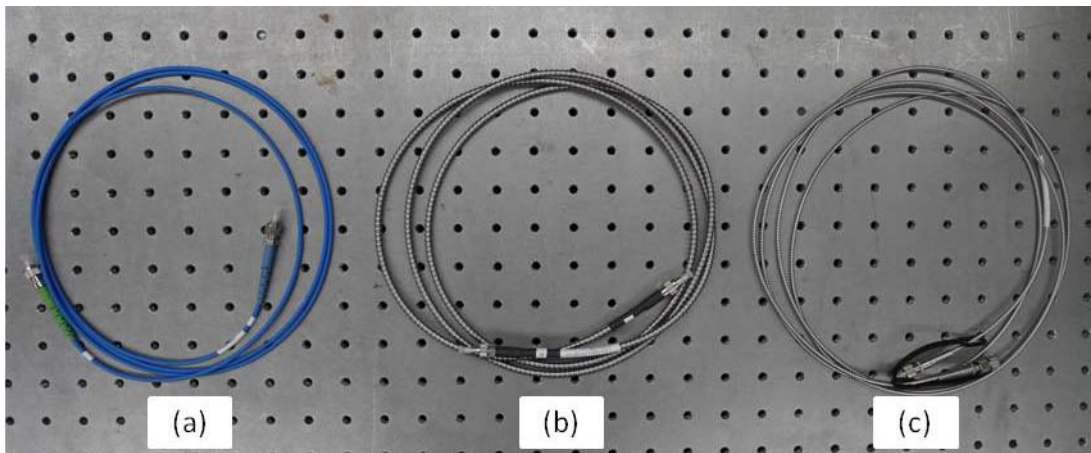


Fig. 6.8. (a) Panda style polarized maintaining (PM) fiber from Thorlabs, (b) panda style armored polarized maintaining (PM) fiber from Thorlabs, and (c) style armored polarized maintaining (PM) fiber from OZ Optics.

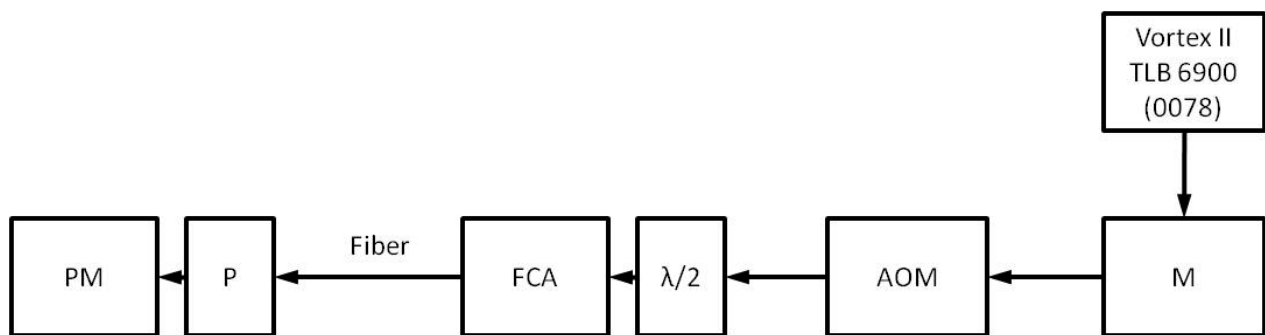


Fig. 6.9. Configuration of the test that the fiber is not touched by anything.

Two kinds of tests were performed for comparison. First, we used a power meter to test the intensity of the laser beam coming out of a stable fiber. This test shows the PM capabilities of this fiber. The test configuration is shown in Fig. 6.9. A polarizer was put in front of the power meter. It is critical to start recording at the extinction ratio. Thus, it is better to record at 30% of the maximum intensity by rotating the polarizer. The time window was one hour and the sample was recorded every second. Two samples of each type of fiber were tested and two types of FCA were utilized. Results are shown in Table 6.3.

Table 6.3. Results of the test with a stable configuration.

	FCA (OZ Optics)			FCA (New Focus)		
	Max power (mW)	Min power (mW)	Percent	Max power (mW)	Min power (mW)	Percent
PM fiber (Thorlabs) A	3.554	2.897	18.5026	6.351	4.743	25.3157
PM fiber (Thorlabs) B	3.767	3.077	18.3249	4.830	4.586	<u>5.0399</u>
Armored PM fiber (Thorlabs) A	3.439	2.770	19.4598	5.936	4.233	28.6992
Armored PM fiber (Thorlabs) B	3.306	2.974	10.0514	7.617	4.078	46.4558
Armored PM fiber (OZ Optics) A	4.385	4.055	<u>7.5237</u>	2.508	2.300	<u>8.3054</u>
Armored PM fiber (OZ Optics) B	3.868	3.753	<u>2.9631</u>	4.249	2.038	52.0463

The percent (Table 6.3) is the variation between the maximum power and minimum power recorded during the period with respect to the maximum power. It is clear to see that the variation percent below 10% happened on the PM fiber from Thorlabs and the armored PM fiber from OZ Optics, and the armored PM fiber from OZ Optics had more chance than the PM fiber from Thorlabs.

The second test is to find out which fiber has the best resistant ability when adding force to or shaking the fiber. The configuration is shown in Fig. 6.10. A 20 seconds video was captured by a camera for each type of fiber being touched all the time. When applying a force on the PM fiber from Thorlabs and the armored PM fiber from Thorlabs, there was a significant variation of the intensity of laser beam, while there was a much less variation of the armored PM fiber from OZ Optics.

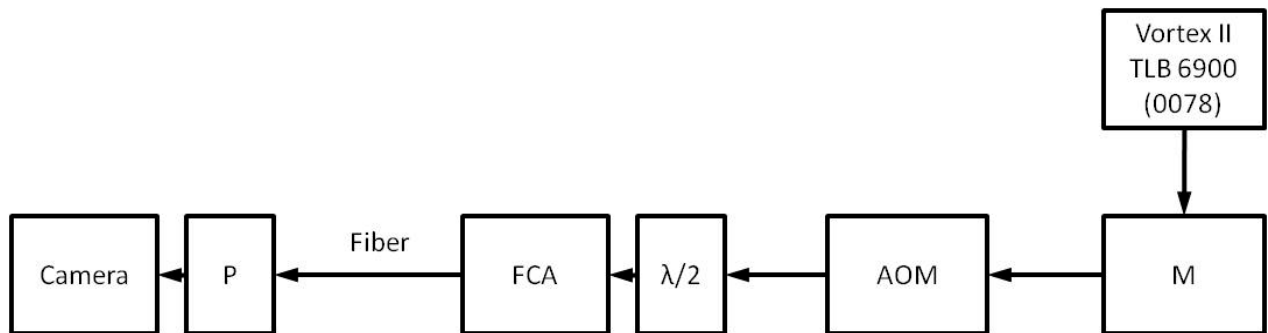


Fig. 6.10. Configuration of the test that the fiber is touched during the whole test period.

Based on results of these two tests, the armored PM fiber from OZ Optics is the best choice for LD system.

5. Optical switch (OS)

The OS has the function that can switch between the two lasers measuring for the shape measurements. The OS implemented in the LD system is the pro800 series from Thorlabs, Inc. Figure 6.11 shows the power stability of the laser beam coming out of the OS after switching from Vortex II-TLB 6900 (0055) to Vortex II-TLB 6900 (0078). The time window was 3600 seconds and sample was taken by the photodiode power meter every second. Vortex II-TLB 6900 (0055) was utilized in the first 10 seconds and after that the laser was switched to Vortex II-TLB 6900 (0078). Results show that the variation is between 4.95 mW and 5.00 mW and the OS can keep the stability of laser beam.

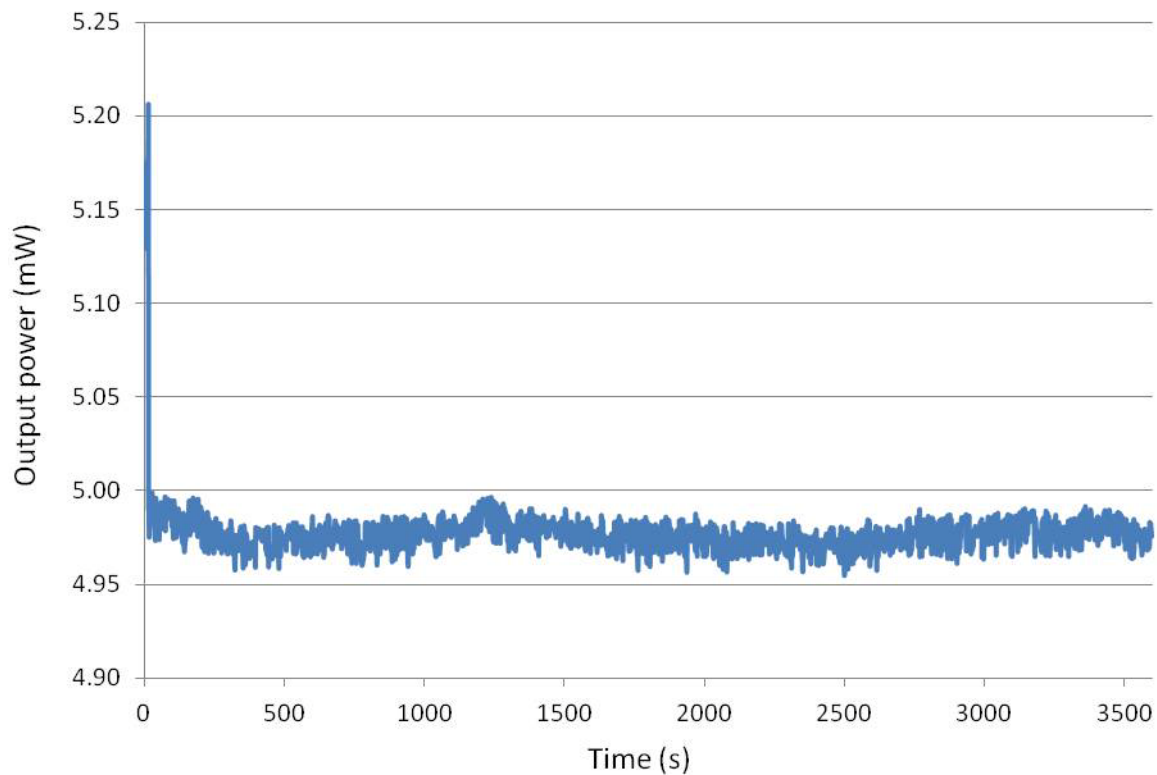


Fig. 6.11. Power stability of the laser beam coming out of the OS.

6. Breadboard

All the optical components of LD system except the OS are designed to mount on a breadboard. This customized breadboard is made from aluminum by VERE, Inc with anti-reflective black coating with the dimension of 18"×18" ×2.3" and 14 lbs of weight. Four holes are on the bottom of the board and four sorbothane bumpers from Thorlabs, Inc (AV1) are mounted to support the whole setup.

6.1.1.2 Optimized 1st version laser delivery system

Once all the components in the LD system are selected, the system needs to be optimized until it has the highest laser beam transportation efficiency. Figure 6.12 shows the beam intensity after each component. The output beam intensity from the OS is around 10mW for both of the two Vortex lasers, which is powerful enough for the measurement of TM.

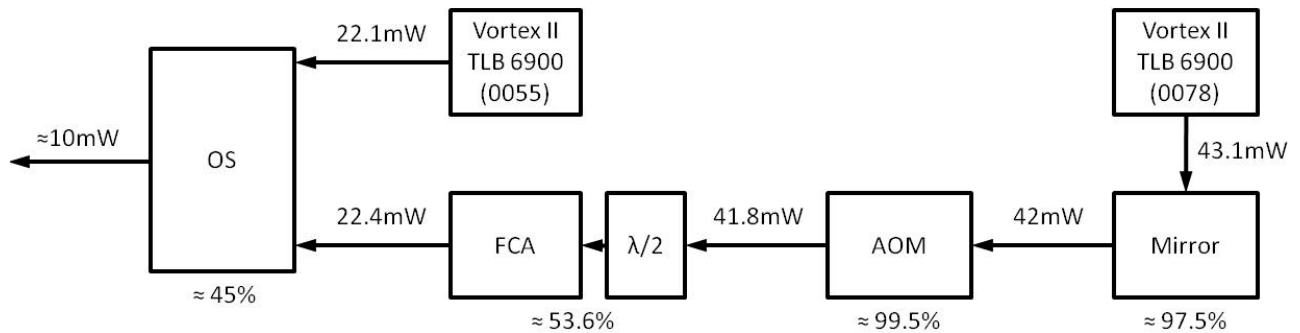


Fig. 6.12. The laser beam transportation efficiency map of LD system.

Compacting and packaging the LD system is another critical step. Figure 6.13 shows the CAD model of a compact and packaged LD system. The main parts are limited to a small breadboard

(12"×10" ×0.5"), which is connected with the extra light customized breadboard mentioned in the last section.

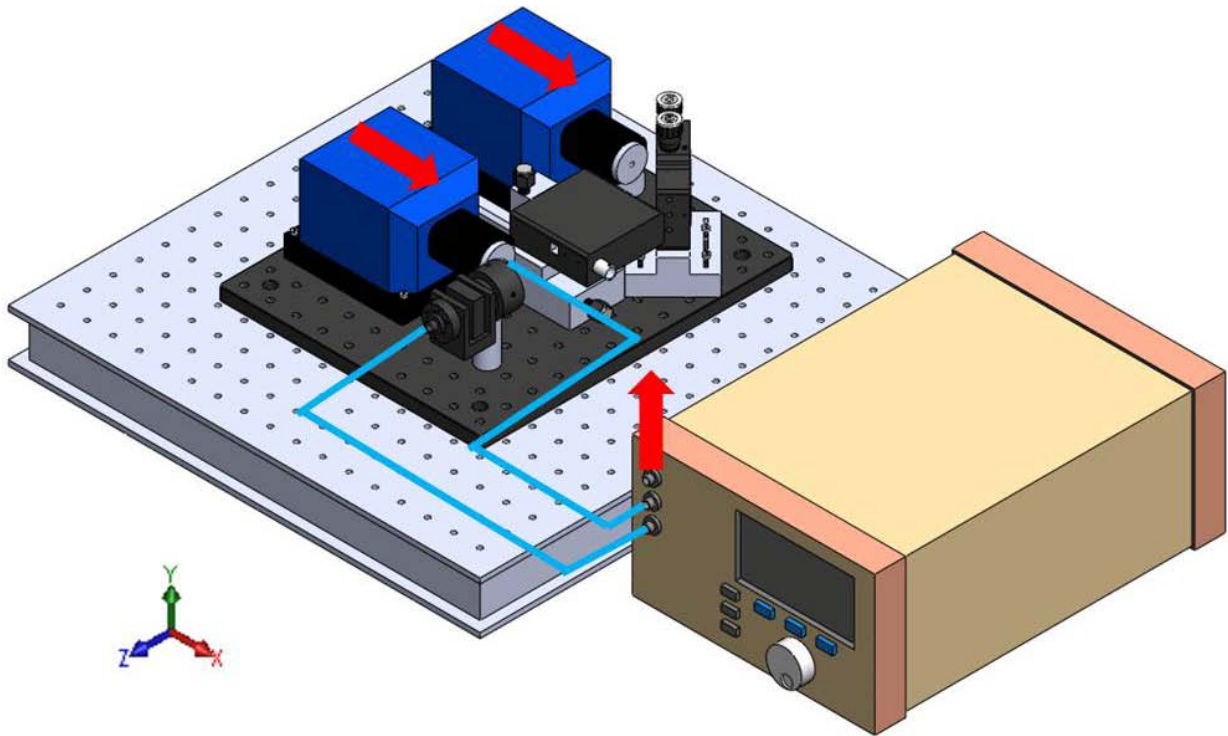


Fig. 6.13. 3D CAD model of the LD system package.

6.1.2 2nd version

The second version of LD system includes a wide range tunable near-infrared laser (Velocity TLB 6312), an anamorphic prism pair (APP) that is used to transform elliptical laser beams into nearly circular beams, an acousto-optic modulator (AOM), a half-wave plate ($\lambda/2$) which can change the polarization direction of the laser beam, and a fiber coupler assembly (FCA), shown in Fig. 6.14. The output beam power of the velocity laser is 8.7 mW and the output beam power of the LD system is 4.5 mW.

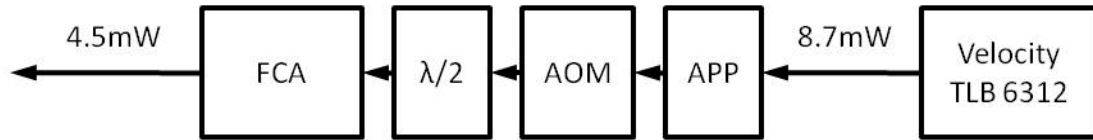


Fig. 6.14. Power distribution in 2nd version of LD system.

All of the optical components in this version are introduced in previous section except APP. The laser beam coming out of the Velocity laser is elliptical. In order to obtain a nearly circular and Gaussian beam, the APP is used. Different rotations of the APP were tested. Figure 6.15 shows cross-section of the output laser beam. When the APP is rotated by 90° and 270°, the beam is nearly circular and has much stronger intensity.

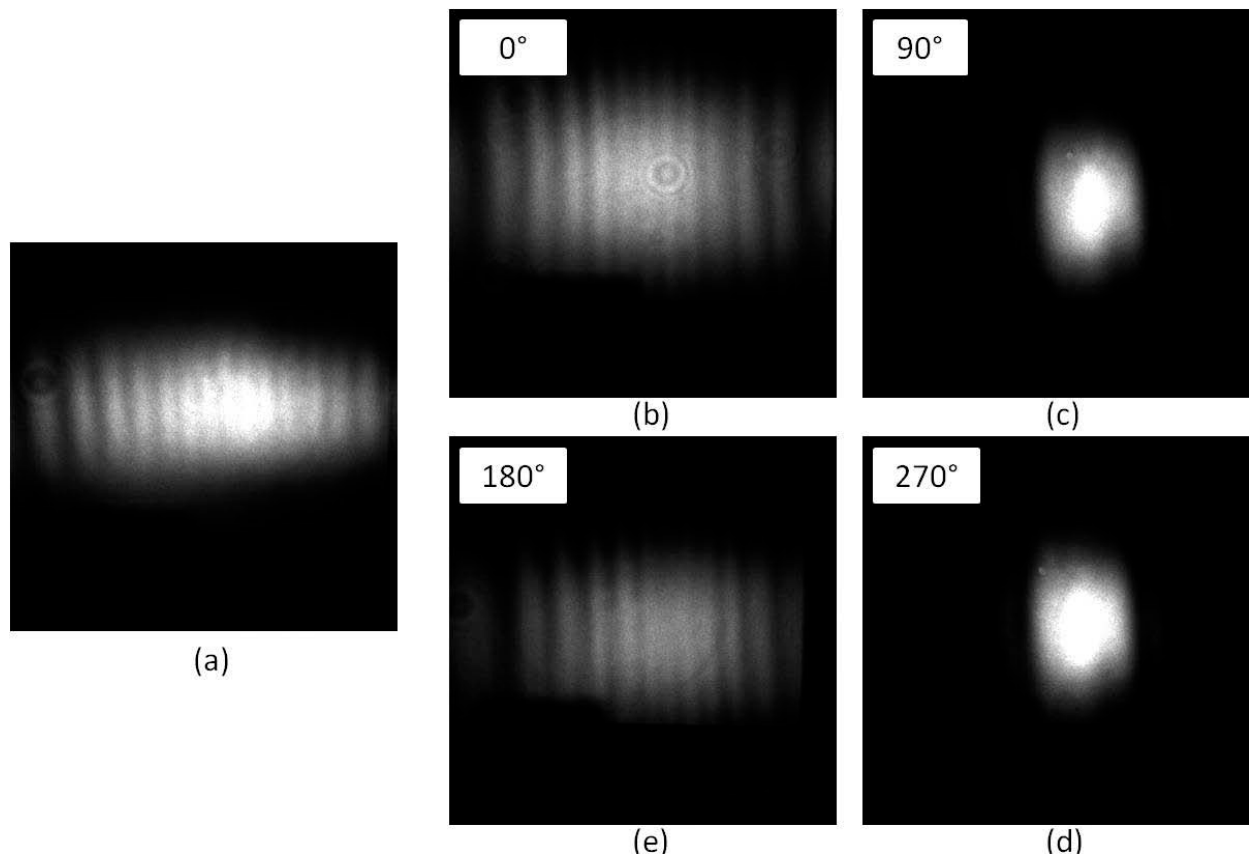


Fig. 6.15 Cross-section of laser beam coming out of Velocity: (a) without APP, (b) to (d) with APP and the rotation degree of APP is from 0° to 270°.

6.1.3 Comparison of laser delivery systems

Two types of the LD system are presented in previous sections: type 1 switches from one laser (λ_1) to the other laser (λ_2) to generate shape contours; type 2 is to switch from λ_1 to λ_2 by switch the settings within only one tunable laser to generate shape contours. In type 2, we could use the Velocity laser and also the Vortex lasers. One limitation of the Vortex lasers is that the possible synthetic wavelength is not appropriate for the measurement of TMs. For the comparison of different LD systems, a metal cone (5 mm height, 12 mm diameter) is used as the test sample and shape measurements are performed.

Figure 6.16 shows the image quality of modulation, optical phase and unwrapped phase (with mask) of different LD systems: (a) 1st version of LD system (779.80 nm, 780.24 nm), (b) only Vertex 0078 used in 1st version of LD system (779.59 nm, 779.86 nm), and (c) 2nd version of LD system (779.8 nm, 780.2 nm). Image contrast is calculated and shown in upper left side of each modulation images. Results show that the image obtained from 2nd version of LD system has the best image quality, but there is not much difference among those images.

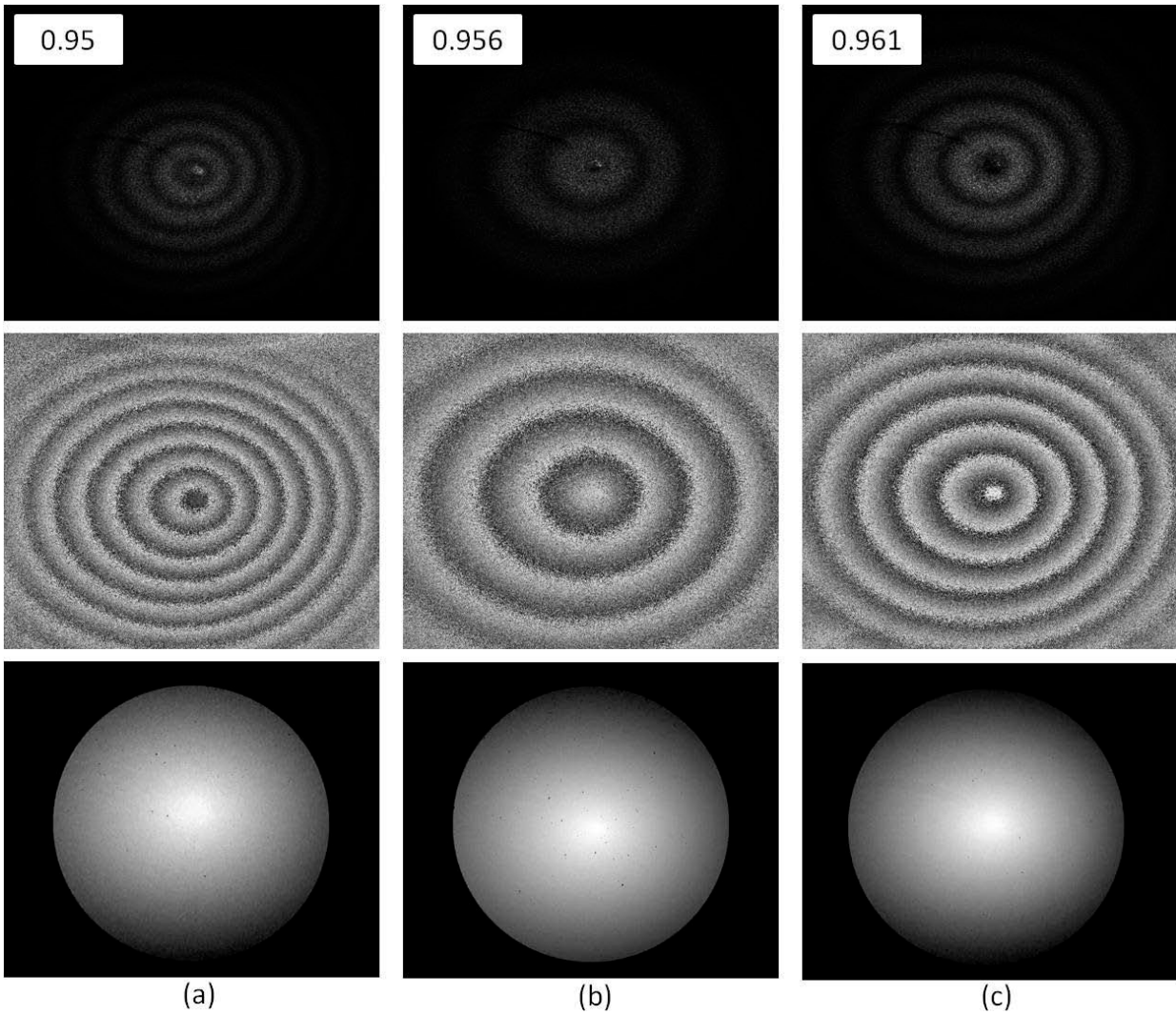


Fig. 6.16. Image quality of modulation, optical phase and unwrapped phase (with mask) of each LD system: (a) 1st version of LD system, (b) only Vertex 0078 used in 1st version of LD system, and (c) 2nd version of LD system. Image contrast is shown in upper left side.

6.2 Optical head system

The OH system is a Michelson configuration setup and has two generations: polarizing cage system and non-polarizing system. The main difference is that polarizing cage system utilizes a polarizing beamsplitter cube (PBS) to separate the reference beam and the object beam, and therefore the system is very sensitive to the polarization direction of the laser beam. In contrast,

non-polarizing system utilizes a non-polarizing beamsplitter cube (BS) so that it is much easier to assemble and operate the OH system.

6.2.1 1st generation

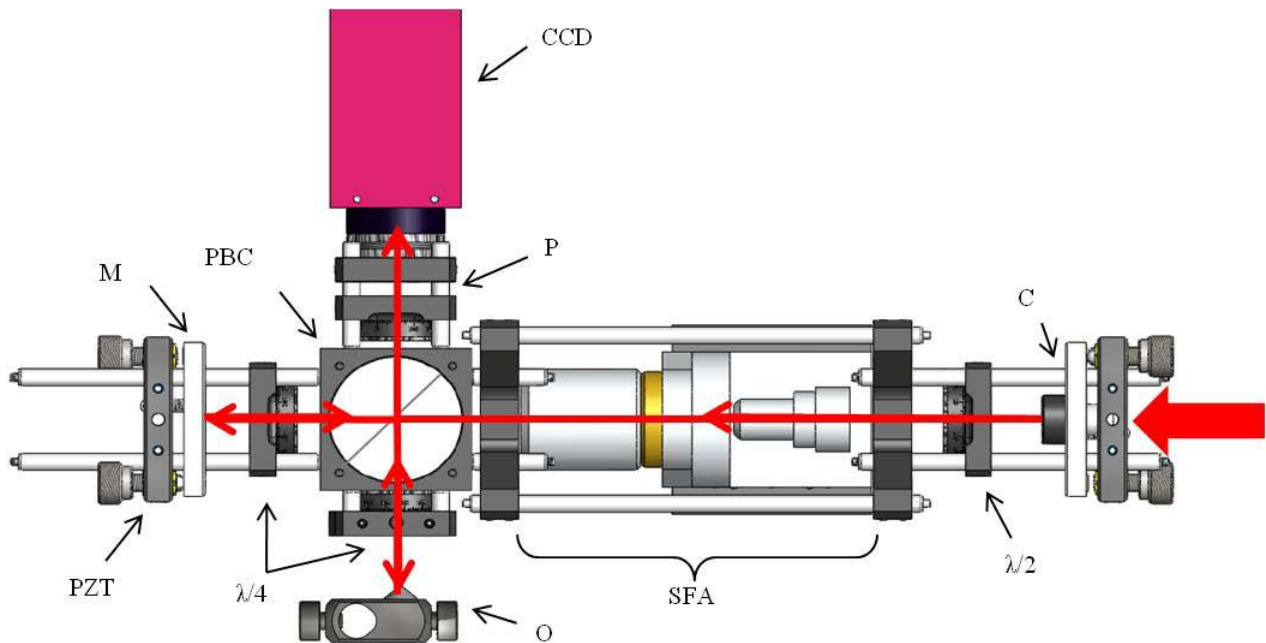


Fig. 6.17. CAD model of the polarizing cage style OH system marked with laser beam path.

The 1st generation of OH system is a polarizing cage system (Fig. 6.17). The laser beam coming out of the OS firstly goes through a collimator (C), a wave plate ($\lambda/2$) and then a spatial filter assembly (SFA). The function of the SFA is to filter high spatial frequencies of the beam and get a clean Gaussian beam profile. After the SFA, the light is directed through a polarizing beamsplitter cube (PBS), which splits the light into reference beam and object beam. The reference beam passes through a quarter wave plate ($\lambda/4$) and is directed to a mirror (M)

connected with a piezoelectric transducer (PZT) that is controlled by the CP and used for application of phase-shifting algorithms. The object beam is directed through a quarter wave plate ($\lambda/4$) onto the object. The reflected object and reference beams are directed through the PBS again and combined at the surface of the CCD camera (CCD). Then the spatial intensity distributions recorded by the CCD will be processed by the computer.

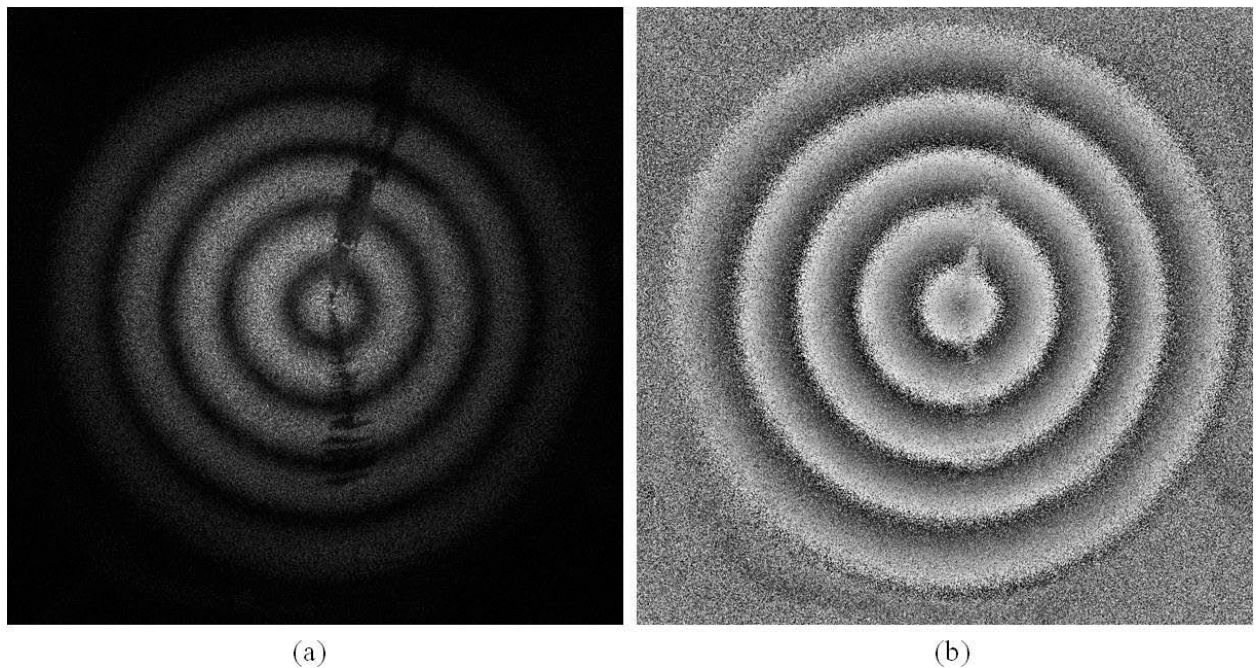


Fig. 6.18. Interference fringes appear on a coated conical metal object in shape measurements. Laser wavelength of Votex 0055 is 780.13 nm and laser wavelength of Votex 0078 is 779.72 nm. Scratches are made for focusing purposes.

The polarizing cage OH system has the advantages that the obtained images have high contrast and high qualification (Fig. 6.18). However, there are two main limitations found during experiments: the light intensity coming out of OH system varies all the time which results from the unstable polarization direction of the laser beam and the beam ratio which equals intensity of

reference beam divided by intensity of object beam also changes. In addition, reflection issue exists some time so that the image in the viewer is unclear, these reflections will influence the quality of fringes (Fig. 6.19).

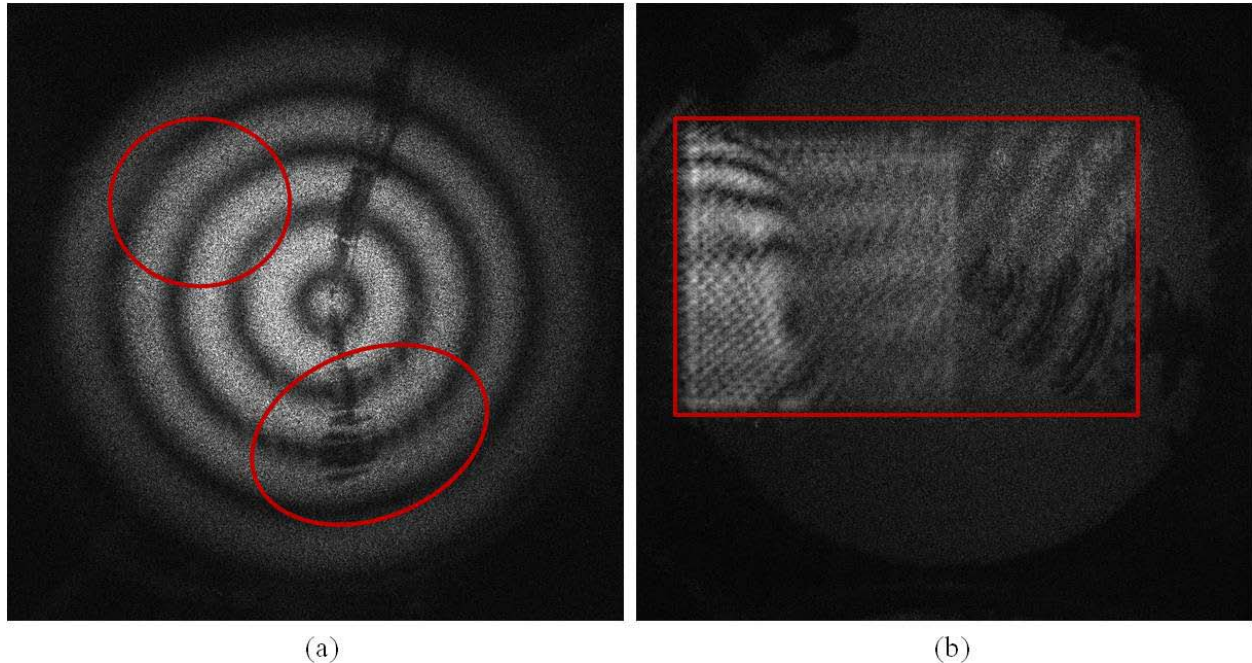


Fig. 6.19. Reflection issue on images of two coated conical metal objects in two situations: (a) shape measurement situation, and (b) no fringes situation. Scratches are made for focusing purposes.

6.2.2 2nd generation

The idea of the 2nd generation of OH system is to increase the stability and reduce reflection issues. Therefore, we employ a non-polarizing BS, and take off the cage so that we can rotate some of the optics and eliminate the reflection. Due to the non-polarized property of the system, some optics can be taken off and the OH system is simplified greatly. The final configuration of setup is shown in Fig. 6.20. The light coming through the collimator (C, F810FC780) can be

enlarged into a parallel beam with 7.1 mm diameter. Then it directly hits on the non-polarizing BS (CM1-BS014) that is in 700-1100 nm broadband and splits light into reference beam and object beam. In the reference light path, a neutral density filter (NDF, NE20B) and a polarizer (P, LPVIS050) are embedded. Both the NDF and polarizer can control of beam ratio, which has a best range between 2 and 5 and depends on the reflectivity of the tested sample. NDF is for coarse adjustment and the polarizer is for fine adjustment. There is no optics in the object light path. Both of the reflected reference light and object light are combined at the non-polarizing BS and reached at the CCD sensor. In this case, by using non-polarizing BS, the beam ratio is stable.

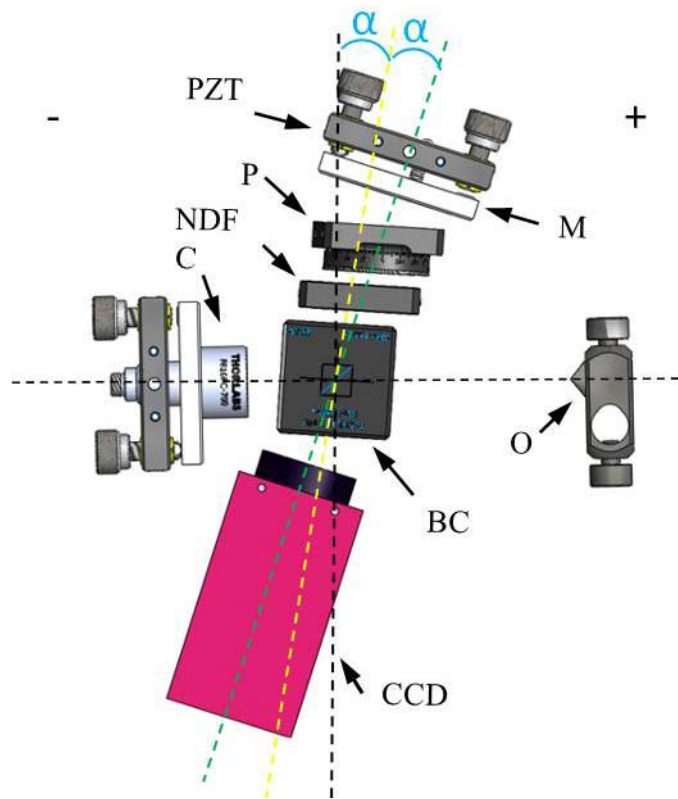


Fig. 6.20. CAD model of the non-polarizing OH system.

In regard of the reflection, the BS is the main issue. Therefore, experiments were performed in order to find out a combination of OH system with the best image quality and no reflection by rotating the BS and other related parts. Figure 6.20 shows two perpendicular axes in black in which all parts locate originally. Then the BS is rotated to the marked yellow axis by α degree. And the mirror and CCD camera are rotated 2α degree to the marked green axis. In Fig. 6.21., α is from “-18” to “+18” in 2 degree step.

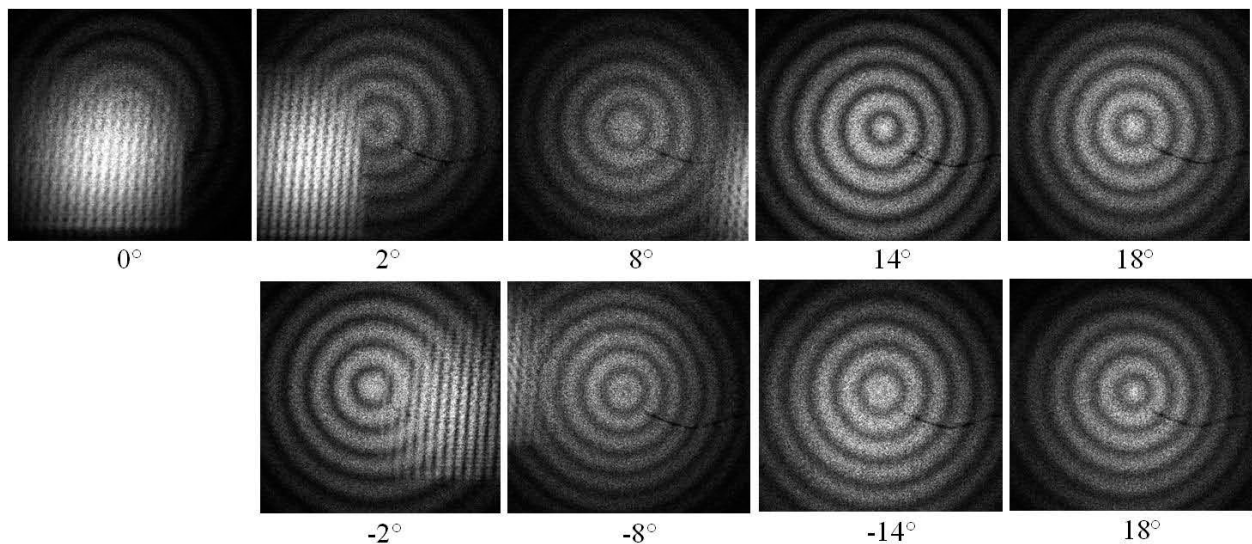


Fig. 6.21. Comparison of image quality of different rotation degrees.

Selected images with interference fringes generated on a conical metal object for shape measurements are shown in Fig. 6.21. The wavelength of Vortex 0055 was 780.16 nm and the wavelength of Vortex 0078 was 779.74 nm. Scratches on the object are made for focus purpose. From 0 degree to 18 degree and from 0 degree to -18 degree, results have experienced from blurry

images with reflection to good quality images, and finally back to blurry images. The best images occurred at 14 degree.

In order to verify that components of OH system are in correct positions, a ray tracing test was performed in Tracepro software, with 14-degree rotation of BS (Fig. 6.22). The NDF and polarizer are not included. The surface source from the surface of collimator emits 500 rays of totally 1 watts flux within a 7.1 mm diameter area. The material property and surface property of relative components in OH system are shown in Table 6.4.

Table 6.4. The material property and surface property of relative components.

Material property	Surface property		
Non-polarizing BS	Non-polarizing BS	Mirror	Object
SCHOTT BK7	3 Layer AR	Perfect mirror	Flat white paint

In the light intensity ray tracing demonstration, every component is in the correct position of optical path basically, but small offset still exists. This is due to the refractive index of BS is larger than 1 so that the light coming out of BS in each direction shifts a little bit. Therefore, this should be considered in the prototype design section.

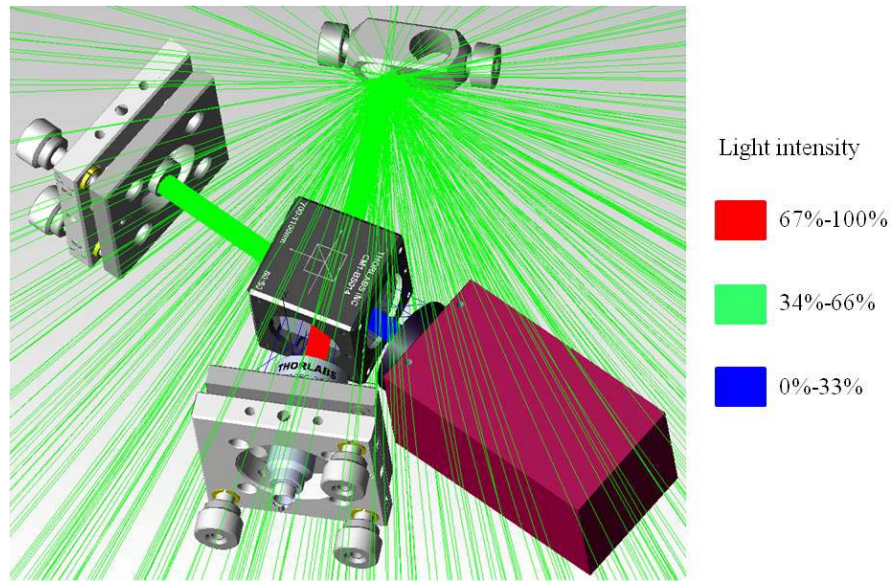


Fig. 6.22. Ray tracing result of OH system with BS rotated in 14 degree.

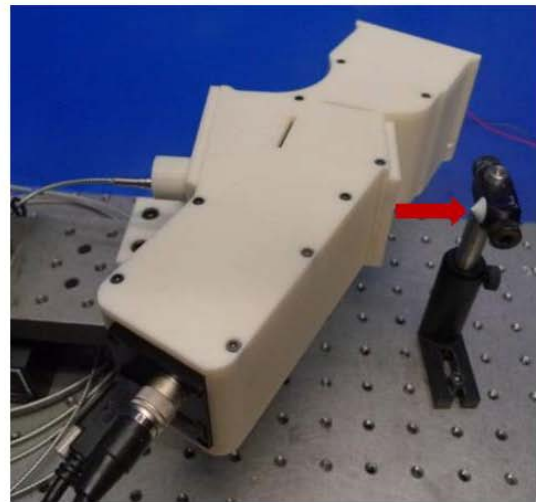
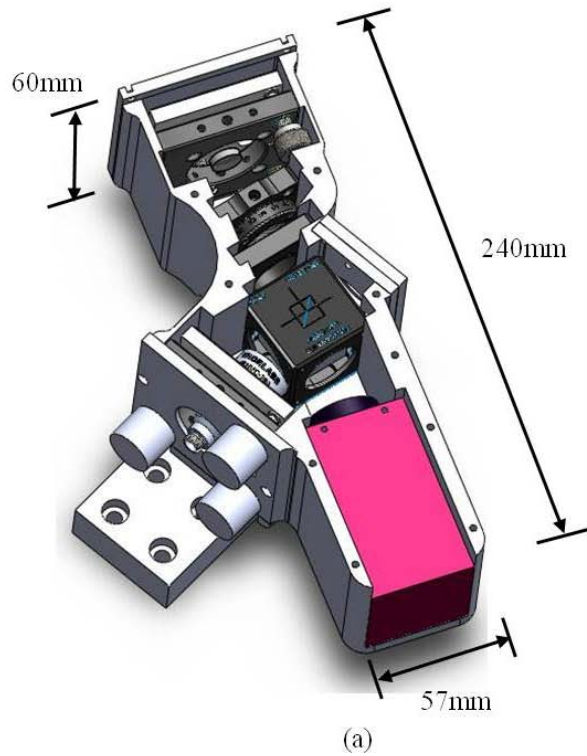


Fig. 6.23. First generation of (a) 3D CAD model design and (b) prototype of OH system.

The first generation packaging system was designed based on the experimental experience and optical ray tracing result and manufactured in ABS plastic by 3D printer (Fig. 6.23). The dimension of the OH enclosure is about 240 mm (L) ×57 mm (W) ×60 mm (H). A 1-inch thick square base in bottom was designed to connect between the OH package and a holder.

6.2.3 Cameras

Cameras can influence the optical image quality. In order to identify an appropriate camera for the OH system, three different cameras are tested and their basic specifications are listed in Table 6.5.

Table 6.5. Basic specifications of cameras that were considered.

	Pike F145	Pike F505	Pixelink PL-A741-E
Picture size (pixel)	1388×1038	2456×2058	1028×1024
Pixel Size (μm)	6.45×6.45	3.45×3.45	6.7×6.7
Spectral sensitivity	Green	Green	Near infrared

Shape measurements are performed and the convex side of a copper foil in spherical shape is imaged. Images are shown in Fig. 6.24, which are captured by (a) Pike F145, (b) Pike F505 and (c) Pixelink PL-A741-E. Based on the image quality and calculated contrast, Pixelink is the best camera for OH system.

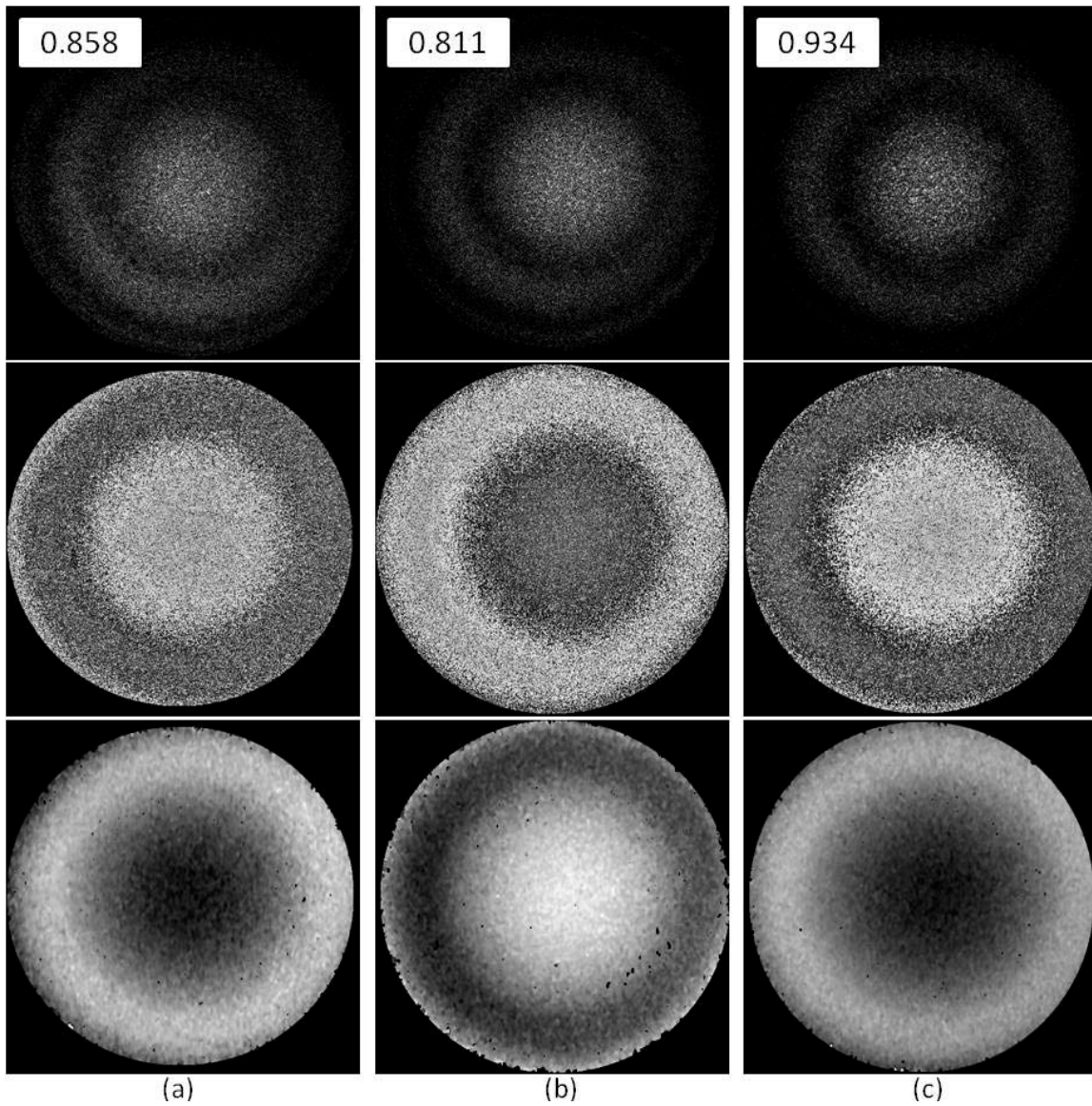


Fig. 6.24. Images captured by different cameras: (a) Pike F145, (b) Pike F505, and (c) Pixelink PL-A741-E. From top to bottom, images are modulation, optical phase and unwrapped phase. Image contrast is shown in the upper left side.

7 Sample preparation

When using laser imaging, it is essential that the surface object is reflective enough to produce a good clean image. When a laser, or any light source is shined on an object, a percentage of the emitted photons are transmitted through the object, another percentage are absorbed by the object, and the remaining photons are reflected at an angle equal to the contact angle. The amount of light that falls into these three categories is dependent on the material's mechanical and optical properties. For example, a very dark object will absorb the majority of the light shined on it, while a bright object will not. Similarly, a translucent object will allow much more light to pass through it than an opaque one. The material that this project focuses on is the TM, which is translucent and therefore not very reflective. In order to increase the quality of the holographic image, the membrane should be coated in our case.

7.1 Coating materials

The most practical way of doing this would be to coat the membrane with a thin reflective film. While there are many such chemical compounds that would aid in this matter, most are unsuitable since there are many concerns and limitations regarding what is permissible to use on the human TM (Goldish and Kunyz, 2010).

Firstly, the coating must not be toxic, or cause any inflammation or irritation to the skin. Second, there must be a safe method to apply and remove the coating. For example, if the coating must be scraped or peeled off, or needs extreme heat or pressure to apply, it is obviously unsafe. Beyond the health concerns, the coating thickness is another concern. If the coating is too thick or too rigid, it may affect how the membrane vibrates, thus leading to incorrect measurements.

Additionally the coating would need to be highly reflective specifically within the wavelength region of the laser that is used during the tests. Lastly, referring back to application concerns, the coating would need to be evenly distributed on the membrane, as any large scale unevenness could alter the vibration patterns (Goldish and Kunyz, 2010).

Based on literature research (Dirckx and Decraemer, 1997) and the experience from doctors at MEEI, Titanium dioxide (TiO_2) and Zinc oxide (ZnO) are considered to be compared on the optical property of reflectivity by the use of spectrometer and MLDHS. Three concentrations of each chemical are tested: 200 mg per 5 ml of water, 450 mg per 5 ml of water and 700 mg per 5 ml of water. The concentration nomination of each type is 200 mg, 450 mg and 700 mg. Based on observation, TiO_2 can be dissolved in water easily while ZnO is hard to dissolve and even it is separated evenly in water it will sink to bottom very soon. After the TiO_2 coating is exposed in air, the color of this coating will turn to milky white or even a little bit yellow, while the ZnO coating can preserve its white color very well. Other materials such as cosmetics (sun block and high beam lip balm) and diluted methylene blue were also tested by spectrometer, but due to much lower reflectivity they won't be discussed in this section.

7.2 Spectrometer

The direct way to test the reflectivity of a chemical is using a commercial product which can specifically measure the optical characteristics. The Ocean Optics spectrometer (USB2000+XR) is employed in the reflection measurements of different coatings. It contains a spectrometer that covers all wavelengths from ~200 nm to 1025 nm, an optical fiber with a coupler, a white light source lamp and a reflection probe that is a light illuminator and also a light receiver. Reflection

measured by this spectrometer is expressed as a percentage ($\%R_\lambda$) relative to the reflection from a standard reference substance

$$\%R_\lambda = \frac{S_\lambda - D_\lambda}{R_\lambda - D_\lambda} \times 100\%, \quad (7.1)$$

where S_λ is the sample intensity at wavelength λ , D_λ is the dark intensity at wavelength λ , R_λ is the reference intensity at wavelength λ .

Measurement procedures are as follows:

(1) Shake the container filled with solution until it has uniform suspension. All samples are coated on clear slides (Fig. 7.1). In order to keep uniform, the burette filled with the solution is positioned on a certain position and only one droplet is dripped onto the clear slide.

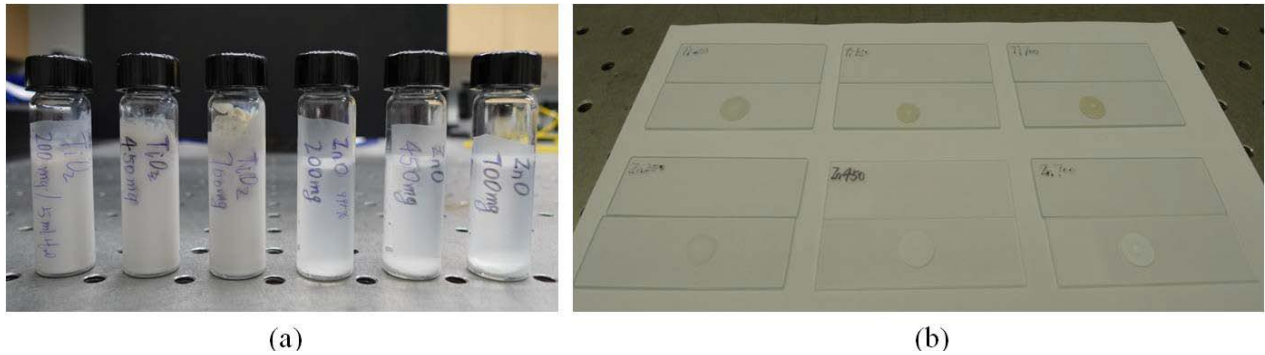


Fig. 7.1. (a) Chemicals diluted with water, and (b) different chemicals with different concentrations on clear slides.

(2) The light source is a Helium Neon tunable laser and all coating samples are tested under laser lights with four different wavelengths: green light (543 nm), yellow light (594 nm), orange light (604 nm) and red light (633 nm). This probe is only a light receiver at this time.

Experimental setup is shown in Fig. 7.2. Both of the laser light probe and reflectance probe are mounted together and face vertical to the sample.



Fig. 7.2. The spectroscopy setup.

(3) A white reference paper is measured that is assumed to reflect more light than the coating sample. After that, the six different coatings (TiO_2 200 mg, TiO_2 450 mg, TiO_2 700 mg, ZnO 200 mg, ZnO 450 mg, and ZnO 700 mg) are tested one by one.

(4) Change the light wavelength and repeat step 3.

Results are shown in Figs 7.3 to 7.6. No matter which laser light is utilized, the reflectance of TiO_2 coating is higher than ZnO coating at the different wavelengths. Roughly, higher concentration of each chemical type has higher reflectance. In the real experiments done by MLDHS, the TM will be exposed under near-infrared laser light so that it is preferable to consider the data obtained in red laser light experiment.

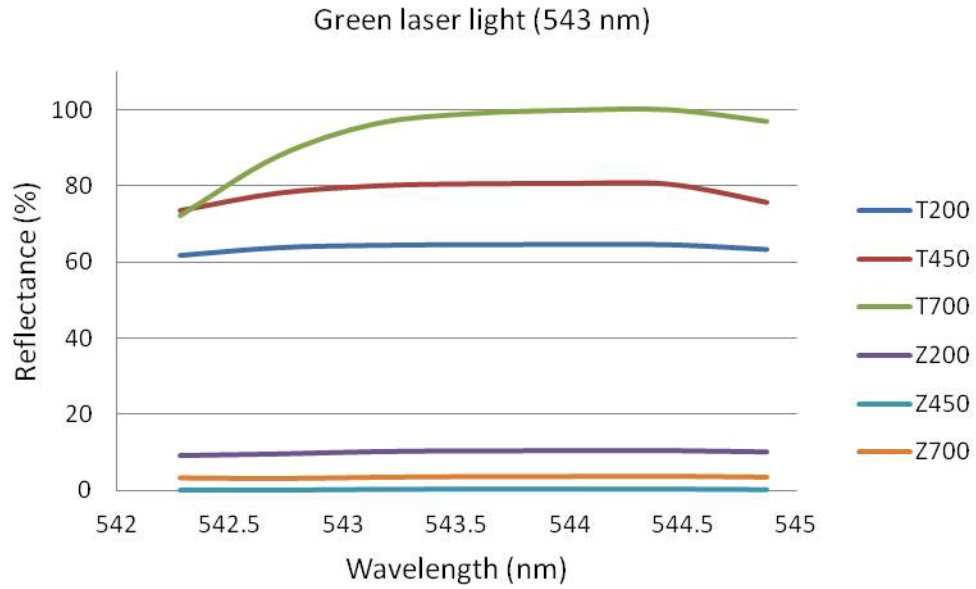


Fig. 7.3. Reflectance measurements of six coatings with green laser light.

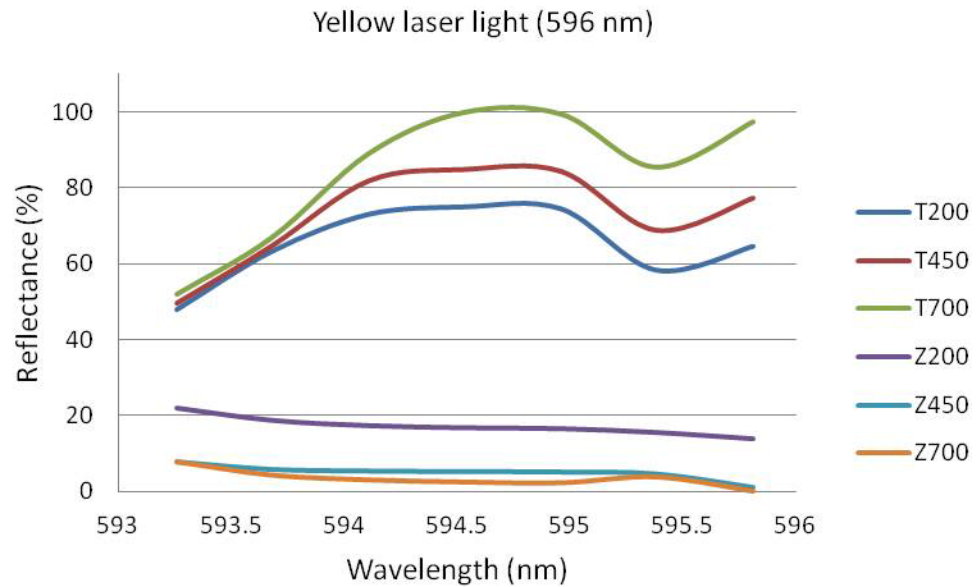


Fig. 7.4. Reflectance measurements of six coatings with yellow laser light.

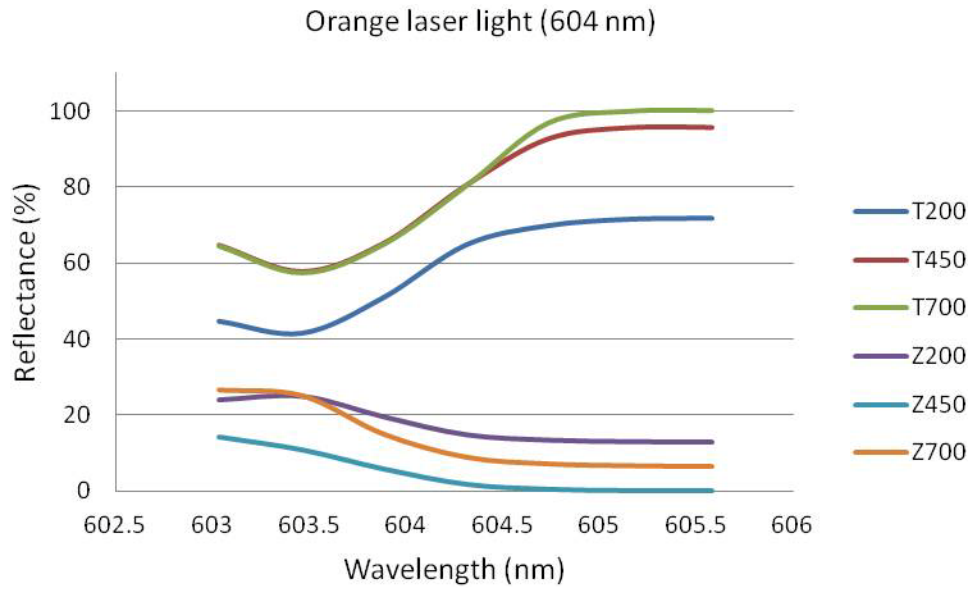


Fig. 7.5. Reflectance measurements of six coatings with orange laser light.

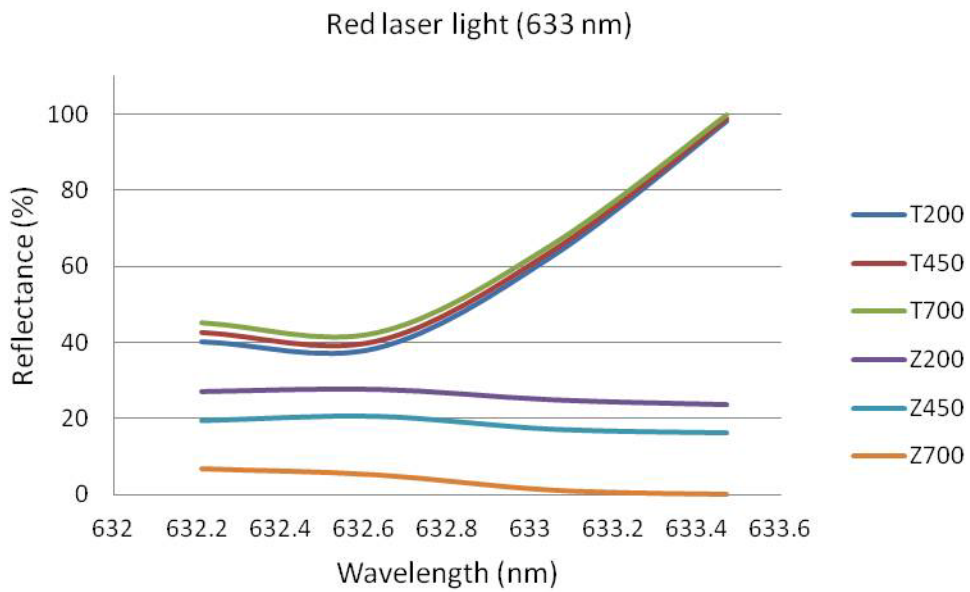


Fig. 7.6. Reflectance measurements of six coatings with red laser light.

7.3 Multi-wavelength lensless digital holography system

The coating will be applied on TM finally and thus it is better to investigate experiments on different coatings by MLDHS. Due to the essential characteristics of the TM that is translucent, hydrophobic and about 30 μm to 120 μm in thickness, the wax paper as a substitute is utilized instead of the real TM in the shape measurements by MLDHS. When viewing from lateral side, the TM is in concave shape and when viewing from medial side, the TM is in convex shape. Therefore both convex shaped sample and concave shaped samples are tested.

Measurement procedures are as follows:

- (1) Cut a piece of wax paper in circular area with 40 mm diameter. Cut along the solid line (Fig. 7.7 (b)) and overlap this edge with the dashed line by a piece of the double-sided tape. Then the sample is in conical shape. Stick the sample on a small disk that can be mounted on a post holder. Follow the same step for five more samples. The dimension of the sample is much larger than the one of human TM, because small wax paper sample coated with wet solution would warp a lot but not a relative large wax paper sample.
- (2) Shake the container filled with solution until we get uniform suspension. Dip a brush into the solution once and paint the coating on a certain area of the sample (Fig. 7.7 (b)). In order to keep uniform, follow the same step when applying other coatings on the samples. Wait until the sample gets dry.

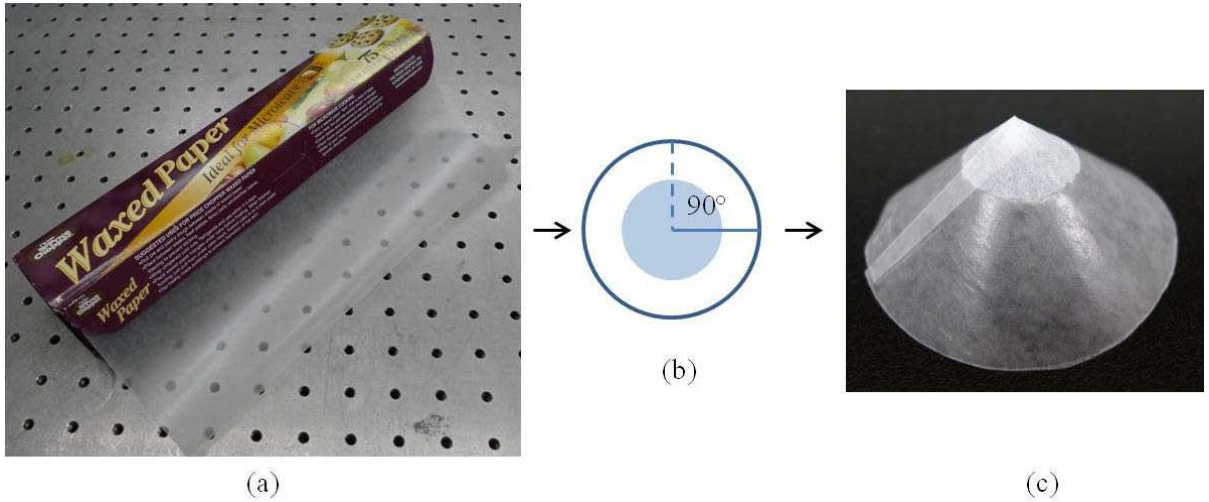


Fig. 7.7. (a) Wax paper, (b) the drawing for creating the conical shaped sample, and (c) the coated conical shaped sample.

(3) Shape measurements are performed to test the image contrast of each coated sample.

(4) Make a cross section of each image and calculate the image contrast.

Results are shown in Fig. 7.8 and Fig. 7.9. As the concentration of the coating increases, the image contrast also increases. But the change is during a very small amount. 700 mg for both TiO_2 and ZnO is very high concentration which is not so recommended and one can even see the particles clearly on the image of ZnO 700 mg.

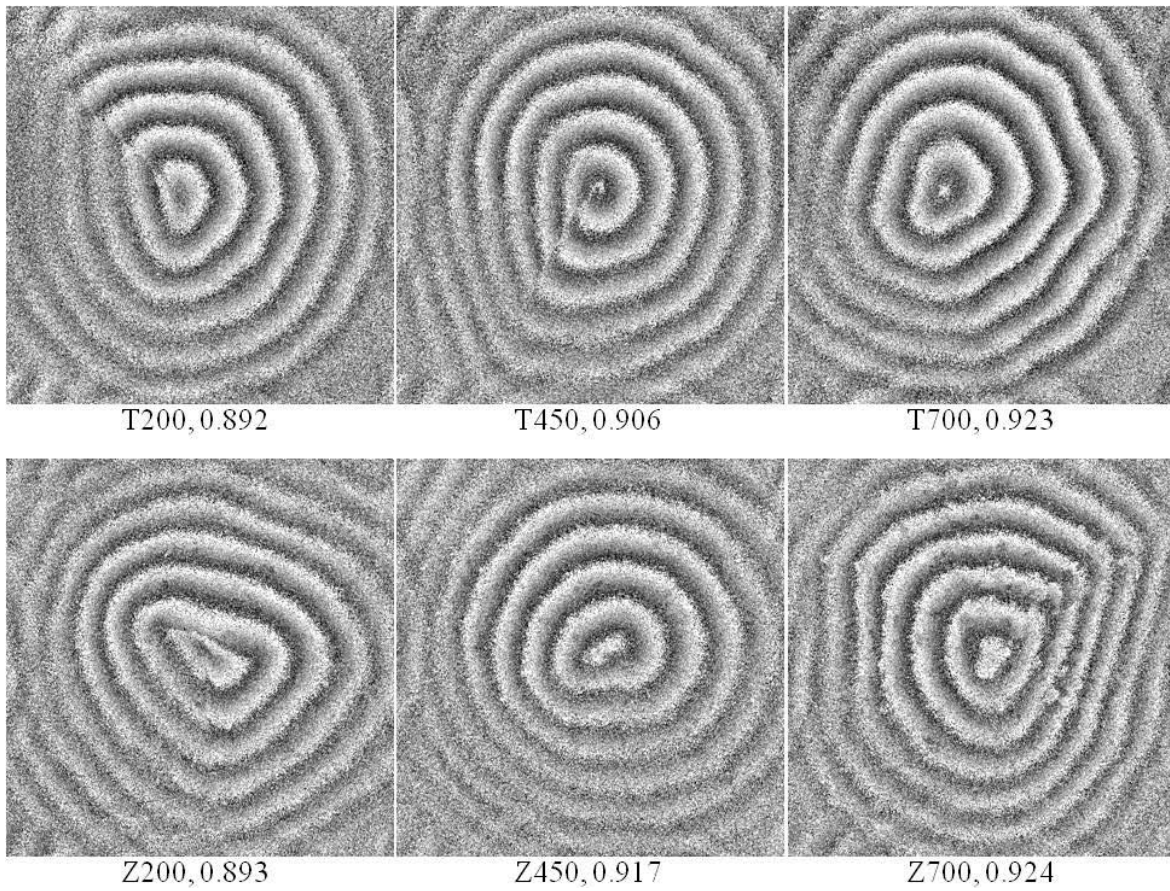


Fig. 7.8. Optical phase images of convex samples with different coatings. Image contrast is shown after every coating nomination.

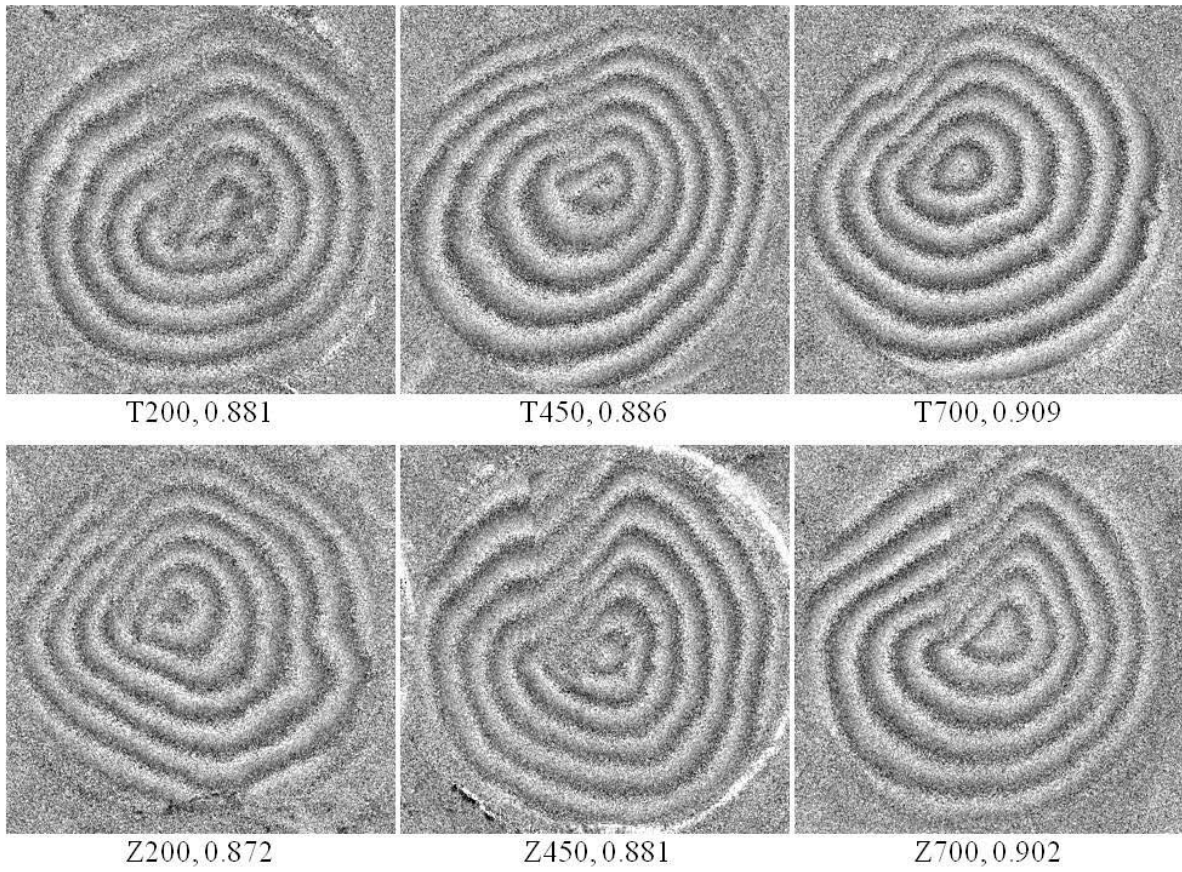


Fig. 7.9. Optical phase images of concave samples with different coatings. Image contrast is shown after every coating nomination.

8 Deformations and shape measurements

To characterize the performance and optimize the MLDHS, preliminary measurements are carried out on artificial samples and human TM samples. It is easy to control the shape and properties of an artificial sample so that results can be used for testing the system. After we get enough experience for the operation of the whole system, then we switch on the real human TM samples.

8.1 Measurements on artificial samples

The MLDHS is designed for measurements on human TMs, thus some parts of the system parameters are calibrated based on the geometry and properties of human TMs. The requirements for an artificial sample are: (a) the dimension should be similar to the a human TM or of an area of interest can be observed within the FOV of the system; (b) the geometry is known or can be measured; (c) mechanical properties of the artificial sample are known or at least the material is known; (d) the first natural frequency is within 100 kHz which is the max frequency that the function generator can achieve.

Four different kinds of samples are tested: quail eggs, small light bulbs, low density polyethylene (LDPE) samples and copper foil samples; all are coated with high reflected white paint, shown in Fig. 8.1. Quail eggs are hollowed and membranes inside are removed. Then they are mounted on plates using an alloy that has low melting point. The small light bulbs are also mounted by melted alloy. The LDPE samples that are in conical shape are fabricated by CNC machine from Proto Labs, with a 20 mm outer diameter, 10 mm outer height, 0.508 mm thickness; another cone has a 15.9 mm inner diameter, 8 mm outer height and 0.508 mm thickness. They

are mounted on a plate or a tube by glue. Copper foil samples are made by the following procedures: stick a piece of flat copper foil on a plate that has circular hole; press a stainless ball onto the foil above the hole and then the foil is cured. The spherical shape of the foil is considered as the same shape of the stainless ball. Experimental results that shape information can be measured of these four kinds of samples while deformation information can be measured on the copper foil samples only.

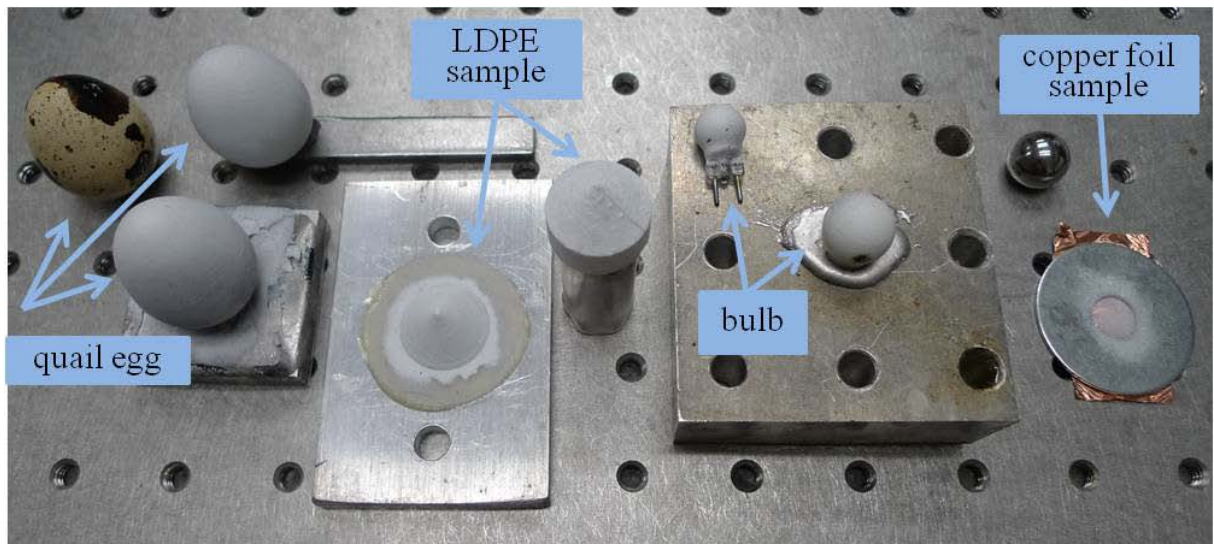


Fig. 8.1. Samples tested by MLDHS for shape and deformation measurements.

Another aspect that needs to be considered in experiment is the synthetic wavelength, that is, which combination of wavelengths from Vortex 0055 and Vortex 0078 gives the best image contrast. From Table 6.2, there are 7 wavelengths for each laser so that there are 42 different synthetic wavelengths.

Table 8.1. Synthetic wavelength according to the wavelength of Vortex 0055 and Vortex 0078.

Voltage (V)	40	50	60	70	80	90	100
Wavelength (0055) (nm)	780.09	780.13	780.16	780.20	780.24	780.27	780.31
Voltage (V)	40	50	60	70	80	90	100
Wavelength (0078) (nm)	779.70	779.72	779.74	779.77	779.80	779.84	779.86
Synthetic wavelength (mm)	1.56	1.48	1.45	1.41	1.38	1.42	1.35

An artificial object in a semi-spherical shape, which was made with copper foil, was tested in the convex surface side by MLDHS (Fig. 8.2). Procedures for manufacturing this semi-spherical-shaped object: stick a piece of flat copper foil by wax on a plate that has a hole in 6.375 mm diameter; punch a stainless ball with 12.69 mm diameter on the copper foil that covers on the hole; and then the copper foil deforms and assume that the shape of this deformed copper foil is the same as the shape of the stainless ball. Geometry and mechanical properties are shown in Table 8.2. The object was excited by a shaker and 3D deformations were recovered based on the proposed approach, see Eq. 5.14.

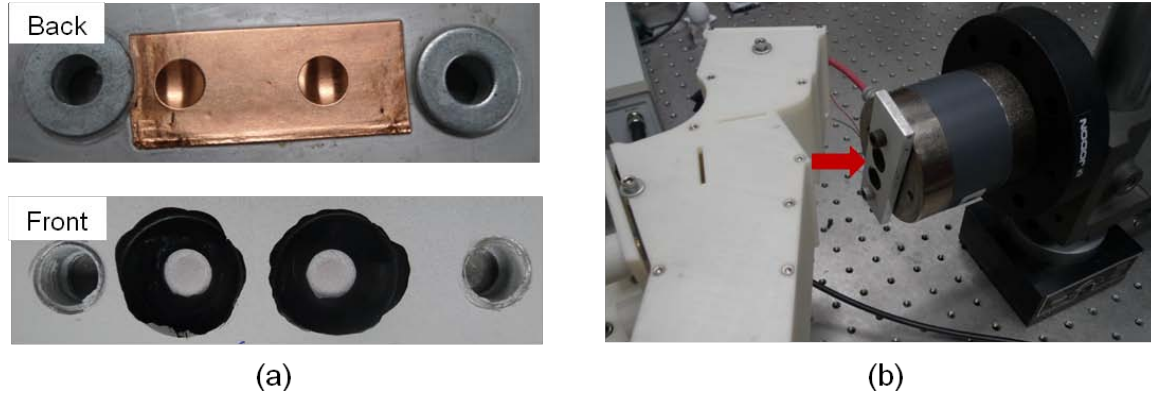


Fig. 8.2. (a) The artificial object with white paint on the convex surface, and (b) the experimental setup.

Table 8.2. Geometry and mechanical properties of the artificial object.

Geometry		Mechanical properties	
Spherical radius	6.35 mm	Young's modulus	115 GPa
Thickness	17.8 μm	Poisson's ratio	0.33
Central angle	60.31°	Mass density	8890 kg/m^3

Fringes were observed at 80.417 kHz. Representations of the artificial object's 3D deformations and shape are shown in Fig. 8.3. Results show that the range of predicted deformation in x direction is 24.17% of the range of measured deformation in z direction, and the range of predicted deformation in y direction is 24.64% of the range of measured deformation in z direction. Therefore, researching on the dynamic behavior of this non-flat object in x and y directions is significant.

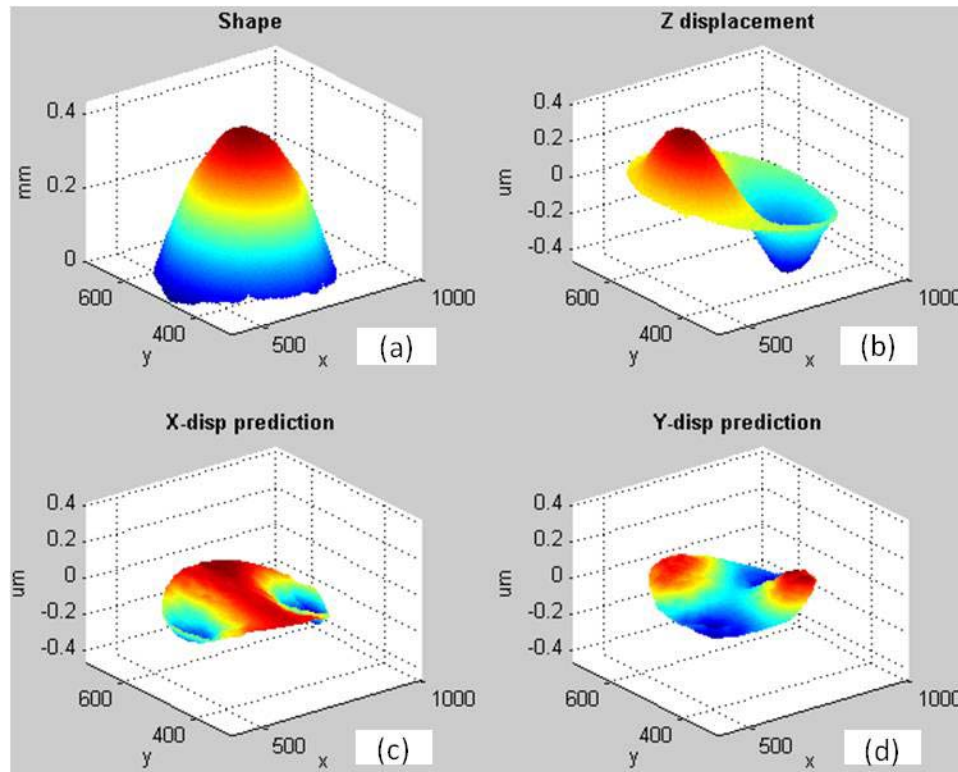


Fig. 8.3. Experimental results at 80.417 kHz: (a) representation of the artificial object shape, (b) displacement measured along optical axis (z axis), (c) predicted displacement in x direction, and (d) predicted displacement in y direction.

8.2 In-vitro measurements on chinchilla tympanic membrane

The sample was a fresh chinchilla temporal bone without history in this study. The temporal bone was removed within 24 hours post-mortem and stored in normal saline at 4 °C, as approved by the Institutional Review Board of the Massachusetts Eye and Ear infirmary. The cartilaginous ear canal was resected and the bony external ear canal was drilled away until 80-90% of the TM surface was visible. To increase the light reflectivity from the TM surface, the TM surface was painted with a suspension of 3% TiO₂ powder in saline. In order to keep moist, the sample was immersed in saline regularly during measurements.

In Fig. 8.4, the head bone was held in a clamp. The TM was placed close to an earphone and microphone coupler speculum integrated into the OH. The microphone was utilized to monitor the stimulus level at the edge of the TM surface.

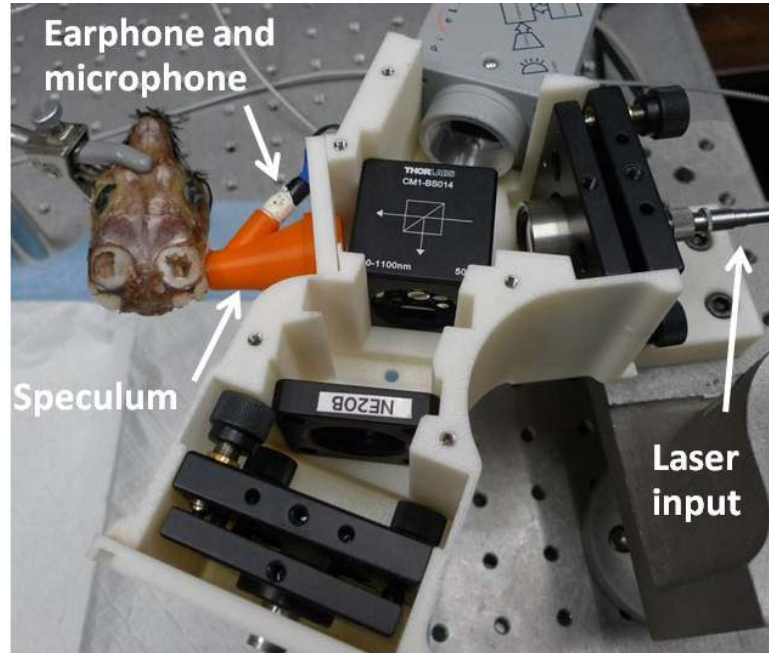


Fig. 8.4. Experimental setup for measurements on a chinchilla TM.

One wavelength used in shape measurement is 779.8 nm and the other is 780.2 nm. Therefore the synthetic wavelength is 1.52 mm. The wrapped phase and unwrapped phase with mask are shown in Fig. 8.5. The white mark shows the location of the manubrium. After image processing, a 3D plot of the TM shape is shown Fig. 8.6. The red arrow shows the light direction. The length of the manubrium is 5.74 mm, the width in the direction perpendicular to manubrium is 4.50 mm and the height from the edge of the TM to the top of the manubrium is 1.4 mm.

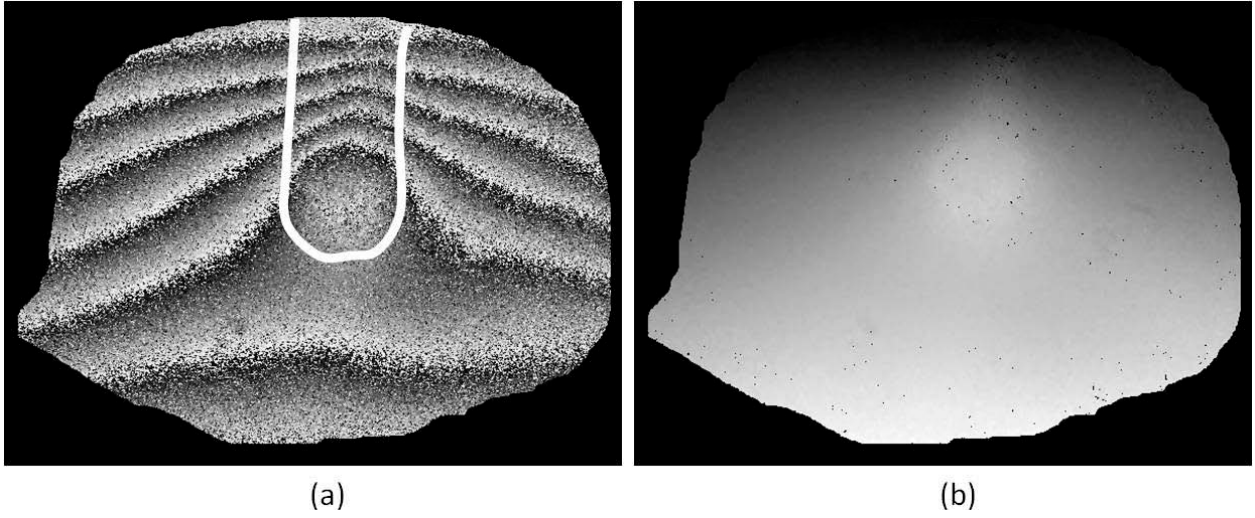


Fig. 8.5. Holographic images for shape measurements: (a) wrapped phase image, and (b) unwrapped phase image. Fig. (a) shows the location of the manubrium by a white contour.

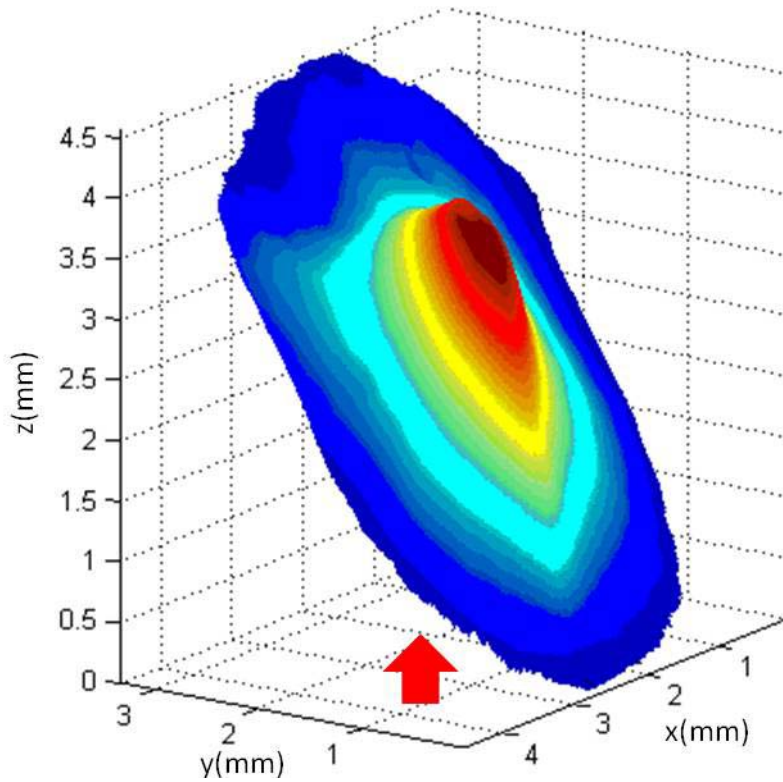


Fig. 8.6. 3D plot of the measured shape. The arrow indicates external side of the TM.

For deformation measurements, sound stimuli were continuous tones at seven frequencies: 800 Hz, 1.5 kHz, 2 kHz, 4.317 kHz, 5 kHz, 6.771 kHz and 10 kHz, with stimulus level set between 70 dB and 120 dB SPL so as to produce measurable sound-induced TM deformations at each measurement frequency and stimulus level. A video that contains several sets of stimulus phase images were recorded. The stimulus phase was starting from 0 to 2π with a step of $\pi/4$.

z -axis deformations were directly measured from this holographic instrument, shown in Fig. 8.7. Figure 8.7 shows deformations of different stimulus frequencies at phase π , where the maximum resultant deformations always happen based on the observation from the video. The deformation patterns of 800 Hz are “simple”, which is characterized by one or two regions of maximal deformation. The deformation patterns of 1.5 kHz and 2 kHz are “complex”, which is characterized by multiple regions of maximal deformation separated by area of small deformation. Above 4 kHz, the deformation patterns of chinchilla TM are “ordered”, which is characterized by many small areas of maximal deformation around the manubrium.

Based on z -axis deformations and shape information, x -axis, y -axis and resultant deformations were predicted, shown in Fig. 8.8. From Fig. 8.8, it is clear to see that there are large magnitudes of x -axis and y -axis deformations with respect to z -axis deformations, which can effect on the resultant deformations significantly. One explanation of these large magnitudes of x -axis and y -axis deformations is that the TM surface is not placed perpendicular to the optical axis which can be observed from the shape plot Fig. 8.6. However, this case is similar to the real one. In the real case, if the speculum connected with OH is inserted into the ear canal, the optical axis could not be perpendicular to the TM either since there is an angle between the TM and the ear canal. Therefore obtaining 3D deformations is significant for learning the entire motions of the TM.

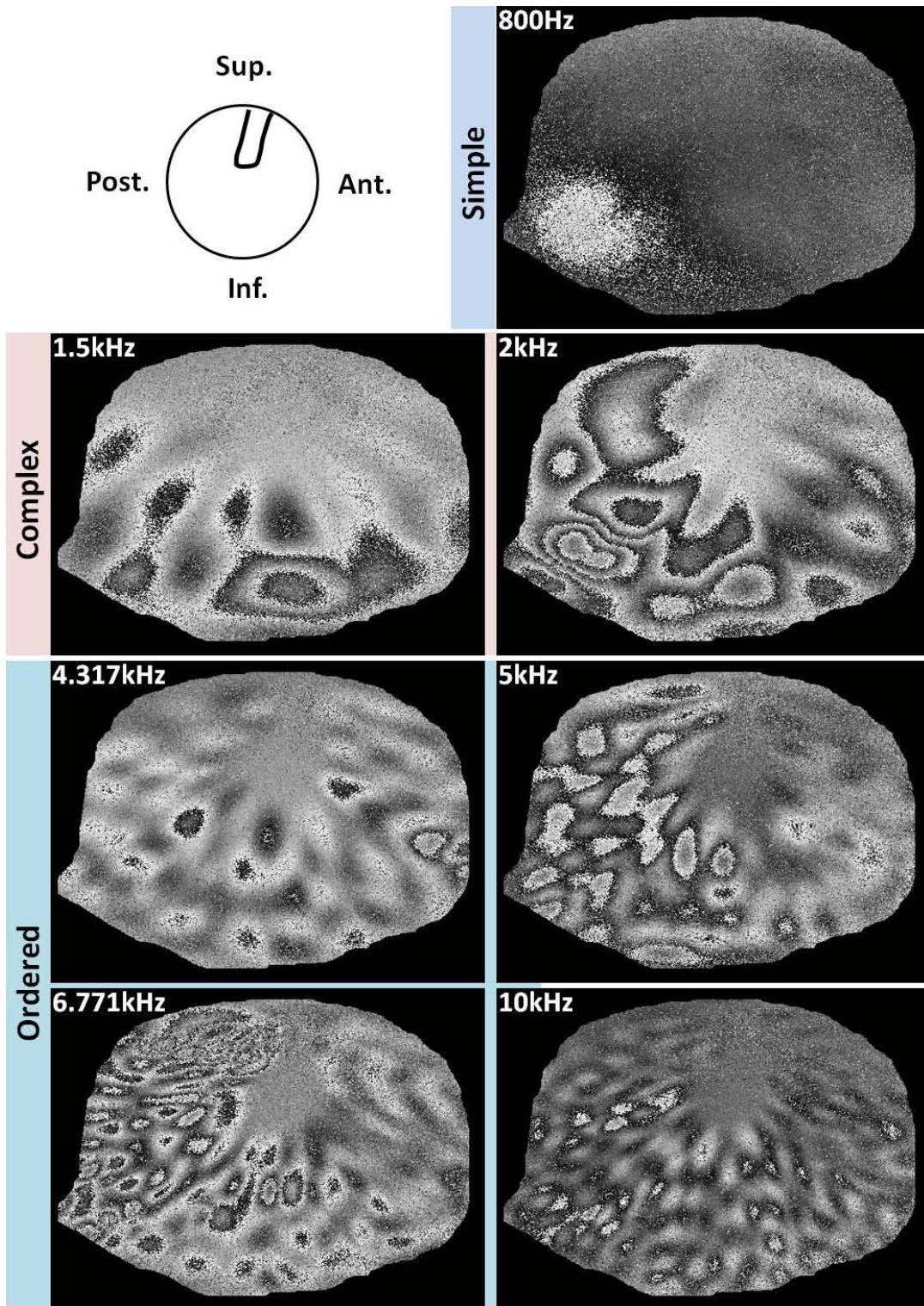


Fig. 8.7. Wrapped optical phase of the measured z -axis deformations of different stimulus frequencies at phase π . For orientation, the posterior (Post.), anterior (Ant.), superior (Sup.) and inferior (Inf.) are shown.

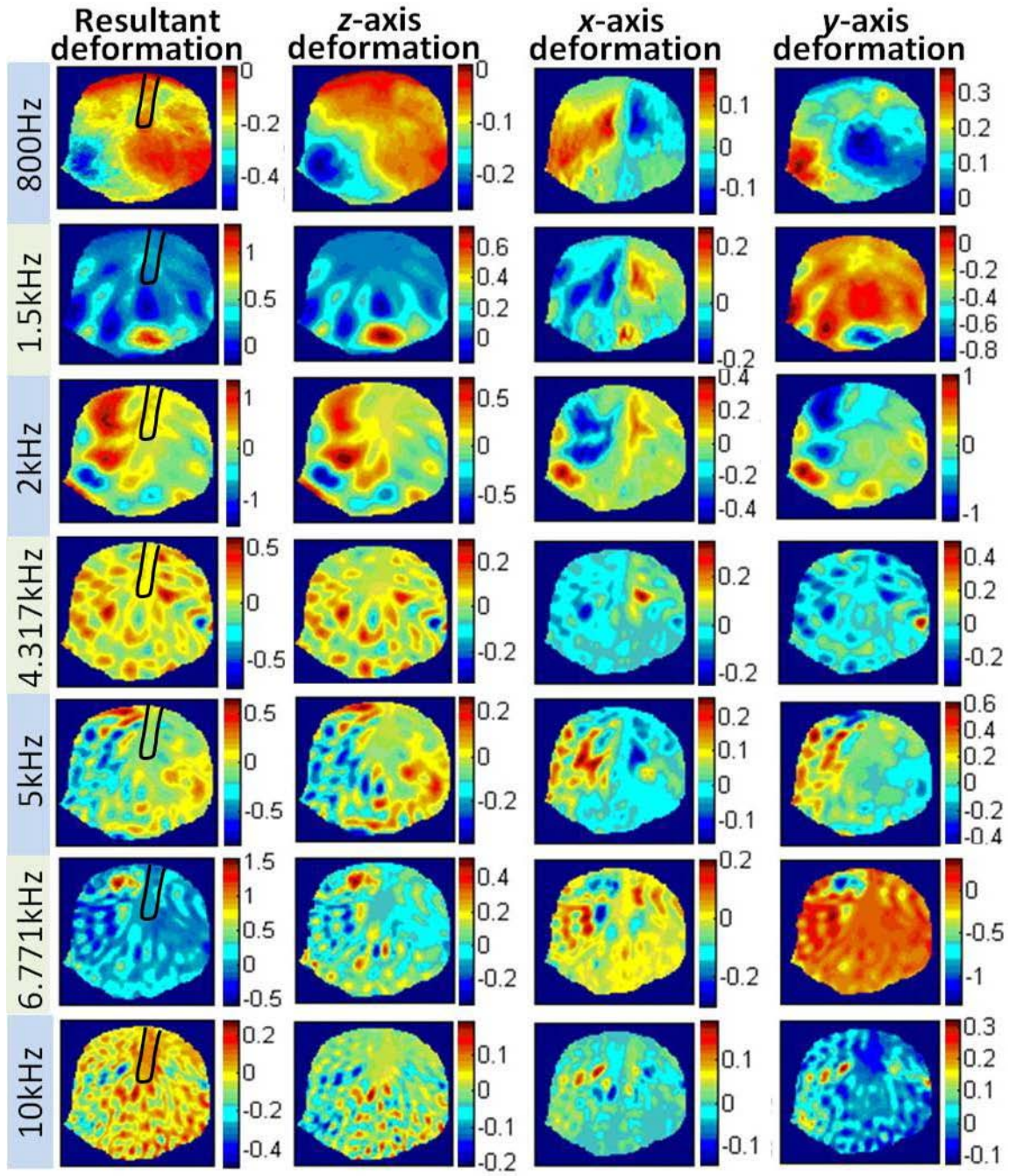


Fig. 8.8. The resultant, z-axis, x-axis and y-axis deformations of the entire TM of different stimulus frequencies at phase π . The unit of deformations is μm .

Figures 8.9 to 8.15 show perspective 3D plots of the instantaneous resultant deformations of the entire TM surface at eight stimulus phases for stimulus frequencies. The orientation of the TM and the location of the manubrium are shown in the first plot at phase 0.

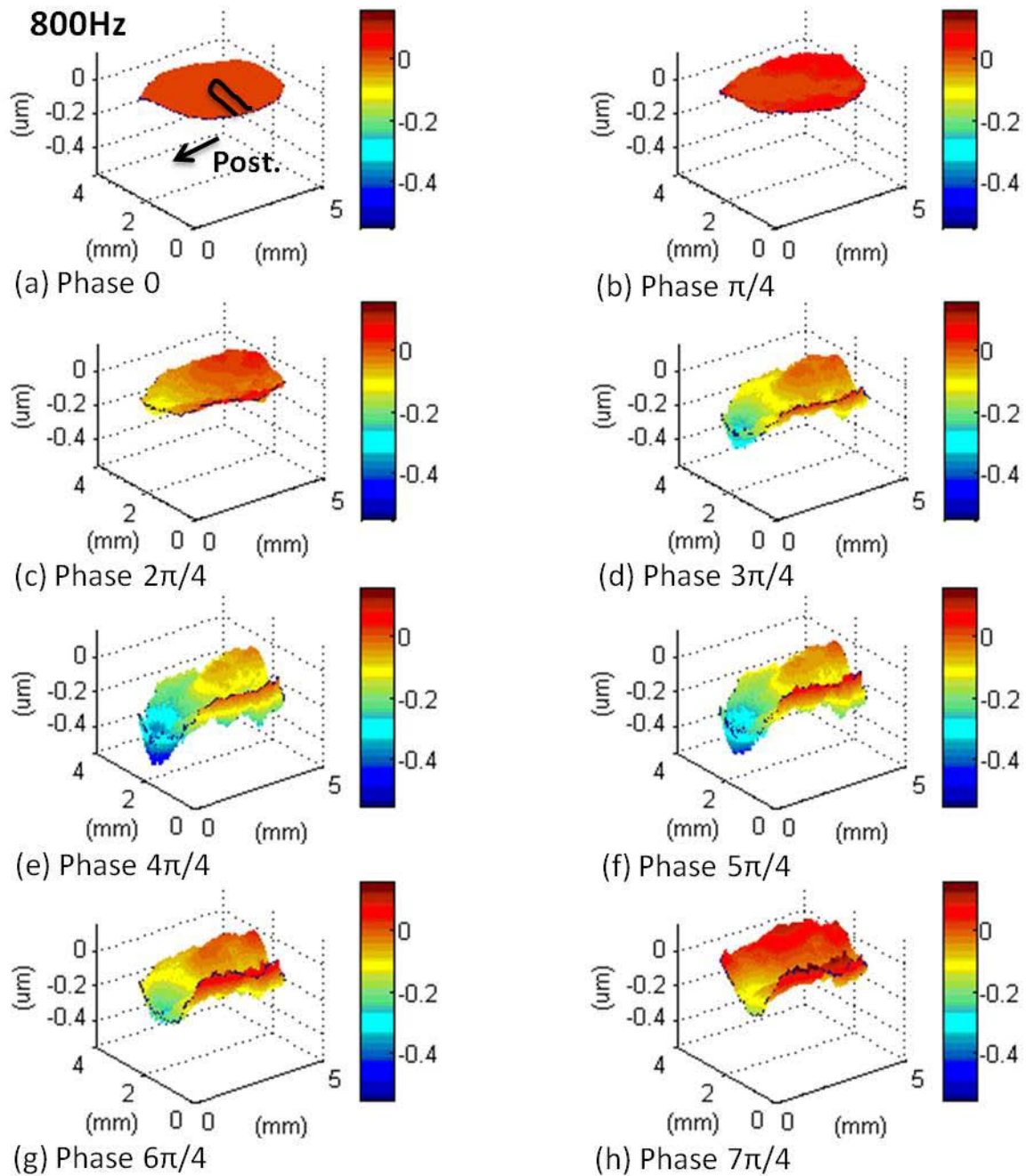


Fig. 8.9. Perspective 3D plots of the instantaneous resultant deformations of the entire TM surface at eight stimulus phases at 800 Hz. The orientation of the TM and the location of the manubrium are shown in the first plot.

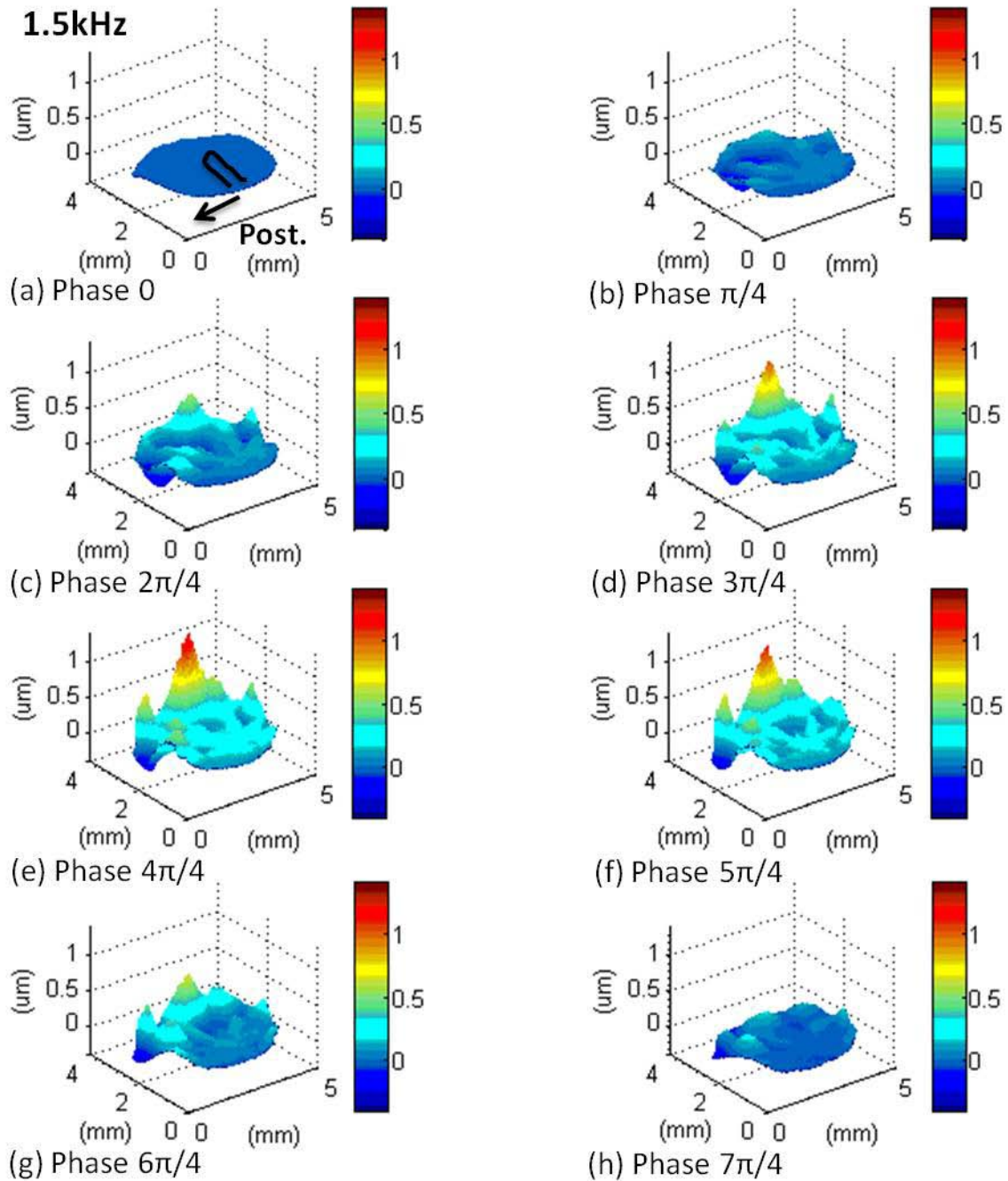


Fig. 8.10. Perspective 3D plots of the instantaneous deformations of the entire TM surface at eight stimulus phases at 1.5 kHz. The orientation of the TM and the location of the manubrium are shown in the first plot.

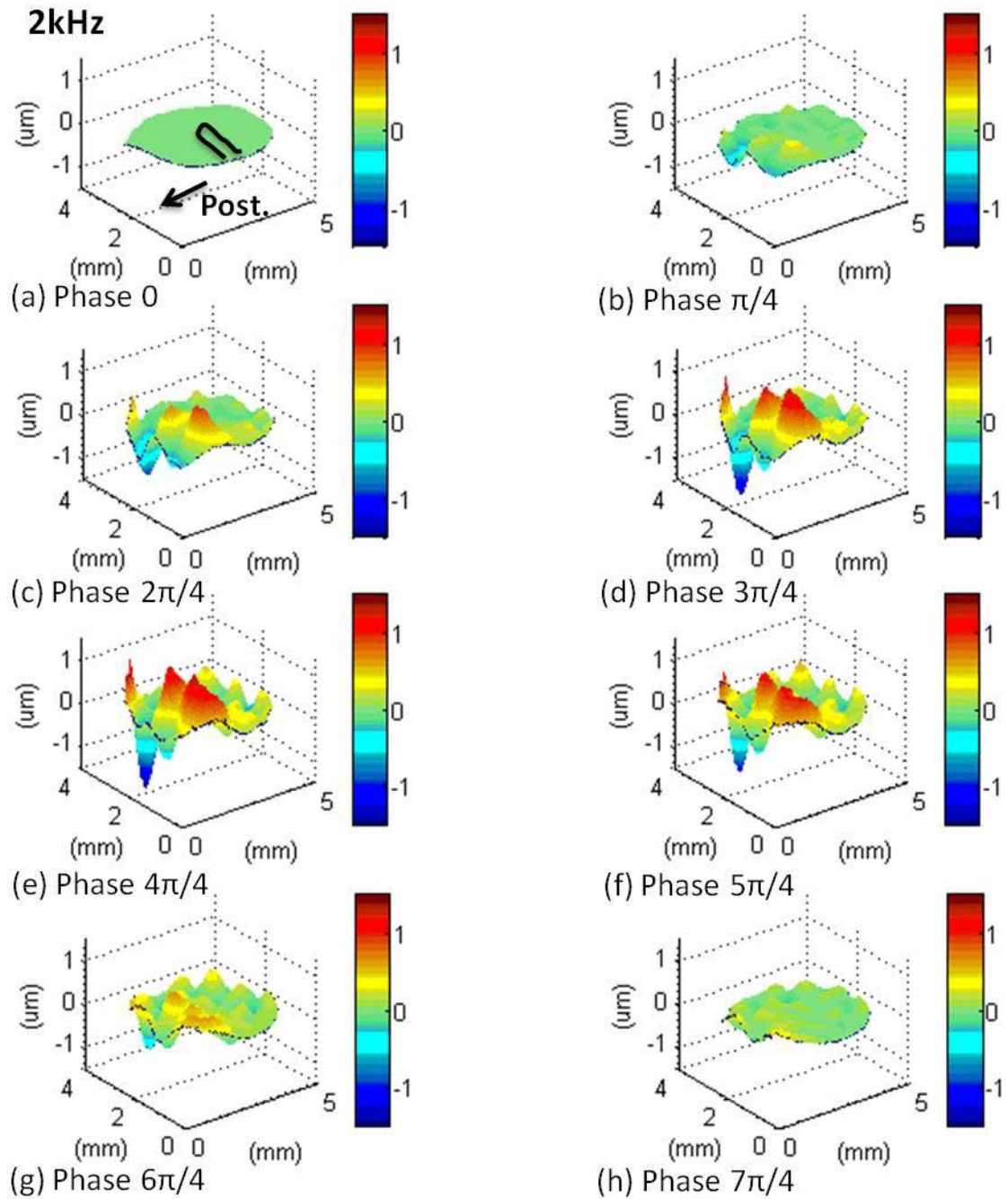


Fig. 8.11. Perspective 3D plots of the instantaneous deformations of the entire TM surface at eight stimulus phases at 2 kHz. The orientation of the TM and the location of the manubrium are shown in the first plot.

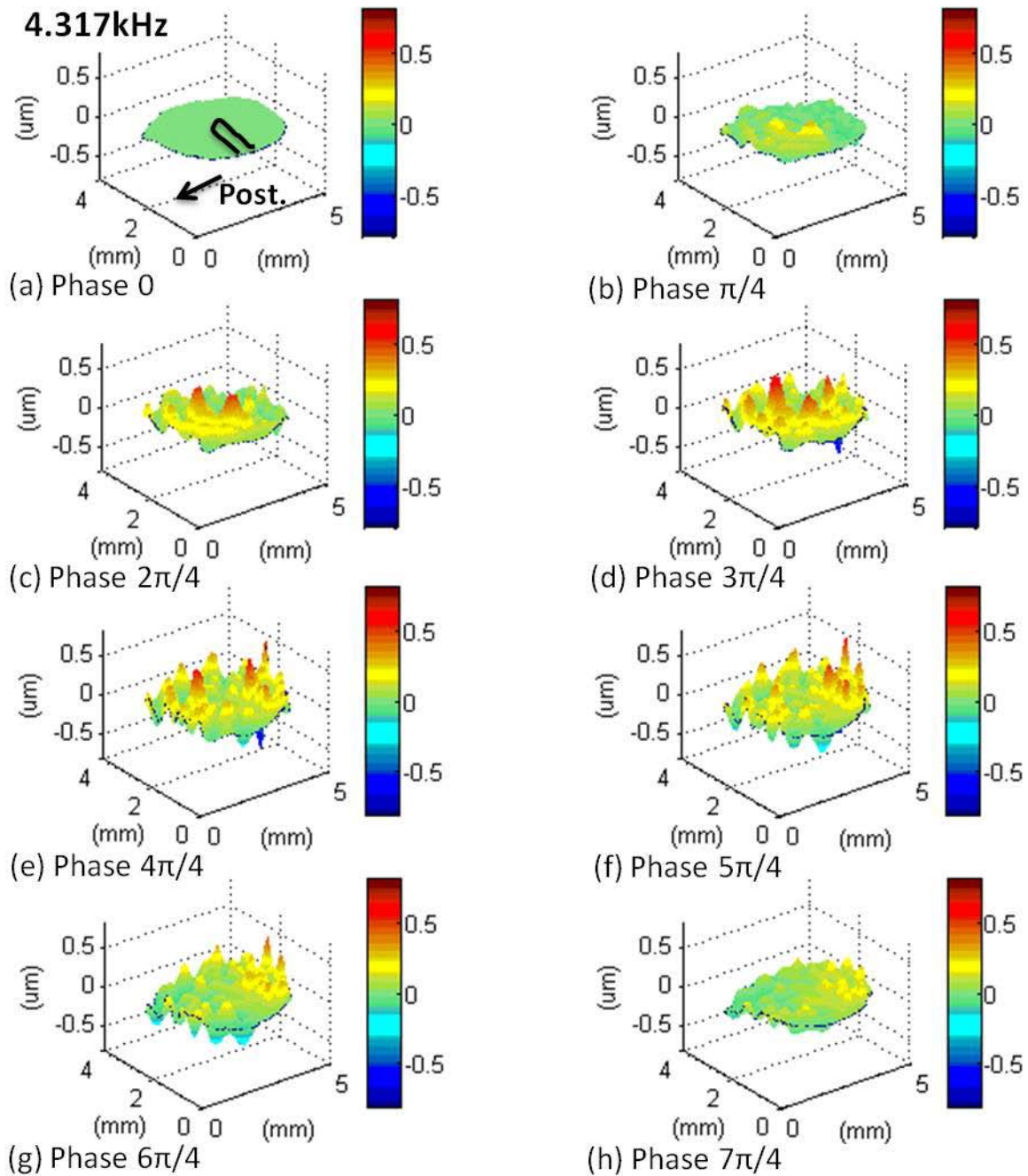


Fig. 8.12. Perspective 3D plots of the instantaneous deformations of the entire TM surface at eight stimulus phases at 4.317 kHz. The orientation of the TM and the location of the manubrium are shown in the first plot.

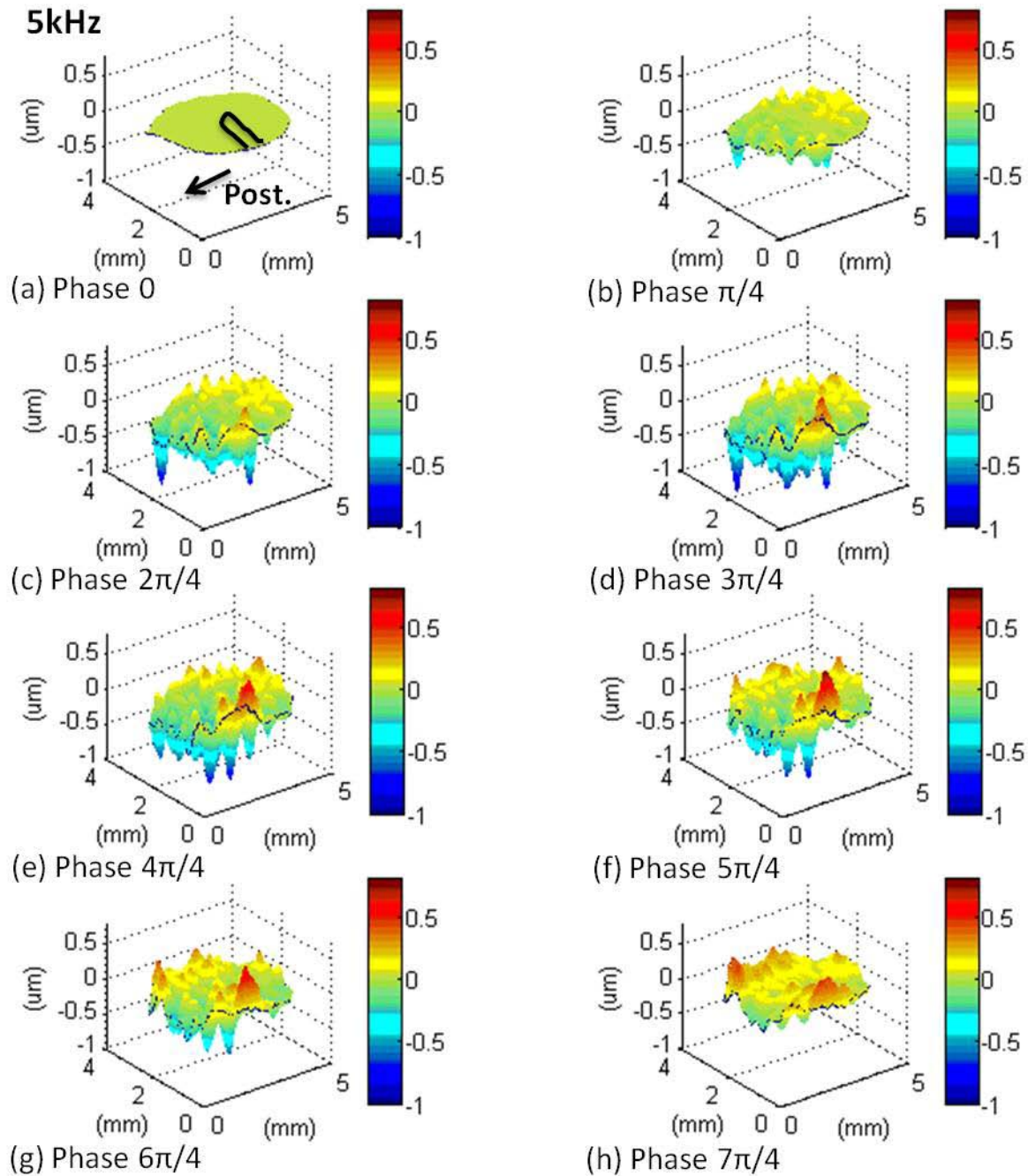


Fig. 8.13. Perspective 3D plots of the instantaneous deformations of the entire TM surface at eight stimulus phases at 5 kHz. The orientation of the TM and the location of the manubrium are shown in the first plot.

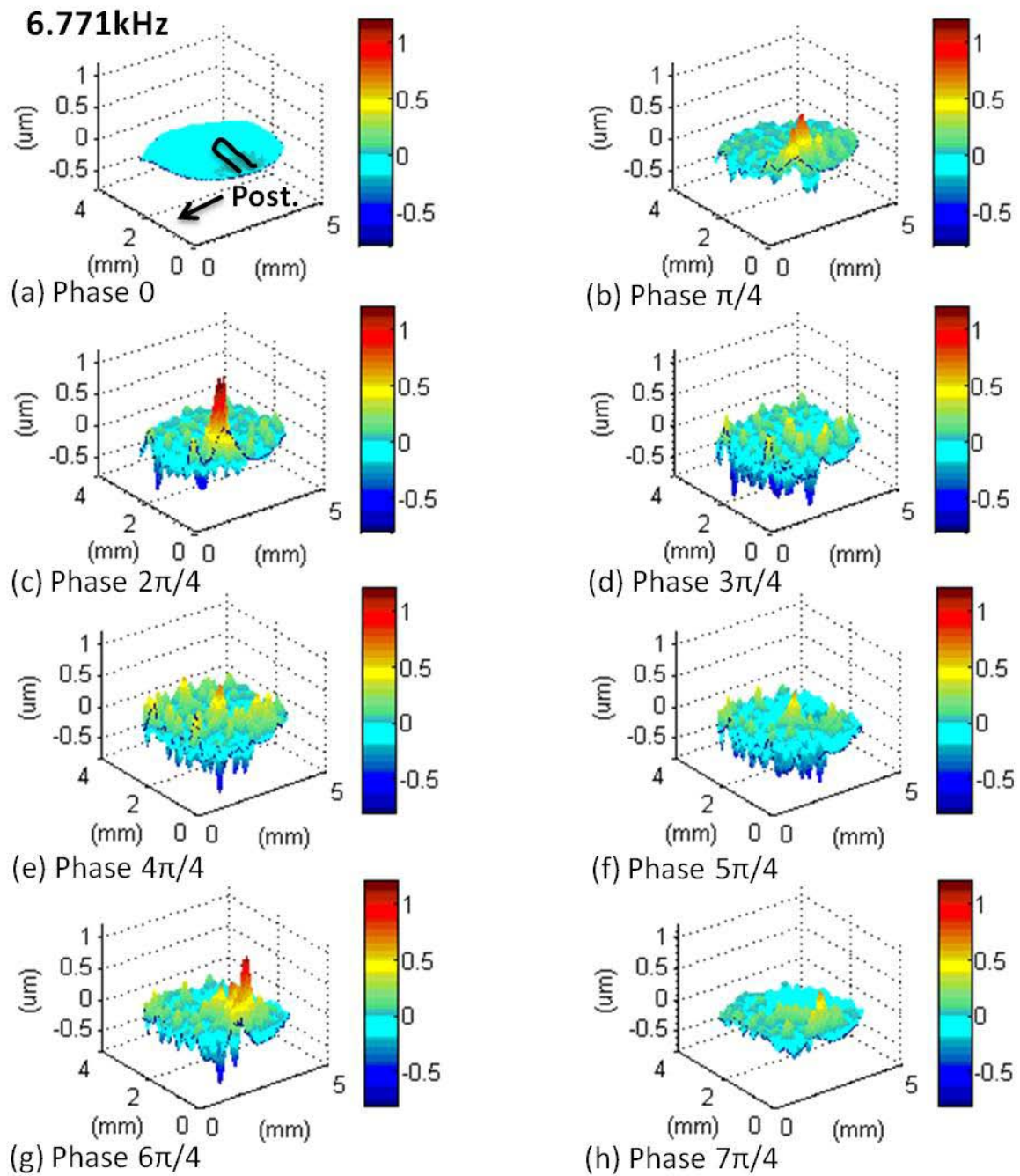


Fig. 8.14. Perspective 3D plots of the instantaneous deformations of the entire TM surface at eight stimulus phases at 6.771 kHz. The orientation of the TM and the location of the manubrium are shown in the first plot.

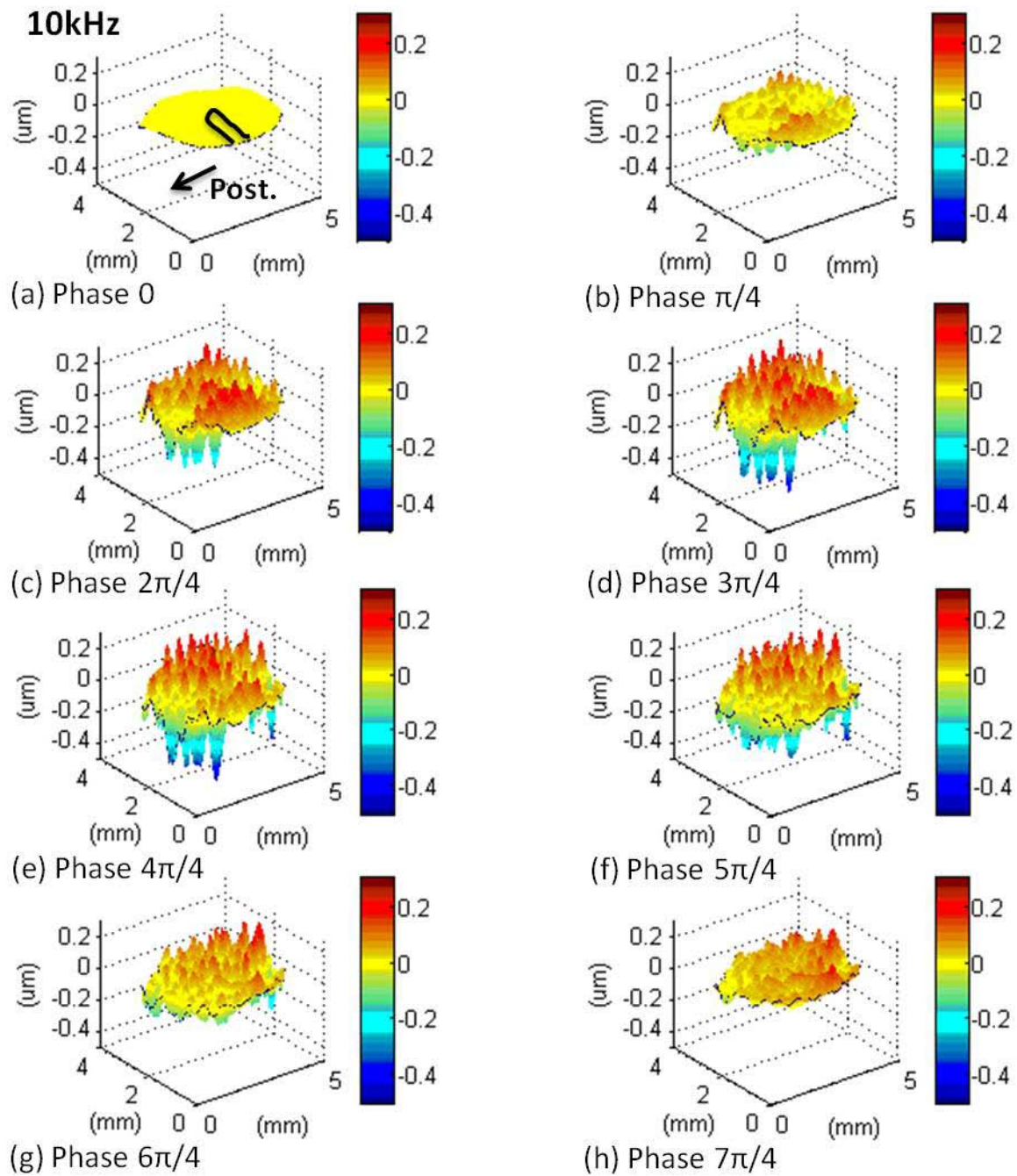


Fig. 8.15. Perspective 3D plots of the instantaneous deformations of the entire TM surface at eight stimulus phases at 10 kHz. The orientation of the TM and the location of the manubrium are shown in the first plot.

9 Conclusions and future work

The most significant achievements of this work are reporting for the very first time measurements of both 3D deformations and shape of the TM by a single optical setup, which is a truly awe-inspiring and state-of-the-art technique in the world. Three main additional contributions have been done in this project: (1) theory establishment and validation for the generation of 3D deformations; (2) hardware development (LD and OH subsystems) with optimized optical components; and (3) applications on artificial samples and a chinchilla TM.

Further research could be made in the following aspects:

- (1) Develop the 2nd generation of OH prototype: by improving these mechanical designs to overcome external vibration effects; be portable on the robot arm; a better way to connect with the speculum;
- (2) More research on optical properties of the TM tissue and optical ray tracing to further understand laser to tissue interaction;
- (3) Continue multi-wavelength research: find out which combination of multiple wavelengths have the best fringes contrast; update software to control wavelength automatically;
- (4) Modify the parameters that are applied on equations of 3D deformation calculation, such as add constants in Eq. 5.14(a) and Eq. 5.14(b);
- (5) Interpret TM motions related with ossicles;
- (6) Measure 3D deformations and shape on human TMs, and understand their significance.

10 References

- Aarnisalo, A. A., Cheng, J. T., Ravicz, M. E., Furlong, C., Merchant, S. N., and Rosowski, J. J. (2010). "Motion of the tympanic membrane after cartilage tympanoplasty determined by stroboscopic holography." *Hearing Research* **263**(1–2): 78-84.
- Aarnisalo, A. A., Cheng, J. T., Ravicz, M. E., Hulli, N., Harrington, E. J., Hernandez-Montes, M. S., Furlong, C., Merchant, S. N., and Rosowski, J. J. (2009). "Middle Ear Mechanics of Cartilage Tympanoplasty Evaluated by Laser Holography and Vibrometry." *Otology & Neurotology* **30**(8).
- Bapat, N. (2011). Development of sound presentation system (SPS) for characterization of sound Induced displacements in tympanic membranes. Department of Mechanical Engineering. Worcester, Worcester Polytechnic Institute. **M.S. Thesis**.
- Cheng, J. T., Aarnisalo, A. A., Harrington, E. J., Hernandez-Montes, M. S., Furlong, C., Merchant, S. N., and Rosowski, J. J. (2010). "Motion of the surface of the human tympanic membrane measured with stroboscopic holography." *Hearing Research* **263**(1–2): 66-77.
- Chole, R. A., and Kodama, K. (1989). "Comparative histology of the tympanic membrane and its relationship to cholesteatoma." *Ann. Otol. Rhinol. Laryngol.* **98**: 761-766.
- Csillag, A. L. (2005). "Atlas of the sensory organs: functional and clinical anatomy." *Humana Press*.
- Dancer, A. L., Franke, R. B., Smigielski, P., Albe, F., and Fagot, H. (1975). "Holographic interferometry applied to the investigation of tympanic-membrane displacements in guinea pig ears subjected to acoustic impulses." *The Journal of the Acoustical Society of America* **58**(1): 223-228.
- Decraemer, W. F., and Dirckx, J. J. (1991). "Moire-shift interferometer measurements of the shape of human and cat tympanic membrane." *Proc. SPIE* **1429**, 26.
- Decraemer, W. F., Dirckx, J. J., and Funnell, W. R. (1991). "Shape and derived geometrical parameters of the adult, human tympanic membrane measured with a phase-shift moiré interferometer." *Hearing Research* **51**(1): 107-121.
- Decraemer, W. F., and Funnell, W. R. J. (2008). "Anatomical and mechanical properties of the tympanic membrane." *Chronic Otitis Media*. B. Ars. The Haugue: 51-84.
- Dirckx, J. J., and Decraemer, W.F. (1996). "Reflective coatings in optical interferometry for in vitro studies of the eardrum." *Proc. SPIE* **2927**(1): 2.
- Dirckx, J. J., and Decraemer, W. F. (1991). "Deformation measurements of the human tympanic membrane under static pressure using automated moire topography." *Proc. SPIE* **1429**, 34.
- Dirckx, J. J., and Decraemer, W. F. (1997). "Optoelectronic moire projector for real-time shape and deformation studies of the tympanic membrane." *J. Biomed. Opt.* **2**, 176.
- Dirckx, J. J. J., Buytaert, J. A. N., and Jeught, S. A. M. V. D. (2010). "Implementation of phase-shifting moiré profilometry on a low-cost commercial data projector." *Optics and Lasers in Engineering* **48**(2): 244-250.
- Dirckx, J. J. J., and Decraemer, W. F. (1989). "Phase shift moire apparatus for automatic 3D surface measurement," *Rev. Sci. Instrum.* **60**, 3698.
- Dirckx, J. J. J., and Decraemer, W. F. (1997). "Coating techniques in optical interferometric metrology." *Appl. Opt.* **36**(13): 2776-2782.

- Dirckx, J. J. J., and Decraemer, W. F. (2000). "Interferometer for Eardrum Shape Measurement, Based on Projection of Straight Line Rulings." *Lasers in Medical Science* **15**(2): 131-139-139.
- Dirckx, J. J. J., Decraemer, W. F., von, U. M., and Larsson, C. (1997). "Measurement and modeling of boundary shape and surface deformation of the Mongolian gerbil pars flaccida." *Hearing Research* **111**(1-2): 153-164.
- Dobrev I., Flores-Moreno J. M., Furlong C., Harrington E. J., Rosowski J. J., and Scarpino C. (2010). "Design of a positioning system for a holographic otoscope," *Proc. SPIE*, **7791**:D1-D12.
- Dobrev, I., Furlong, C., and Rosowski, J. J. (2011). "Design of a mechatronic positioner for a holographic otoscope system." *Proc. SEM* **9999**: 193-198.
- Flores-Moreno J. M., Furlong C., Rosowski J. J., Harrington E., Cheng J. T., Scarpino C., Mendoza S. F. (2011). "Holographic otoscope for nano-displacement measurements of surfaces under dynamic excitation." *The Journal of Scanning Microscopies* **33**: 342-352.
- Furlong, C., and Pryputniewicz, R. J. (2000). "Absolute shape measurements using high-resolution optoelectronic holography methods." *Opt. Eng.* **39**(1): 216.
- Furlong, C., Rosowski, J. J., Hulli, N., and Ravicz, M.E. (2009). "Preliminary Analyses of Tympanic-Membrane Motion from Holographic Measurements." *Strain* **45**(3): 301-309.
- Goldish, S., and Kunyz, T. (2010). "Packaging and optimization of a digital holographic otoscope for clinical use." Department of Mechanical Engineering. Worcester, Worcester Polytechnic Institute. **MQP**.
- Goode, R. L., Ball, G., and Nishihara, S. (1993). "Measurement of Umbo Vibration in Human Subjects-Method and Possible Clinical Applications." *Otology & Neurotology* **14**(3).
- Goode, R. L., Ball, G., Nishihara, S., and Nakamura K. (1996). "Laser Doppler vibrometer (LDV)--a new clinical tool for the otologist." *Am. J. Otol.* **17**(6): 813-22.
- Harrington, E., Dobrev, I., Bapat, N., and Flores, J. M. (2010). "Development of an optoelectronic holographic platform for otolaryngology applications." *Proc. SPIE* **7791**(1): 77910J.
- Harrington, E., Furlong, C., Rosowski, J. J., and Cheng, J.T. (2011). "Automatic Acquisition and Processing of Large Sets of Holographic Measurements in Medical Research." *Proc. SEM* **9999**: 219-228.
- Hear-it. (2011) from <http://www.hear-it.org/page.dsp?area=858>.
- Hernandez-Montes, M. d. S., Furlong, C., Rosowski, J. J., Hulli, N., Harrington, E., Cheng, J. T., Ravicz, M. E., and Santoyo, F. M. (2009). "Optoelectronic holographic otoscope for measurement of nano-displacements in tympanic membranes." *Journal of Biomedical Optics* **14**(3): 034023-034029.
- Huber, A. M., Schwab, C., Linder, T., Stoeckli, S. J., Ferrazzini, M., Dillier, N., and Fisch, U. (2001). "Evaluation of Eardrum Laser Doppler Interferometry as a Diagnostic Tool." *The Laryngoscope* **111**(3): 501-507.
- Hulli, N. (2008). "Development of an optoelectronic holographic otoscope system for characterization of sound-induced displacements in tympanic membranes." Department of Mechanical Engineering. Worcester, Worcester Polytechnic Institute. **M.S. Thesis**.
- Jakob, A., Bornitz, M., Kuhlisch, E., and Zahnert, T. (2009). "New Aspects in the Clinical Diagnosis of Otosclerosis Using Laser Doppler Vibrometry." *Otology & Neurotology* **30**(8).

- Karasic, G., and Largesse N. (2009). "Miniaturization of an optoelectronic holographic otoscope for measurement of nanodisplacements in tympanic membranes. " Department of Mechanical Engineering, Worcester, Worcester Polytechnic Institute. **MQP**.
- Katz, J. (2002). "Handbook of clinical audiology. " *Lippincott Williams & Wilkins*.
- Khanna, S. M., and Tonndorf, J. (1972). "Tympanic Membrane Vibrations in Cats Studied by Time-Averaged Holography." *The Journal of the Acoustical Society of America* **51**(6B): 1904-1920.
- Koike, T., Wada, H., and Kobayashi, T. (2002). "Modeling of the human middle ear using the finite-element method." *J. Acoust. Soc. Am.* **111**(3): 1306.
- Kraus, H. (1967). "Thin elastic shells: an introduction to the theoretical foundations and the analysis of their static and dynamic behavior. " *Wiley*.
- Kreis, T. (2005). "Handbook of holographic interferometry: optical and digital methods." *Wiley-VCH*.
- Ladak, H. M., Decraemer, W. F., Dirckx, J. J., and Funnell, W. R. (2004). "Response of the cat eardrum to static pressures: Mobile versus immobile malleus." *J. Acoust. Soc. Am.* **116**(5): 3008-21.
- Lim, D. J. (1995). "Structure and function of the tympanic membrane: a review." *Acta oto-rhino-laryngologica Belg.* **49**: 101-115.
- Løkberg, O. J., Høgmoen, K., and Holje, O. M. (1979). "Vibration measurement on the human ear drum in vivo." *Applied Optics* **18**: 763-765.
- Lu, W., Furlong, C., Rosowski, J. J., Cheng, J. T., and Merchant, S. N. "Characterization of Shape and Deformation of Tympanic Membranes by Dual-wavelength Lensless Digital Holography." *Proc. SEM* **9999**: 299-307.
- Maeta, M., Kawakami, S., Ogawara, T., and Masuda, Y. (1991). "Vibration analysis of the tympanic membrane with a ventilation tube and a perforation by holography." *Proc. SPIE* **1429**, 152.
- Martínez-Celorio, R. A., Dirckx, J. J. J., Marti-Lopez L., and Pena-Lecona, F. G. (2004). "Out-of-plane displacement measurement by means of endoscopic moiré interferometry." *Rev. Sci. Instrum.* **75**, 492.
- O. J. Løkberg, Høgmoen, K., and Gundersen, T. (1980). "Vibration measurement of the human tympanic membrane--in vivo." *Acta Otolaryngol* **89**: 37-42.
- Powell, R. L., and Stetson, K. A. (1965). "Interferometric vibration analysis by wavefront reconstruction." *J. Opt. Soc. Am.* **55**(12).
- Pryputniewicz, R. J. (1985). "Time average holography in vibration analysis." *Opt. Eng.* **24**(5): 843-848.
- Pryputniewicz, R. J. (1987). "Quantitative interpretation of time-average holograms in vibration analysis." *Optical metrology*. Porto, Portugal: 296-371.
- Pryputniewicz, R. J. (1989). "Measurement of vibration patterns using electro-optic holography." *SPIE* **1162**: 456-467.
- Pryputniewicz, R. J. (1996). "Holographic numerical analysis." ME/CHSLT-NEST, Worcester Polytechnic Institute, Worcester, MA.
- Rosowski, J. J., Mehta, R. P., and Merchant, S. N. (2003). "Diagnostic Utility of Laser-Doppler Vibrometry in Conductive Hearing Loss with Normal Tympanic Membrane." *Otology & Neurotology* **24**(2).

- Rosowski, J. J., Nakajima, H. H., and Merchant, S. N. (2008). "Clinical Utility of Laser-Doppler Vibrometer Measurements in Live Normal and Pathologic Human Ears." *Ear and Hearing* **29**(1).
- Saada, A. S. (2009). "Elasticity: theory and applications." *J. Ross Pub.*
- Schubert, E. D. (1980). "Hearing, its function and dysfunction." *Springer-Verlag.*
- Standring, S., and Gray, H. (2008). "Gray's anatomy: the anatomical basis of clinical practice." *Churchill Livingstone/Elsevier.*
- Ventsel, E., and Krauthammer, T. (2001). "Thin plates and shells: theory, analysis, and applications." *Marcel Dekker.*
- von Unge, M., Decraemer, W. F., Bagger-Sjögäck, D., and Dirckx, J. J. (1993). "Displacement of the gerbil tympanic membrane under static pressure variations measured with a real-time differential moire interferometer." *Hearing Research* **70**(2): 229-242.
- von Unge, M., Decraemer, W. F., Dirckx, J. J., and Bagger-Sjögäck, D. (1995). "Shape and displacement patterns of the gerbil tympanic membrane in experimental otitis media with effusion." *Hearing Research* **82**(2): 184-196.
- von Unge, M., Decraemer, W. F., Dirckx, J. J., and Bagger-Sjögäck, D. (1999). "Tympanic membrane displacement patterns in experimental cholesteatoma." *Hearing Research* **128**(1-2): 1-15.
- Wagner, C., Osten, W., and Seebacher, S. (2000). "Direct shape measurement by digital wavefront reconstruction and multiwavelength contouring." *Opt. Eng.* **39**(1): 79.
- Wajnberg, J. M. D. (1987). "The true shape of the tympanic membrane." *The Journal of laryngology and otology* **101**: 538-541.
- Whittemore, K. R., Merchant, S. N., Poon, B. B., and Rosowski, J. J. (2004). "A normative study of tympanic membrane motion in humans using a laser Doppler vibrometer (LDV)." *Hearing Research* **187**(1-2): 85-104.
- Wikipedia. (2008) from <http://upload.wikimedia.org/wikipedia/commons/7/7c/HumanEar.jpg>.

APPENDIX A: MATLAB program for theory validation and accuracy analysis of normal vectors.

```
%%
clc; clear all; close all;

%% Section 1: deformations from FEA software

% How many quote lines to skip (Title & name of columns)
nlc = 5;
% Number of column (# element included)
nbc = 5;

%% Open dialog box for file loading

% Save file from Solidworks named as "mode#-disp.txt" & "mode#-shape.txt"

[name, folder] = uigetfile({'*.txt', 'txt-files *.txt'}, 'File
Selector', 'E:\weina\Solidworks\thinshell\spherical\1_160_0.0625thick_5radius')
;
% path needs to be changed
filename = ([folder, name]);
savename = ([filename(1:strfind(filename, '-')-1), '.mat']);

%% mode#-#.txt

Names = name(1:strfind(name, '-'));
f{1, :} = {[folder, names, 'disp', '.txt']};
f{2, :} = {[folder, names, 'shape', '.txt']};
clear filename name folder names

%% Read data

for n = 1:size(f,1)
    filename = cell2mat(f{n, :});
    name = filename(strfind(filename, '-')+1:end);
    fid = fopen(filename);
    for i = 1:nlc
        tline = fgetl(fid);
        disp(tline) %remove the title line
    end

    A = fscanf(fid, '%g %g %g %g %g', [nbc inf]);
    fclose(fid);
    switch name
        case 'disp.txt'
            DATA_disp = A;
        case 'shape.txt'
            DATA_shape = A;
    end
end
end
```

```

if isequal(DATA_disp(:,1),DATA_shape(:,1))==1
    nodes = DATA_disp(:,1);
    X = DATA_shape(:,2);
    Y = DATA_shape(:,3);
    Z = DATA_shape(:,4);
    UX = DATA_disp(:,2);
    UY = DATA_disp(:,3);
    UZ = DATA_disp(:,4);
    URES = DATA_disp(:,5);
else
    disp('STOP! Order nodes first!')
end

%% Save data

save(savename, 'nodes', 'X', 'Y', 'Z', 'UX', 'UY', 'UZ', 'URES')
disp('Saved')
clear A f DATA_disp DATA_shape fid filename i n name tline nlc nbc col ans
savename

%% Correct URES

for i = 1:size(nodes,1)
    if UZ(i)<0
        URES(i)= -URES(i);
    else URES(i)= URES(i);
    end
end

%% Rescaling

UX = UX./100000;
UY = UY./100000;
UZ = Z./100000;
URES = URES./100000;

%% Convert vectors to matrix

Px = 499;    % points / line; odd num better
Py = 499;    % points /column; odd num better

[XX, YY] = meshgrid(linspace(min(X),max(X),Px),linspace(min(Y),max(Y),Py));

%% Interpolate

UX_matrix = griddata(X,Y,UX,XX,YY);
UY_matrix = griddata(X,Y,UY,XX,YY);
UZ_matrix = griddata(X,Y,UZ,XX,YY);
URES_matrix = griddata(X,Y,URES,XX,YY);

```

```

%% Plot deformations in x,y,z directions

figure(1)
mesh(XX,YY,UX_matrix)
set(findobj('Type','patch'),'LineStyle','none');
title('X deformation','FontSize',14,'FontWeight','bold')
xlabel('x (mm)');ylabel('y (mm)');

figure(2)
mesh(XX,YY,UY_matrix)
set(findobj('Type','patch'),'LineStyle','none');
title('Y deformation','FontSize',14,'FontWeight','bold')
xlabel('x (mm)');ylabel('y (mm)');

figure(3)
mesh(XX,YY,UZ_matrix)
set(findobj('Type','patch'),'LineStyle','none');
title('Z deformation','FontSize',14,'FontWeight','bold')
xlabel('x (mm)');ylabel('y (mm)');

figure(4)
mesh(XX,YY,URES_matrix)
set(findobj('Type','patch'),'LineStyle','none');
title('RES deformation','FontSize',14,'FontWeight','bold')
xlabel('x (mm)');ylabel('y (mm)');

%% Section 2 - Surface normal vectors--normals accuracy

% Spherical shape
r = 5;      % shape curvature
Z_calculate = sqrt(r^2-X.^2-Y.^2);
Z_calculate_modify = Z_calculate-min(Z_calculate(:));

[X_shape, Y_shape] =
meshgrid(linspace(min(X),max(X),Px),linspace(min(Y),max(Y),Py));
Z_shape = griddata(X,Y,Z_calculate_modify,X_shape,Y_shape);

figure(5)
surf(XX,YY,Z_shape,'LineStyle','none')
axis equal
title('Shape','FontSize',14,'FontWeight','bold')
xlabel('x (mm)');ylabel('y (mm)');zlabel('z (mm)');

% Get surface normals by matlab fun. "surfnorm"

[Nx,Ny,Nz] = surfnorm((Px/5)*Z_shape); %px/5=px/diameter of the circle

% Fix x axis at middle,250

central_num = (Px+1)/2;
Vec_Ny = Ny(:,central_num);

```

```

Vec_Nz = Nz(:,central_num);

% Calculate normals by analytical solution

vec_Z_shape = Z_shape(:,central_num)+ min(Z_calculate(:));
vec_radius = r*ones(size(vec_Z_shape));
vec_Y_shape = sqrt((vec_radius).^2-(vec_Z_shape).^2);

for h = 1:central_num
    vec_Y_shape(h) = -vec_Y_shape(h);
end

f_Nz = 2*vec_Z_shape;
f_Ny = 2*vec_Y_shape;
D = sqrt(f_Nz.^2+f_Ny.^2);
f_Nz_normalize = f_Nz./D;
f_Ny_normalize = f_Ny./D;

% Difference between nomrals generated by matlab and by theory

diff_Nz = (f_Nz_normalize-Vec_Nz)./f_Nz_normalize;
diff_Ny = (f_Ny_normalize-Vec_Ny)./f_Ny_normalize;

[zc,zr] = find(isnan(diff_Nz));
for u_z = 1:size(zr)
    diff_Nz(zr(u_z),zc(u_z)) = 0;
end

ind_z = find(diff_Nz(:));
n_z = length(ind_z(:));

RMS_diff_Nz = norm(diff_Nz)/sqrt(n_z);

[yc,yr] = find(isnan(diff_Ny));
for u_y = 1:size(yr)
    diff_Ny(yr(u_y),yc(u_y)) = 0;
end

ind_y = find(diff_Ny(:));
n_y = length(ind_y(:));

RMS_diff_Ny = norm(diff_Ny)/sqrt(n_y);

% Plot--reduce plotted velocity density

N = 20;
N_index = floor(Px/N);
vec_Y_shape_select = zeros(N_index,1);
vec_Z_shape_select = zeros(N_index,1);
f_Ny_normalize_select = zeros(N_index,1);

```

```

f_Nz_normalize_select = zeros(N_index,1);
Vec_Ny_select = zeros(N_index,1);
Vec_Nz_select = zeros(N_index,1);

for i = 1:N_index
    vec_Y_shape_select(i) = vec_Y_shape(N*i);
    vec_Z_shape_select(i) = vec_Z_shape(N*i);
    f_Ny_normalize_select(i) = f_Ny_normalize(N*i);
    f_Nz_normalize_select(i) = f_Nz_normalize(N*i);
    Vec_Ny_select(i) = Vec_Ny(N*i);
    Vec_Nz_select(i) = Vec_Nz(N*i);
end

figure(6)
plot(vec_Y_shape, vec_Z_shape);
hold on
quiver(vec_Y_shape_select,vec_Z_shape_select,f_Ny_normalize_select,f_Nz_normalize_select)
hold on
quiver(vec_Y_shape_select,vec_Z_shape_select,Vec_Ny_select,Vec_Nz_select, 0.8)
hold off
axis equal
xlabel('y(mm)');ylabel('z (mm)');
legend('surface','analytical normal vectors','Matlab normal vectors');

%% Section 4 -- theory validation

% Known: z-axis def + NX,NY,NZ---> unknown x-axis & y-axis def

UX_shape_Zdisp = (Nz).\ (Nx.*UZ_matrix);    % x-axis def
UY_shape_Zdisp = (Nz).\ (Ny.*UY_matrix);    % y-axis def

figure(7)
mesh(UX_shape_Zdisp)
set(findobj('Type','patch'),'LineStyle','none');
title('X-def prediction','FontSize',14,'FontWeight','bold');
xlabel('x');ylabel('y');

figure(8)
mesh(UY_shape_Zdisp)
set(findobj('Type','patch'),'LineStyle','none');
title('Y-def prediction','FontSize',14,'FontWeight','bold');
xlabel('x');ylabel('y');

%% Normalize def and def prediction

% Eliminate the effect of amplitude
UX_matrix=UX_matrix-min(UX_matrix(:));
UY_matrix=UY_matrix-min(UY_matrix(:));
UX_shape_Zdisp=UX_shape_Zdisp-min(UX_shape_Zdisp(:));
UY_shape_Zdisp=UY_shape_Zdisp-min(UY_shape_Zdisp(:));

```

```

UX_nor=UX_matrix/max(UX_matrix(:));
UY_nor=UY_matrix/max(UY_matrix(:));
UX_shape_Zdisp_nor=UX_shape_Zdisp/max(UX_shape_Zdisp(:));
UY_shape_Zdisp_nor=UY_shape_Zdisp/max(UY_shape_Zdisp(:));

%% Compare def with def prediction

MX=UX_nor-UX_shape_Zdisp_nor;

[xrow,xcol]=find(isnan(MX));
for ux=1:size(xrow)
    MX(xrow(ux),xcol(ux))=0;
end
[m_x,n_x]=size(MX);

RMS_X=norm(MX)/sqrt(m_x*n_x);
STD_X=std(MX(:));

MY=UY_nor-UY_shape_Zdisp_nor;

[yrow,ycol]=find(isnan(MY));
for uy=1:size(yrow)
    MY(yrow(uy),ycol(uy))=0;
end
[m_y,n_y]=size(MY);

RMS_Y=norm(MY)/sqrt(m_y*n_y);
STD_Y=std(MY(:));

MDX=max(max(UX_matrix))-min(min(UX_matrix));
MDY=max(max(UY_matrix))-min(min(UY_matrix));

RMS_X=RMS_X/MDX*100;
RMS_Y=RMS_Y/MDY*100;
STD_X=STD_X/MDX*100;
STD_Y=STD_Y/MDY*100;

clc;
disp(['RMS(%) in X direction is ', num2str(RMS_X)]);
disp(['RMS(%) in Y direction is ', num2str(RMS_Y)]);
disp(['STD(%) in X direction is ', num2str(STD_X)]);
disp(['STD(%) in Y direction is ', num2str(STD_Y)]);

%%

figure (9)
subplot(2,2,1)
imagesc(UX_nor);figure(gcf);
title('UX', 'FontSize',10, 'FontWeight', 'bold')
subplot(2,2,2)
imagesc(UY_nor);figure(gcf);
title('UY', 'FontSize',10, 'FontWeight', 'bold')

```

```
subplot(2,2,3)
imagesc(UX_shape_Zdisp_nor);figure(gcf);
title('UX prediction','FontSize',10,'FontWeight','bold')
subplot(2,2,4)
imagesc(UY_shape_Zdisp_nor);figure(gcf);
title('UY prediction','FontSize',10,'FontWeight','bold')
```

APPENDIX B: MATLAB program for 3D deformations and shape measurements

```
% Shape and 3D deformations of Experimental results

clear all; close all; clc;

%% Read data from files

filename_shape_tilt =
'E:\weina\201201119_meei\experiment\shape_v50003_1_phase90_unwrapped_Xtilt0p2_
Ytilt5p5.rti';
[image_shape_tilt,lvvMetadata_shape_tilt,rtiMetadata_shape_tilt] =
readRTI(filename_shape_tilt);

filename_shape =
'E:\weina\201201119_meei\shape_v50003_1_phase90_unwrapped.rti';
[image_shape,lvvMetadata_shape,rtiMetadata_shape] = readRTI(filename_shape);

filename_def =
'E:\weina\201201119_meei\experiment\test_TA_2KHZ_2V\test_TA_2KHZ_2V_phase180_u
nwrapped.rti';
[image_def,lvvMetadata_def,rtiMetadata_def] = readRTI(filename_def);

%% Crop data -- choose area of interest

% minx_image_shape= 368; maxx_image_shape= 940;
% miny_image_shape= 358; maxy_image_shape= 771;
% minx_image_def= 367; maxx_image_def= 942;
% miny_image_def= 356; maxy_image_def= 773;

% check mask size, better to write a loop in future
minx_image = 366; maxx_image= 943;
miny_image = 355; maxy_image= 774;

image_shape_crop = image_shape(miny_image:maxy_image, minx_image:maxx_image);
image_shape_tilt_crop = image_shape_tilt(miny_image:maxy_image,
minx_image:maxx_image);
image_def_crop = image_def(miny_image:maxy_image, minx_image:maxx_image);

X_shape_crop = double(1:maxx_image-minx_image+1)';
Y_shape_crop = double(1:maxy_image-miny_image+1)';

%% Fill gaps for shape and def

mask_shape = image_shape_crop;

mask_shape(~isnan(mask_shape))=1;
mask_shape(isnan(mask_shape))=0;
```

```

s_shape = regionprops(~mask_shape, 'area', 'PixelList');    %find different area

[~,idx_shape] = sort([s_shape(:).Area], 'descend');
s_shape = s_shape(idx_shape);    %sort structure according to the size of area
from max to min

list_shape = s_shape(1).PixelList;
for i = 1:size(list_shape,1)
    x = list_shape(i,1);
    y = list_shape(i,2);
    mask_shape(y,x) = 1;
end
clear list_shape
s_shape = s_shape(2:end,:);    %remove the first line (max)

mask2_shape = zeros(size(mask_shape));

for i = 1:size(s_shape,1)
    list_shape = s_shape(i).PixelList;
    for j = 1:size(list_shape,1)
        x_shape = list_shape(j,1);
        y_shape = list_shape(j,2);
        value_shape = (image_shape_crop(y_shape-1,x_shape) +
image_shape_crop(y_shape,x_shape-1))/2;
        image_shape_crop(y_shape,x_shape) = value_shape;
    end
    clear list_shape
end

%
mask_shape_tilt = image_shape_tilt_crop;

mask_shape_tilt(~isnan(mask_shape_tilt)) = 1;
mask_shape_tilt(isnan(mask_shape_tilt)) = 0;

s_shape_tilt = regionprops(~mask_shape_tilt, 'area', 'PixelList');    %find
different area

[~,idx_shape_tilt] = sort([s_shape_tilt(:).Area], 'descend');
s_shape_tilt = s_shape_tilt(idx_shape_tilt);    %sort structure according to
the size of area from max to min

list_shape_tilt = s_shape_tilt(1).PixelList;
for i = 1:size(list_shape_tilt,1)
    x = list_shape_tilt(i,1);
    y = list_shape_tilt(i,2);
    mask_shape_tilt(y,x) = 1;
end
clear list_shape_tilt
s_shape_tilt = s_shape_tilt(2:end,:);    %remove the first line (max)

mask2_shape_tilt = zeros(size(mask_shape_tilt));

```

```

for i = 1:size(s_shape_tilt,1)
    list_shape_tilt = s_shape_tilt(i).PixelList;
    for j = 1:size(list_shape_tilt,1)
        x_shape_tilt = list_shape_tilt(j,1);
        y_shape_tilt = list_shape_tilt(j,2);
        value_shape_tilt = (image_shape_tilt_crop(y_shape_tilt-
1,x_shape_tilt)+image_shape_tilt_crop(y_shape_tilt,x_shape_tilt-1))/2;
        image_shape_tilt_crop(y_shape_tilt,x_shape_tilt) = value_shape_tilt;
    end
    clear list_shape_tilt
end

%
mask_def = image_def_crop;

mask_def(~isnan(mask_def)) = 1;
mask_def(isnan(mask_def)) = 0;

s_def = regionprops(~mask_def, 'area', 'PixelList');    %find different area

[~,idx_def] = sort([s_def(:).Area], 'descend');
s_def = s_def(idx_def);    %sort structure according to the size of area from
max to min

list_def = s_def(1).PixelList;
for i = 1:size(list_def,1)
    x_def = list_def(i,1);
    y_def = list_def(i,2);
    mask_def(y_def,x_def) = 1;
end
clear list_def
s_def = s_def(2:end,:);    %remove the first line (max)

mask2_def = zeros(size(mask_def));

for i = 1:size(s_def,1)
    list_def = s_def(i).PixelList;
    for j = 1:size(list_def,1)
        x_def = list_def(j,1);
        y_def = list_def(j,2);
        value_def = (image_def_crop(y_def-1,x_def)+image_def_crop(y_def,x_def-
1))/2;
        image_def_crop(y_def,x_def) = value_def;
    end
    clear list_def
end

%% Filter

H1 = fspecial('disk',10);
H2 = fspecial('disk',10);

```

```

shape_filter = imfilter(image_shape_crop,H1,'replicate');
shape_tilt_filter = imfilter(image_shape_tilt_crop,H1,'replicate');
z_def_filter = imfilter(image_def_crop,H2,'replicate');

%% Interpret measured shape and z-deformation

scalex = (6.7*10^-3)*1.18;
scaley = (6.7*10^-3)*1.18;

lambda_shape = 1.52;    %wavelength in mm  lambda1=780.2nm  lambda2=779.80nm
scalefactor_shape = lambda_shape/(4*pi);
shape = scalefactor_shape*shape_filter;
shape_tilt = scalefactor_shape*shape_tilt_filter;

min_shape = min(min(shape));
shape = shape-min_shape*ones(size(shape));

min_shape_tilt = min(min(shape_tilt));
shape_tilt = shape_tilt-min_shape_tilt*ones(size(shape_tilt));

shape_tilt_pct = (shape_tilt - min(shape_tilt(:))) ./ (max(shape_tilt(:)) -
min(shape_tilt(:)));

lambda_def = 779.80*10^-3;  % um scale
scalefactor_def = lambda_def/(4*pi);
z_def = scalefactor_def*z_def_filter;

x_axis_mm = scalex*X_shape_crop;
y_axis_mm = scaley*Y_shape_crop;

%% Predict x- and y- deformations

% decompositions of normal vectors
[Nx,Ny,Nz] = surfnorm(shape/scalex);

% deformations calculated in x and y directions
UX_def = (Nz).\ (Nx.*z_def);
UY_def = (Nz).\ (Ny.*z_def);

% filter
H1 = fspecial('disk',10);
H2 = fspecial('disk',10);

UX_def_filter = imfilter(UX_def,H1,'replicate');
UY_def_filter = imfilter(UY_def,H2,'replicate');

%% Resultant deformation

```

```

U_res = z_def./Nz;

[Nx_res,Ny_res,Nz_res] = surfnorm(U_res/scalex);

%% Coarse arrow plot

x_coarse = 30;
y_coarse = 30;

[frameH,frameW] = size(U_res);

x_phase_pix = floor(linspace(1,frameW,x_coarse+1));
y_phase_pix = floor(linspace(1,frameH,y_coarse+1));

shape_coarse = zeros(y_coarse,x_coarse);
U_res_coarse = zeros(y_coarse,x_coarse);
Nx_res_coarse = zeros(y_coarse,x_coarse);
Ny_res_coarse = zeros(y_coarse,x_coarse);
Nz_res_coarse = zeros(y_coarse,x_coarse);
x_axis_mm_coarse = zeros(x_coarse,1);
y_axis_mm_coarse = zeros(y_coarse,1);

for i = 1:y_coarse

    for j = 1:x_coarse

        shape_coarse(i,j) = shape(y_phase_pix(i), x_phase_pix(j));
        U_res_coarse(i,j) = U_res(y_phase_pix(i), x_phase_pix(j));
        Nx_res_coarse(i,j) = Nx_res(y_phase_pix(i), x_phase_pix(j));
        Ny_res_coarse(i,j) = Ny_res(y_phase_pix(i), x_phase_pix(j));
        Nz_res_coarse(i,j) = Nz_res(y_phase_pix(i), x_phase_pix(j));
        x_axis_mm_coarse(j) = x_axis_mm(x_phase_pix(j));

    end

    y_axis_mm_coarse(i) = y_axis_mm(y_phase_pix(i));

end

[qx_phase,qy_phase] = meshgrid(x_axis_mm_coarse,y_axis_mm_coarse);

figure
quiver3(qx_phase,qy_phase,U_res_coarse,Nx_res_coarse,Ny_res_coarse,Nz_res_coar
se);
hold on
mesh(x_axis_mm, y_axis_mm, U_res);
colormap Jet
hold off
xlabel('x (mm)');ylabel('y (mm)');zlabel('z (um)');

```

```

grid off

%% Only horizontal and vertical curves

% Horizontal-- fix y

central_num_y = floor(length(Y_shape_crop)/2);

shape_horiz_y = shape(central_num_y,:);
z_def_horiz_y = z_def(central_num_y,:);
UX_def_horiz_y = UX_def(central_num_y,:);
UY_def_horiz_y = UY_def(central_num_y,:);

shape_horiz_y = shape_horiz_y';
z_def_horiz_y = z_def_horiz_y';
UX_def_horiz_y = UX_def_horiz_y';
UY_def_horiz_y = UY_def_horiz_y';

shape_horiz_y_ind = find(~isnan(shape_horiz_y));
z_def_horiz_y_ind = find(~isnan(z_def_horiz_y));
UX_def_horiz_y_ind = find(~isnan(UX_def_horiz_y));
UY_def_horiz_y_ind = find(~isnan(UY_def_horiz_y));

horiz_min_ind = min(UX_def_horiz_y_ind);
horiz_max_ind = max(UX_def_horiz_y_ind);

shape_horiz_densey = shape_horiz_y(horiz_min_ind:horiz_max_ind);
z_def_horiz_densey = z_def_horiz_y(horiz_min_ind:horiz_max_ind);
UX_def_horiz_densey = UX_def_horiz_y(horiz_min_ind:horiz_max_ind);
UY_def_horiz_densey = UY_def_horiz_y(horiz_min_ind:horiz_max_ind);

x_horiz_ind = double(1:length(shape_horiz_densey))';

p_shape_horiz = polyfit(x_horiz_ind,shape_horiz_densey,10);
f_shape_horiz = polyval(p_shape_horiz,x_horiz_ind);

p_z_def_horiz = polyfit(x_horiz_ind,z_def_horiz_densey,10);
f_z_def_horiz = polyval(p_z_def_horiz,x_horiz_ind);

p_UX_def_horiz = polyfit(x_horiz_ind,UX_def_horiz_densey,10);
f_UX_def_horiz = polyval(p_UX_def_horiz,x_horiz_ind);

p_UY_def_horiz = polyfit(x_horiz_ind,UY_def_horiz_densey,10);
f_UY_def_horiz = polyval(p_UY_def_horiz,x_horiz_ind);

% Vertical-- fix x

central_num_x = floor(length(X_shape_crop)/2);

```

```

shape_verti_x = shape(:,central_num_x);
z_def_verti_x = z_def(:,central_num_x);
UX_def_verti_x = UX_def(:,central_num_x);
UY_def_verti_x = UY_def(:,central_num_x);

shape_verti_x_ind = find(~isnan(shape_verti_x));
z_def_verti_x_ind = find(~isnan(z_def_verti_x));
UX_def_verti_x_ind = find(~isnan(UX_def_verti_x));
UY_def_verti_x_ind = find(~isnan(UY_def_verti_x));

verti_min_ind = min(UX_def_verti_x_ind);
verti_max_ind = max(UX_def_verti_x_ind);

shape_verti_densex = shape_verti_x(verti_min_ind:verti_max_ind);
z_def_verti_densex = z_def_verti_x(verti_min_ind:verti_max_ind);
UX_def_verti_densex = UX_def_verti_x(verti_min_ind:verti_max_ind);
UY_def_verti_densex = UY_def_verti_x(verti_min_ind:verti_max_ind);

y_verti_ind = double(1:length(shape_verti_densex))';

p_shape_verti = polyfit(y_verti_ind,shape_verti_densex,10);
f_shape_verti = polyval(p_shape_verti,y_verti_ind);

p_z_def_verti = polyfit(y_verti_ind,z_def_verti_densex,10);
f_z_def_verti = polyval(p_z_def_verti,y_verti_ind);

p_UX_def_verti = polyfit(y_verti_ind,UX_def_verti_densex,10);
f_UX_def_verti = polyval(p_UX_def_verti,y_verti_ind);

p_UY_def_verti = polyfit(y_verti_ind,UY_def_verti_densex,10);
f_UY_def_verti = polyval(p_UY_def_verti,y_verti_ind);

length_horiz = scalex*x_horiz_ind;
length_verti = scaley*y_verti_ind;

%%

figure
warp(x_axis_mm, y_axis_mm, shape, shape_tilt_pct)
colormap('jet');
grid on
xlabel('x (mm)');ylabel('y (mm)');zlabel('z (mm)');
axis equal

figure
subplot(2,2,1) % measured shape
mesh (x_axis_mm, y_axis_mm, U_res);

```

```

set(findobj('Type','patch'),'LineStyle','none');
title('Resultant def','FontSize',14,'FontWeight','bold');
xlabel('x (mm)');ylabel('y (mm)');zlabel('z (um)');
colormap Jet

subplot(2,2,2)
mesh(x_axis_mm, y_axis_mm, z_def)
set(findobj('Type','patch'),'LineStyle','none');
title('Z def','FontSize',14,'FontWeight','bold');
xlabel('x (mm)');ylabel('y (mm)');zlabel('z (um)');
colormap Jet

subplot(2,2,3)
mesh(x_axis_mm, y_axis_mm, UX_def_filter)
set(findobj('Type','patch'),'LineStyle','none');
title('X-def prediction','FontSize',14,'FontWeight','bold');
xlabel('x (mm)');ylabel('y (mm)');zlabel('x (um)');
colormap Jet

subplot(2,2,4)
mesh(x_axis_mm, y_axis_mm, UY_def_filter)
set(findobj('Type','patch'),'LineStyle','none');
title('Y-def prediction','FontSize',14,'FontWeight','bold');
xlabel('x (mm)');ylabel('y (mm)');zlabel('y (um)');
colormap Jet

% horizontal plot--y is fixed

figure
subplot(2,2,1)
plot(length_horiz,f_shape_horiz);
xlabel('Horizontal (mm)');ylabel('(mm)');
title('Measured shape','FontSize',14,'FontWeight','bold');

subplot(2,2,2)
plot(length_horiz,f_z_def_horiz);
xlabel('(mm)');ylabel('z (um)');
title('Measured z def','FontSize',14,'FontWeight','bold');

subplot(2,2,3)
plot(length_horiz,f_UX_def_horiz);
xlabel('(mm)');ylabel('x (um)');
title('Predicted x def','FontSize',14,'FontWeight','bold');

subplot(2,2,4)
plot(length_horiz,f_UY_def_horiz);
xlabel('(mm)');ylabel('y (um)');
title('Predicted y def','FontSize',14,'FontWeight','bold');

% Vertical plot--x is fixed

figure

```

```
subplot(2,2,1)
plot(length_verti,f_shape_verti);
xlabel('Vertical (mm)');ylabel('(mm)');
title('Measured shape','FontSize',14,'FontWeight','bold');

subplot(2,2,2)
plot(length_verti,f_z_def_verti);
xlabel('(mm)');ylabel('z (um)');
title('Measured z def','FontSize',14,'FontWeight','bold');

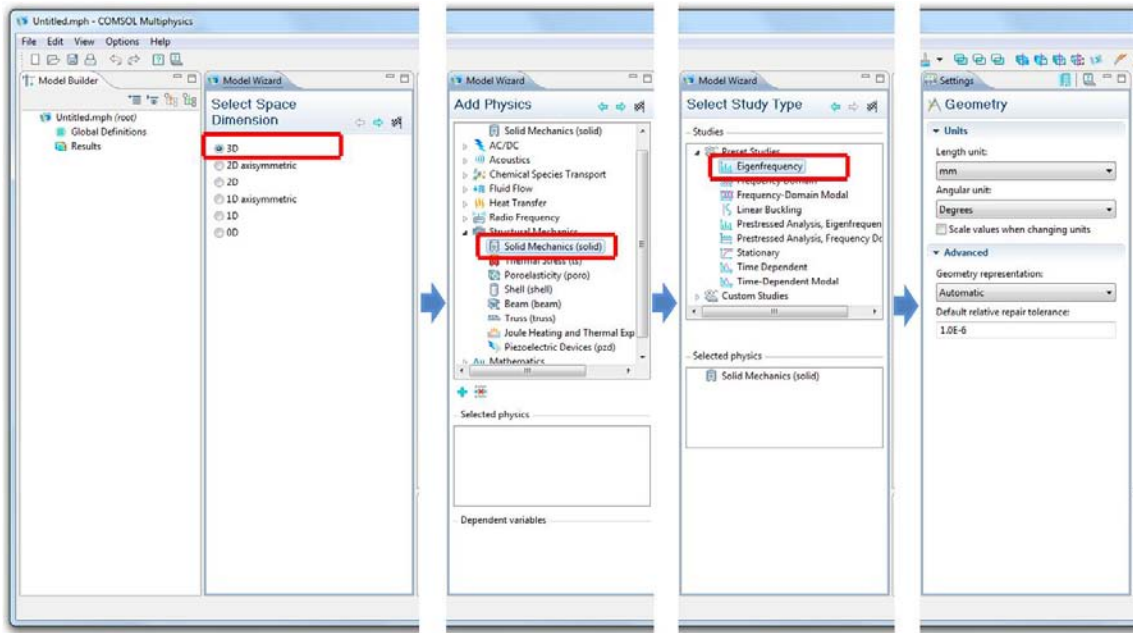
subplot(2,2,3)
plot(length_verti,f_UX_def_verti);
xlabel('(mm)');ylabel('x (um)');
title('Predicted x def','FontSize',14,'FontWeight','bold');

subplot(2,2,4)
plot(length_verti,f_UY_def_verti);
xlabel('(mm)');ylabel('y (um)');
title('Predicted y def','FontSize',14,'FontWeight','bold');
```

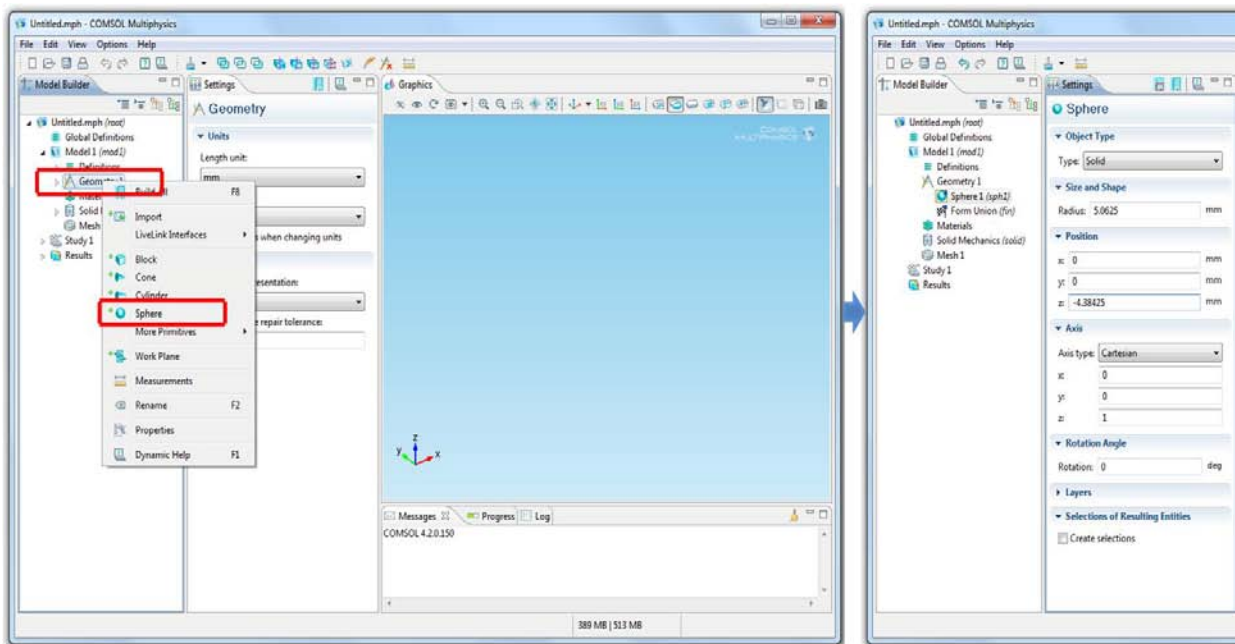
APPENDIX C: COMSOL Multiphysics (V4.2a) Vibration simulation procedure

A procedure for Eigen-frequency analysis of a spherical-shape thin shell is demonstrated.

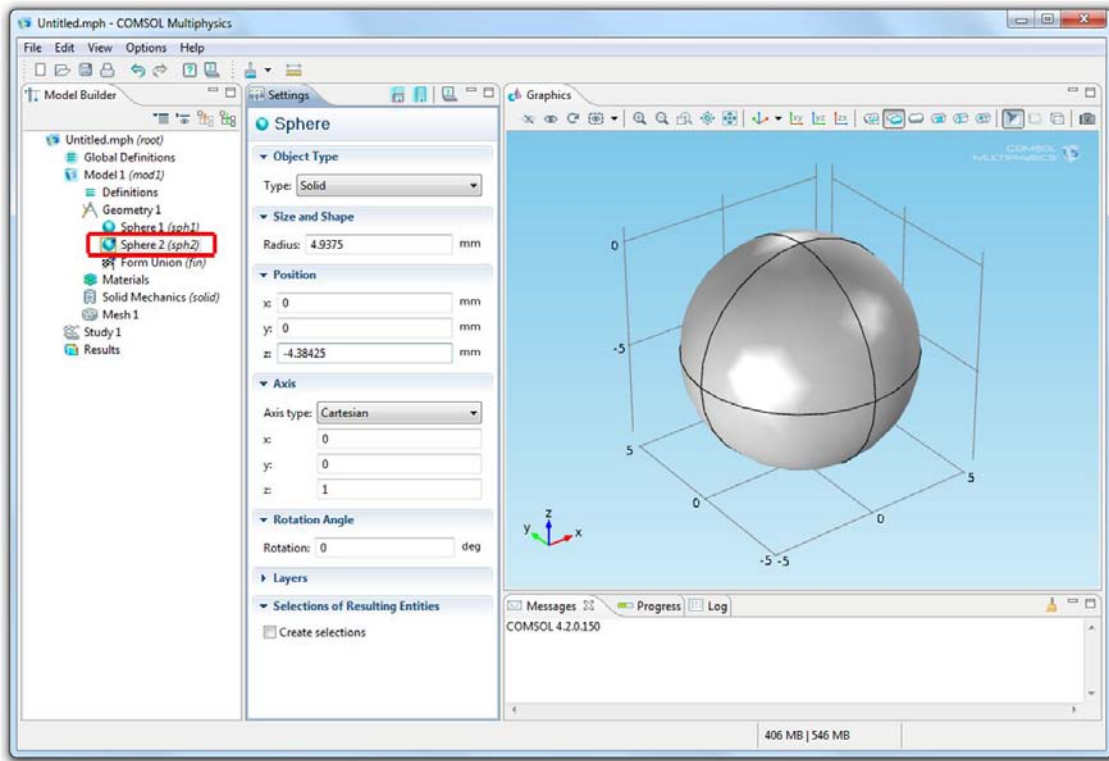
1. Start COMSOL Multiphysics 4.2a: in “Model Wizard” section, select space dimension (3D), add physics (solid mechanics), and select study type (eigenfrequency); in settings, select the unit of geometry.



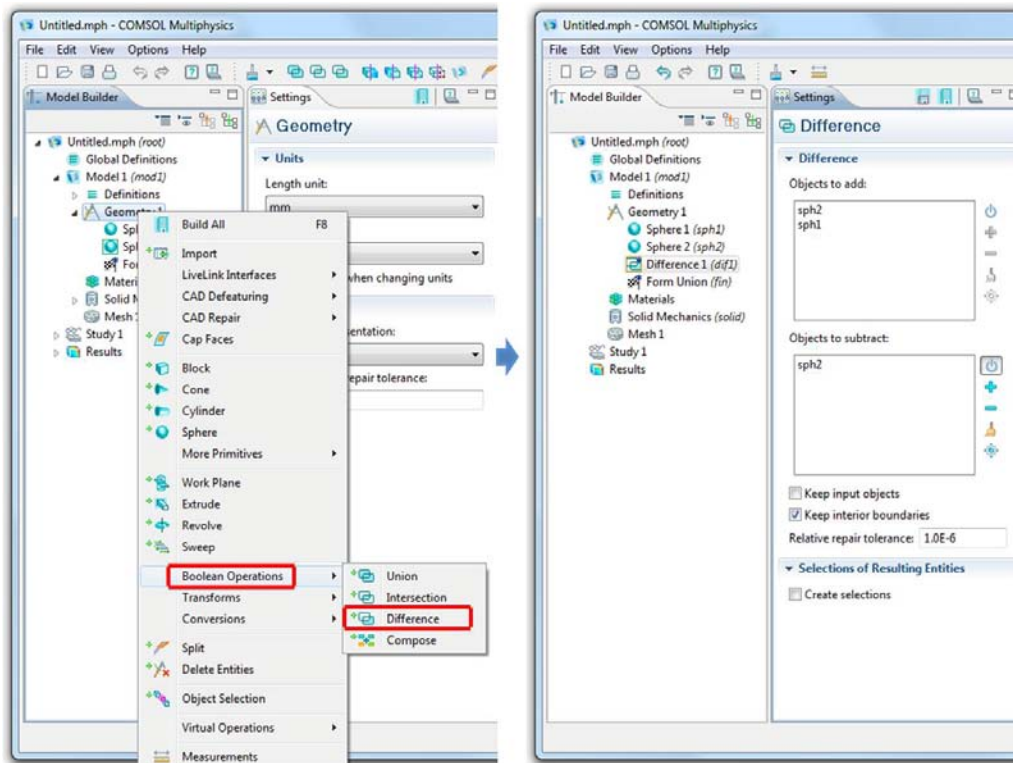
2. To build geometry, select “sphere” as the model and then set the dimensions.



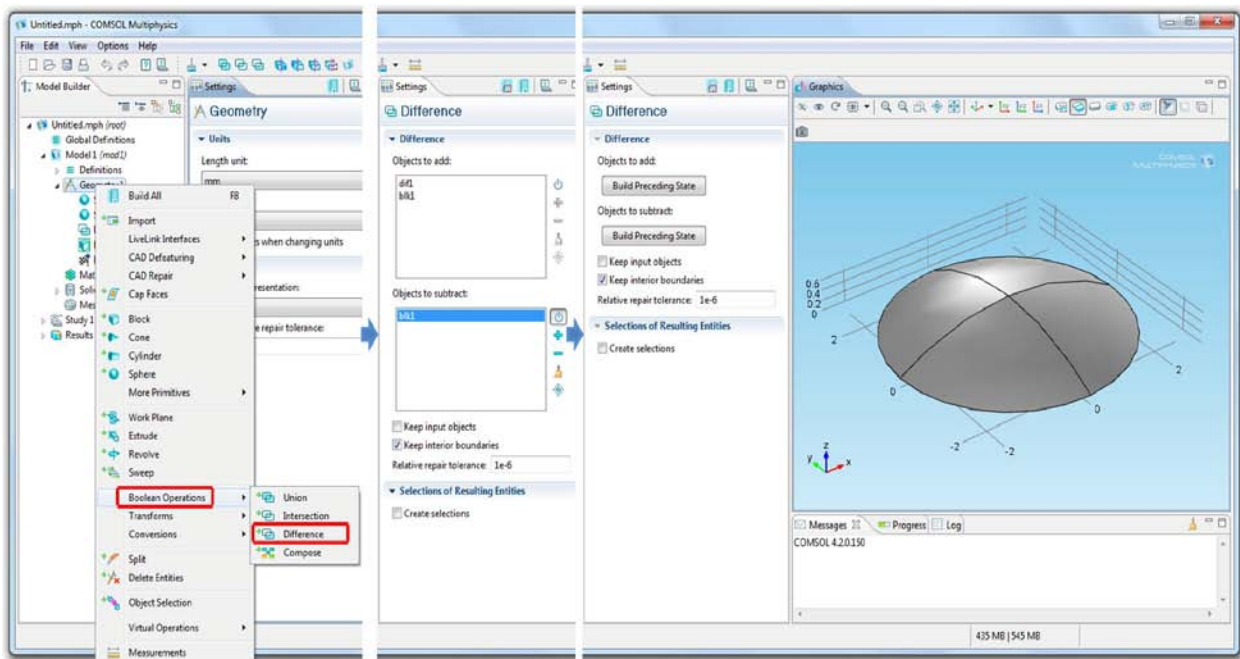
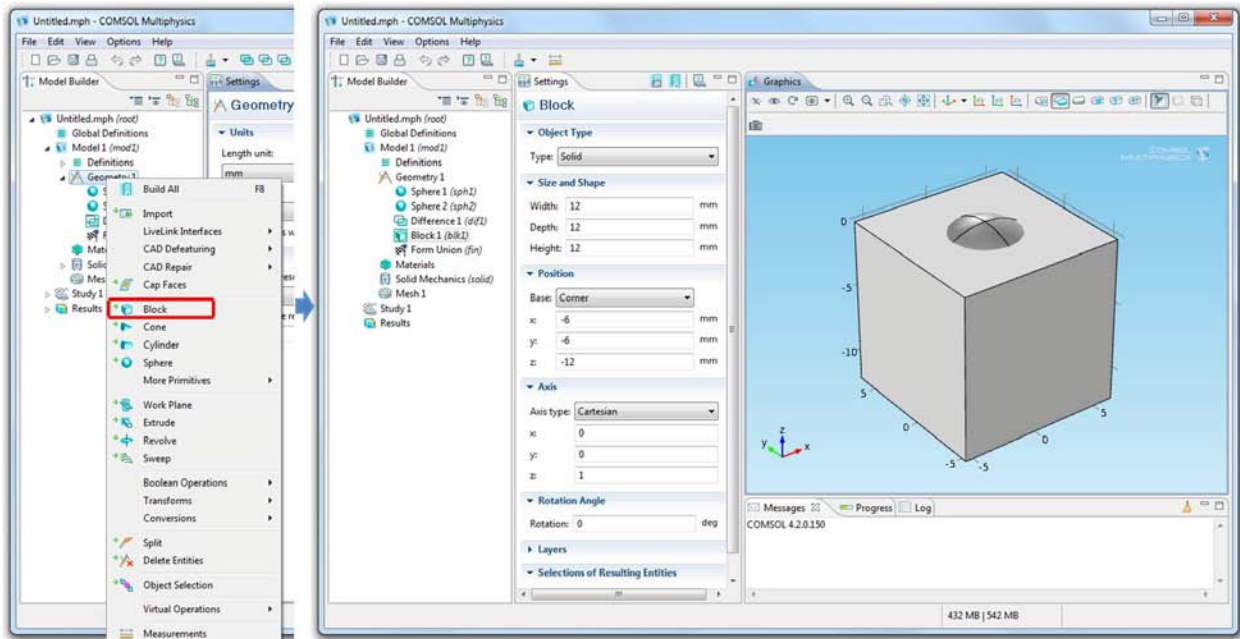
3. Build “sphere 2” in “Model Builder” and set the dimensions.



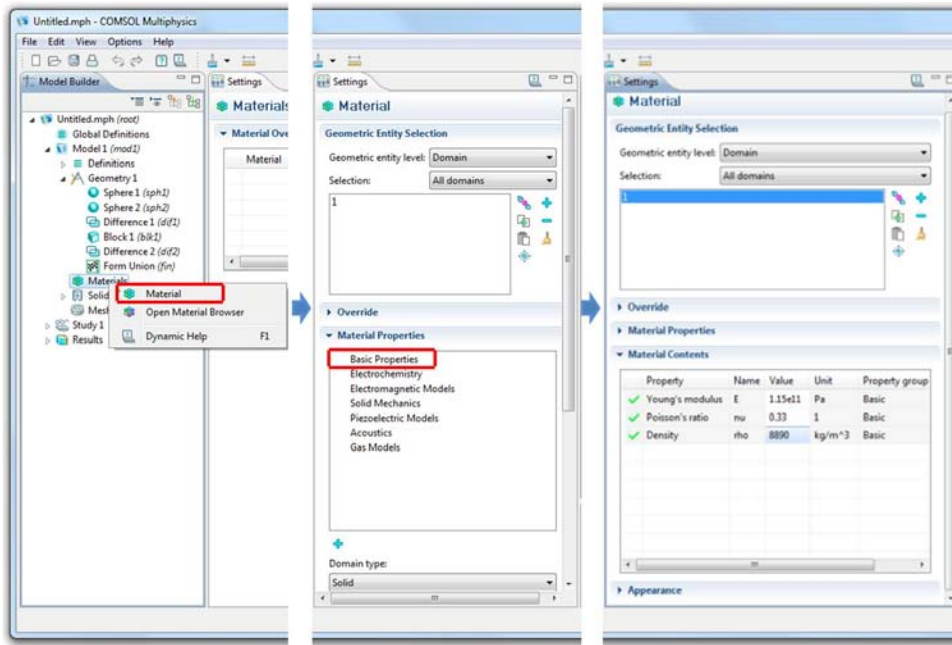
4. In the drop-down menu of “Geometry”, “Difference” in “Boolean Operations” is utilized to obtain a thin-shell shape. Then select the objects.



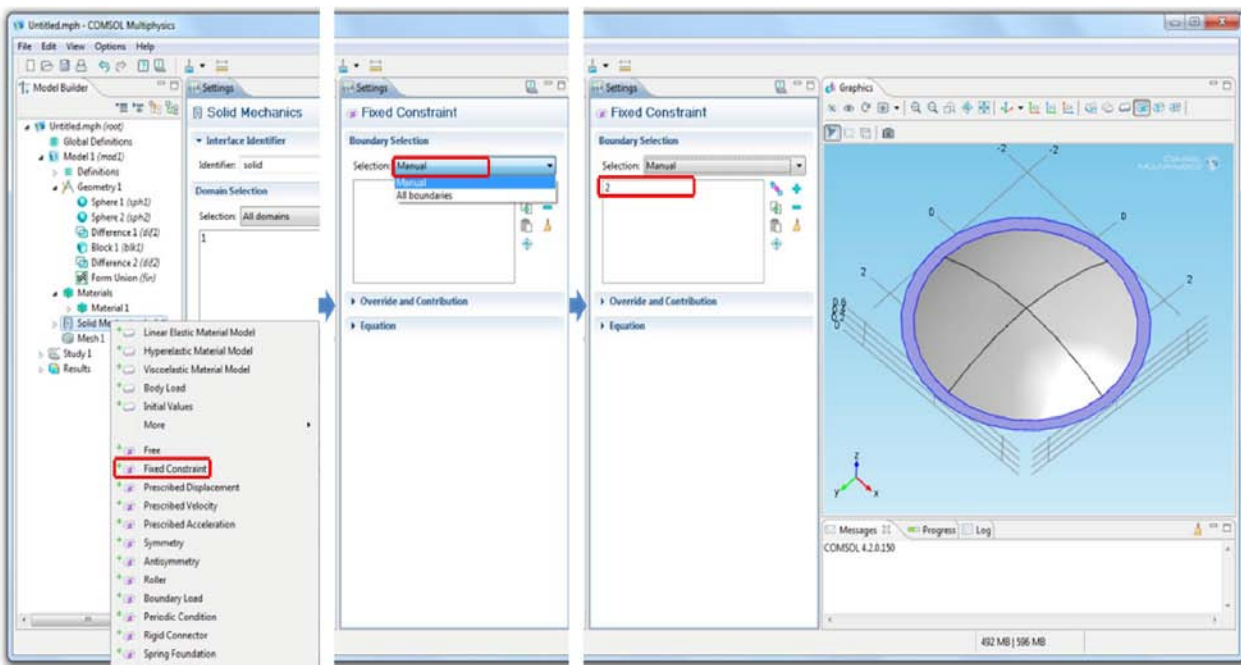
5. Build a “Block” in Geometry, set dimensions and utilize “Difference” in “Boolean Operations” to obtain a partial spherical thin shell which is the difference between the spherical ball and the block. Until now, the task of the creation of the object is completed.



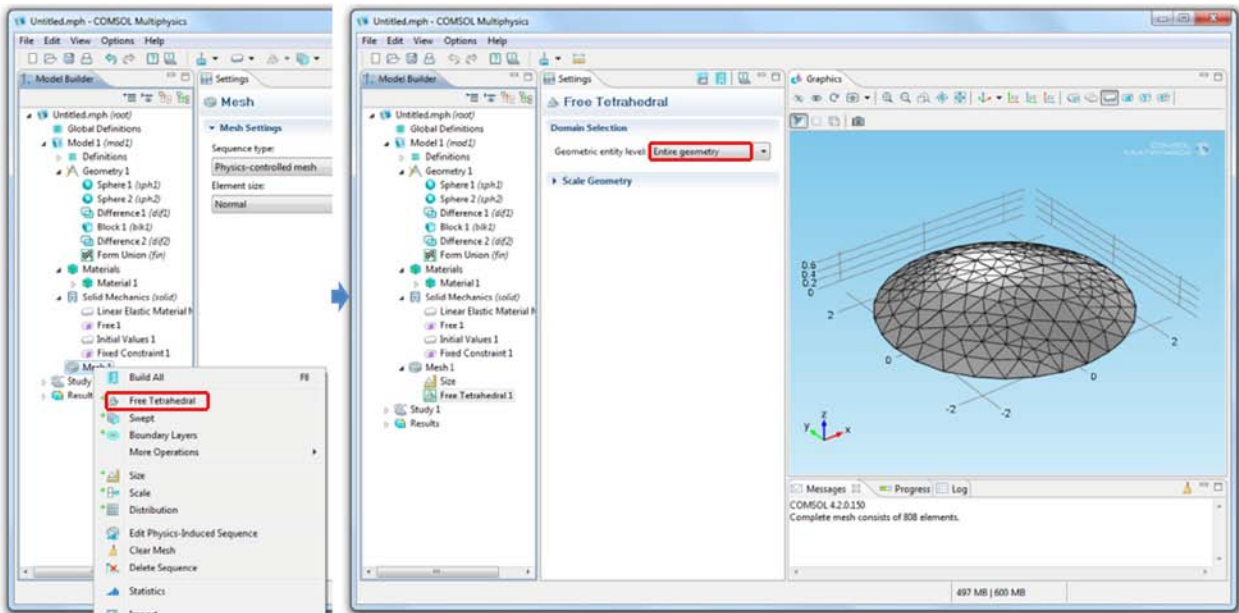
- The next step is to define the material properties of the object. In the setting of “Material”, edit the “Basic Properties” by means of Young’s modulus, Poisson’s ratio and Density. Material can be selected from COMSOL library or defined by the users.



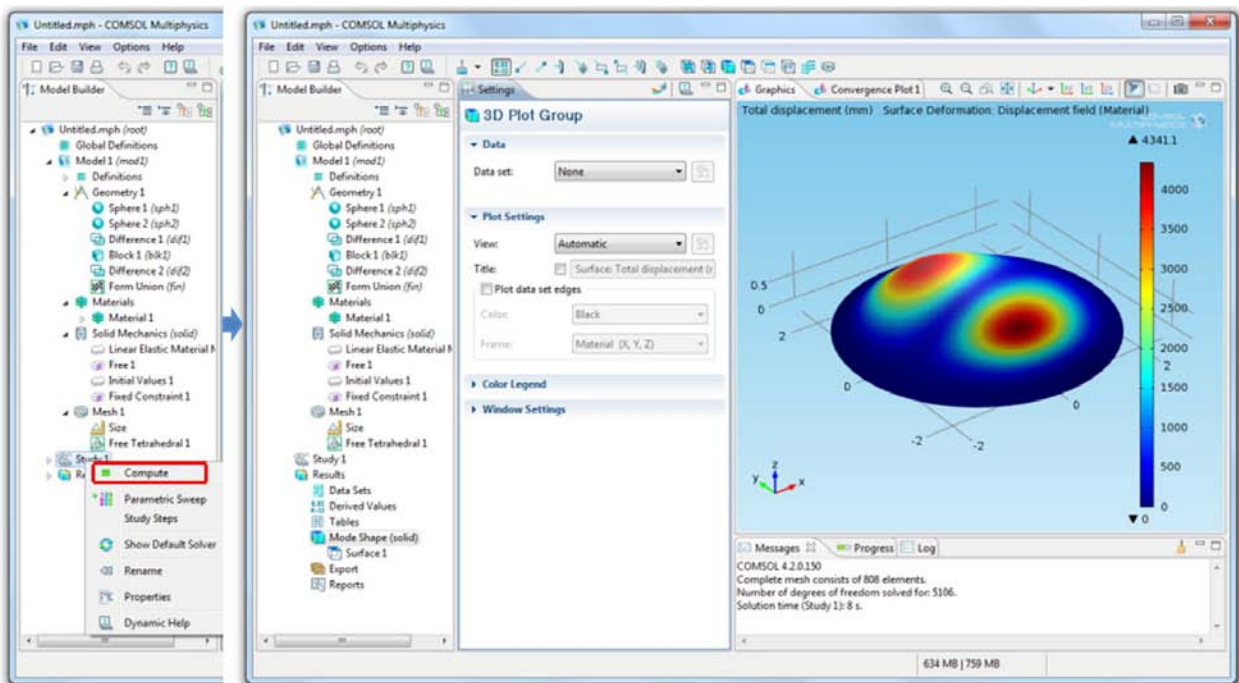
- Then the next step is to define the boundary conditions. In the drop-down menu of “Solid Mechanics”, select “Fixed Constraint”. Set the selection method as “Manual”, and then select the boundary that needs to be fixed.



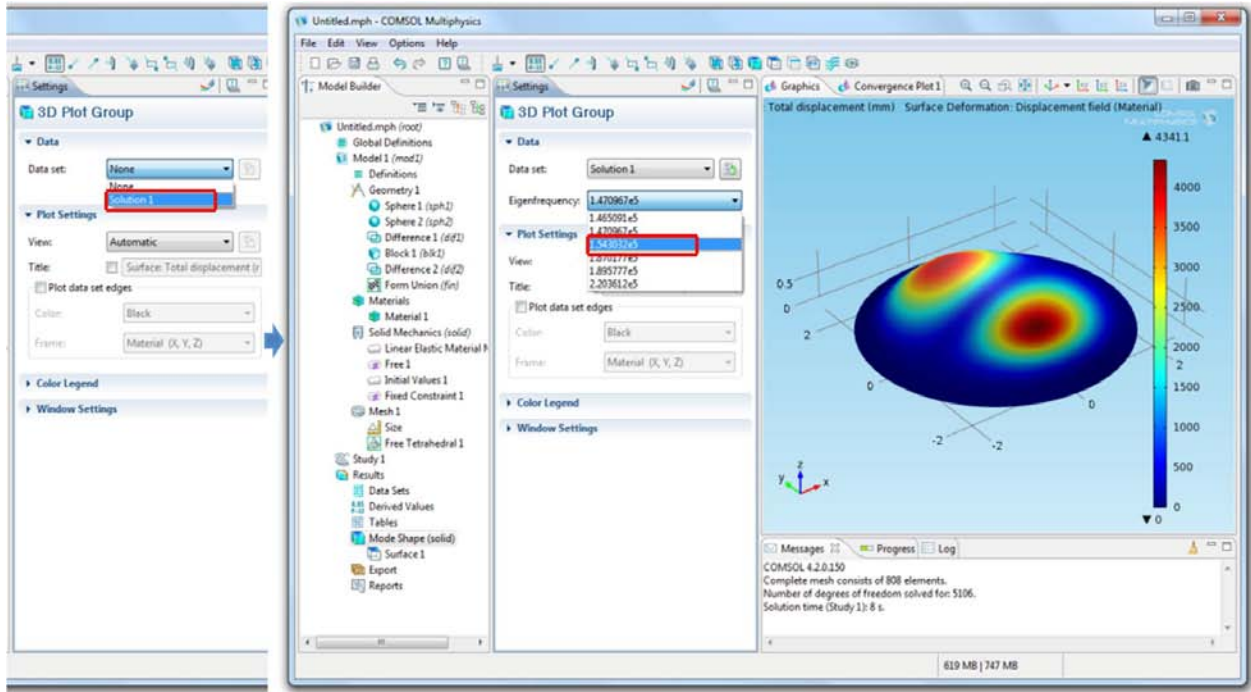
8. A very crucial step is “Mesh”. Right click on “Mesh” in the “Model Builder” menu, select “Free Tetrahedral” to generate mesh by default. In other options, the user can define the geometry of mesh and mesh parameters. In “Free Tetrahedral” window, select the “Entire geometry” as the mesh domain.



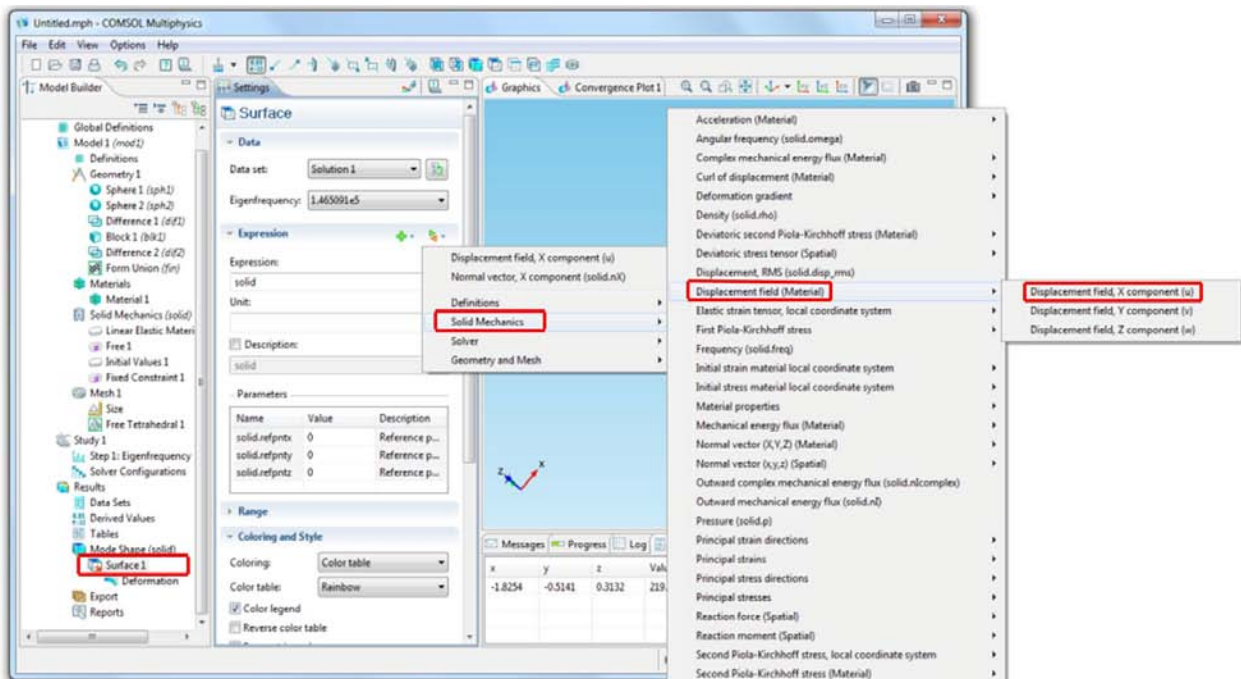
9. To solve the problem, go to “Study 1”, select “Compute”. Then a 3D plot of the surface displacement at a vibration mode is generated.

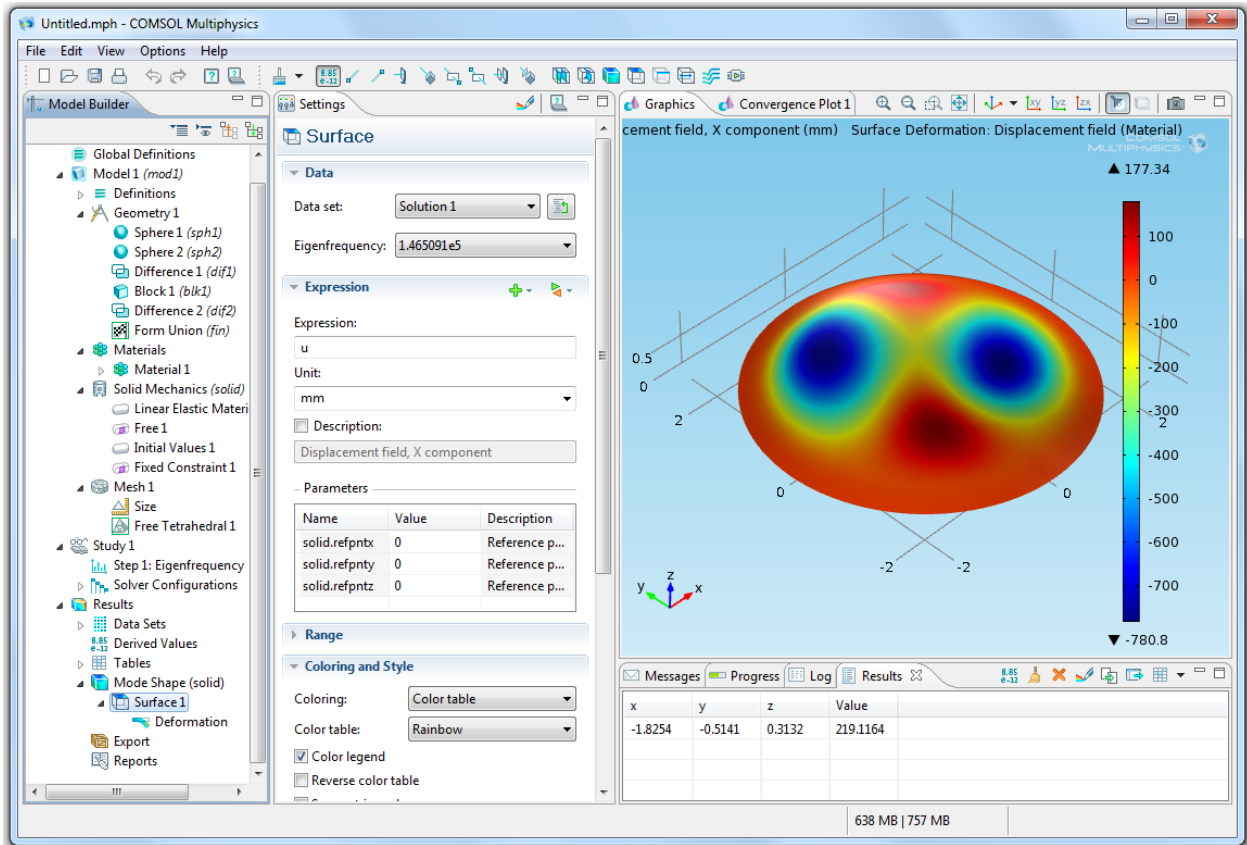


10. In “3D Plot Group” window, select the solution, and then select the mode in “Eigenfrequency” that you want to plot. By default, it plots the resultant displacement.



11. In order to generate decompositions of the resultant frequency displacement in x, y and z axes, go to “Surface”, in the drop-down menu of “Expression” select “Solid Mechanics”. Then go to “Displacement field”, select “Displacement field X component” or others.

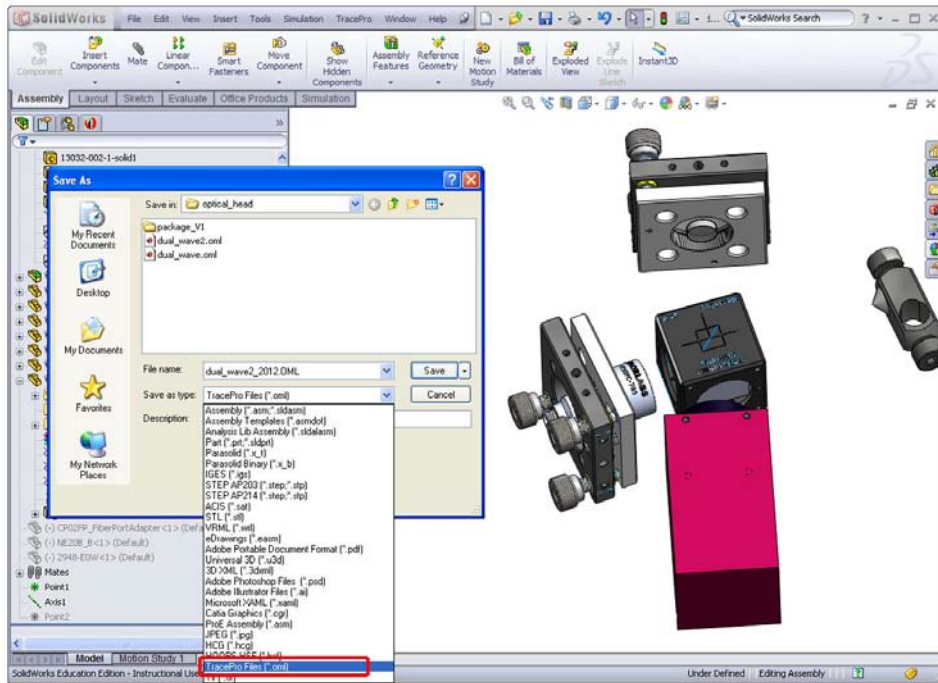




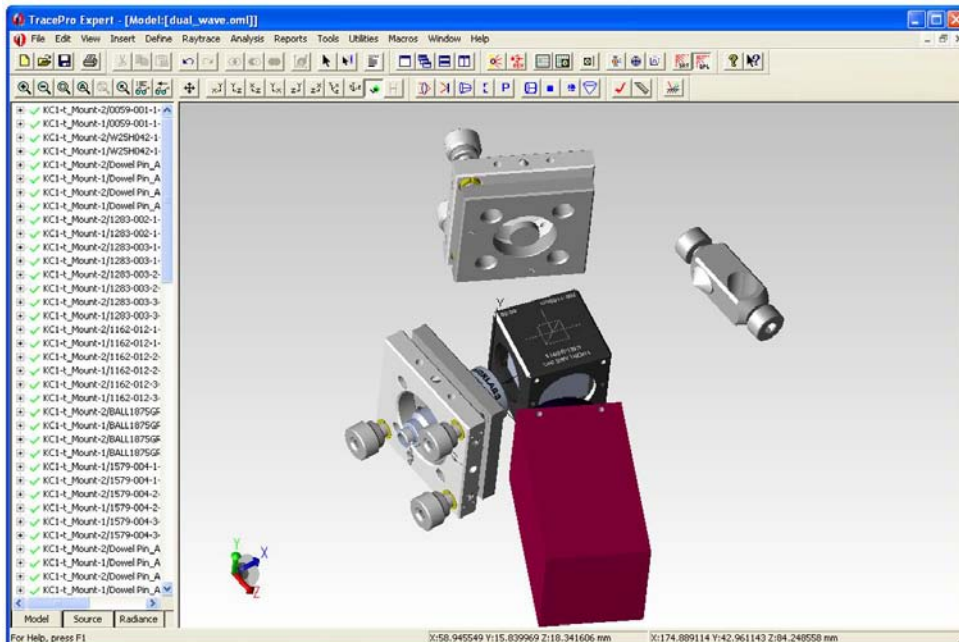
APPENDIX D: Optical ray tracing simulations of OH by Tracepro software

A step by step procedure of optical ray tracing simulation for validating the angles between different optical components in Tracepro are shown as follows:

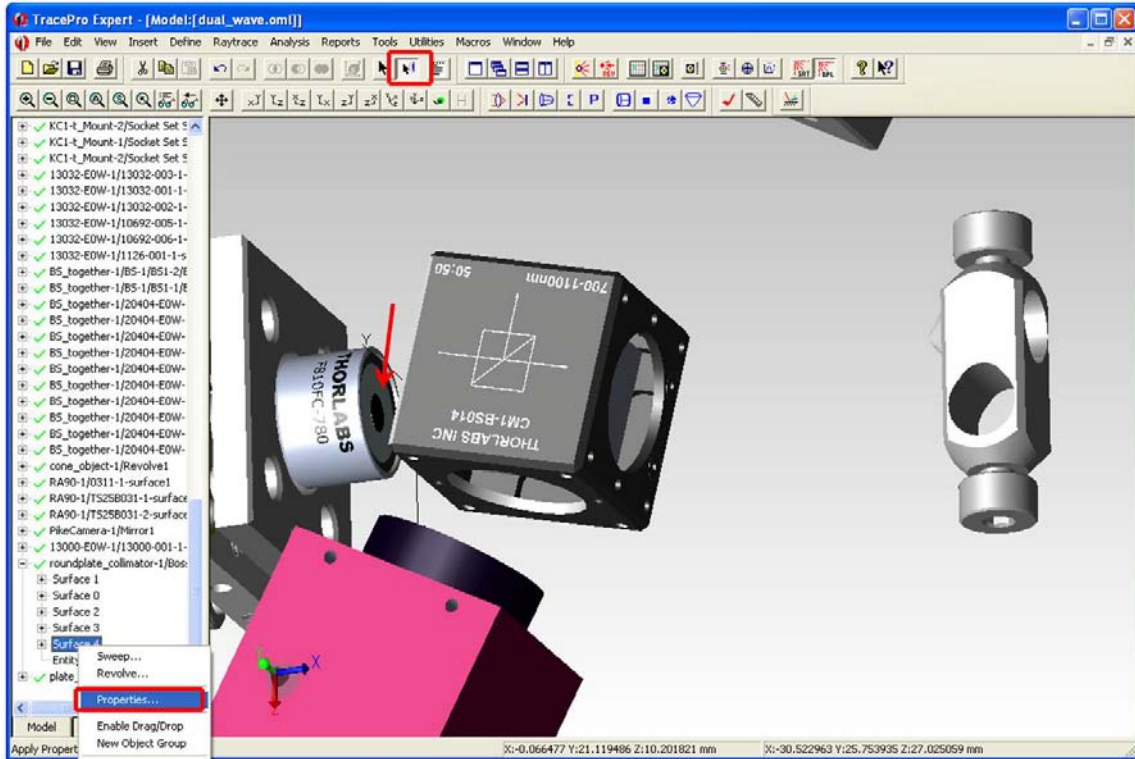
1. In order to import CAD model to Tracepro, add in “Tracepro” module in Solidworks and then save the file to “.oml” format.



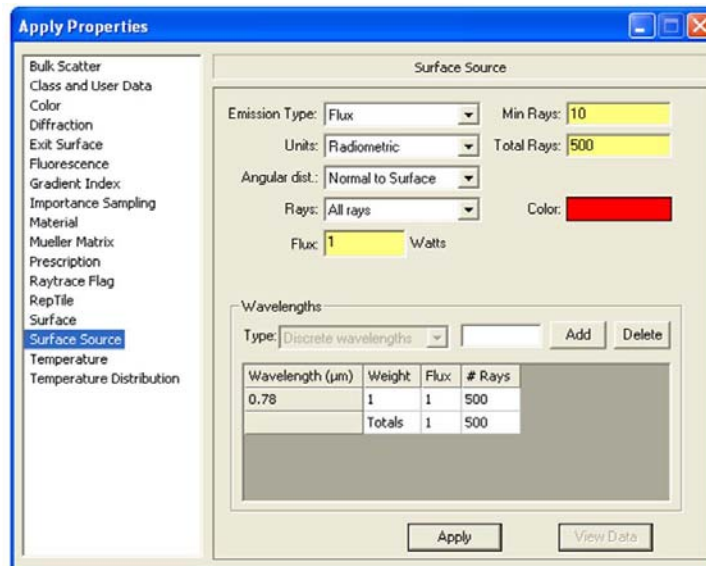
2. Launch Tracpro software, and open the saved CAD model file.



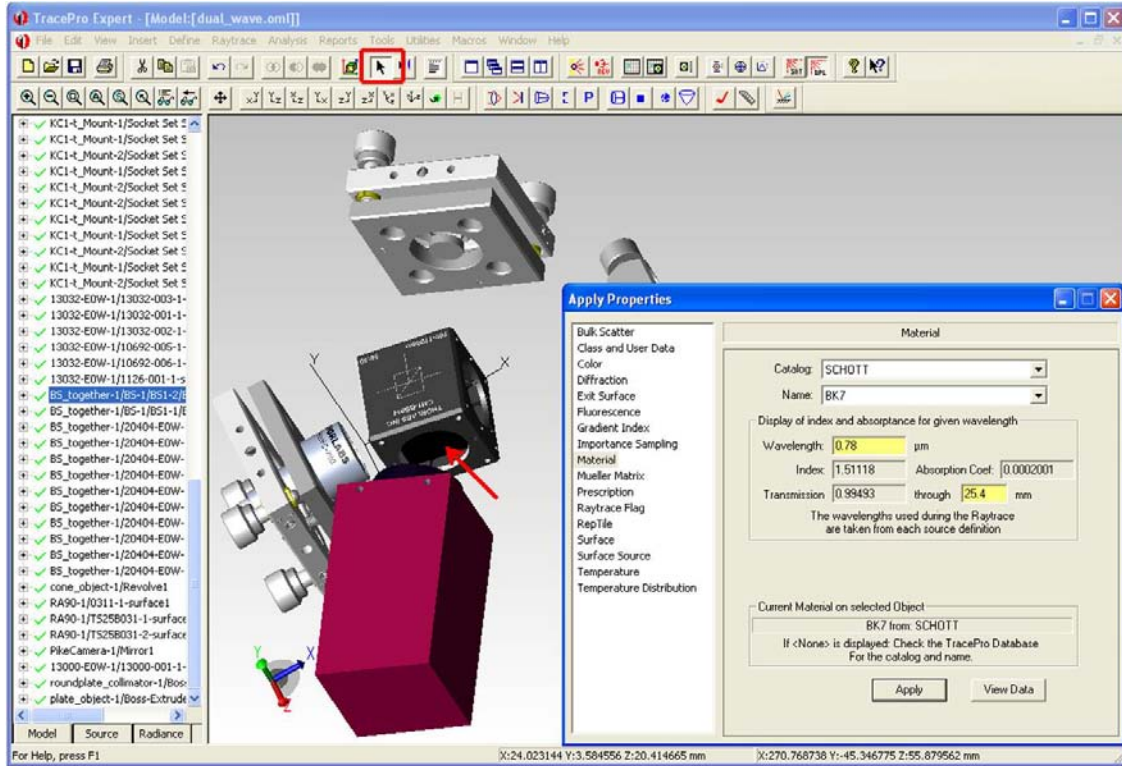
- In order to perform light intensity distribution in ray tracing simulation, optical properties of each component that is located in the optical path need to be specified. The first step is to define the surface source. Select the button “Selcet surface” in toolbar, and click on the outside surface of the colimator. If the object is select, the color will turn to black. In the model tree, right click the select surfsce and select “Properties”.



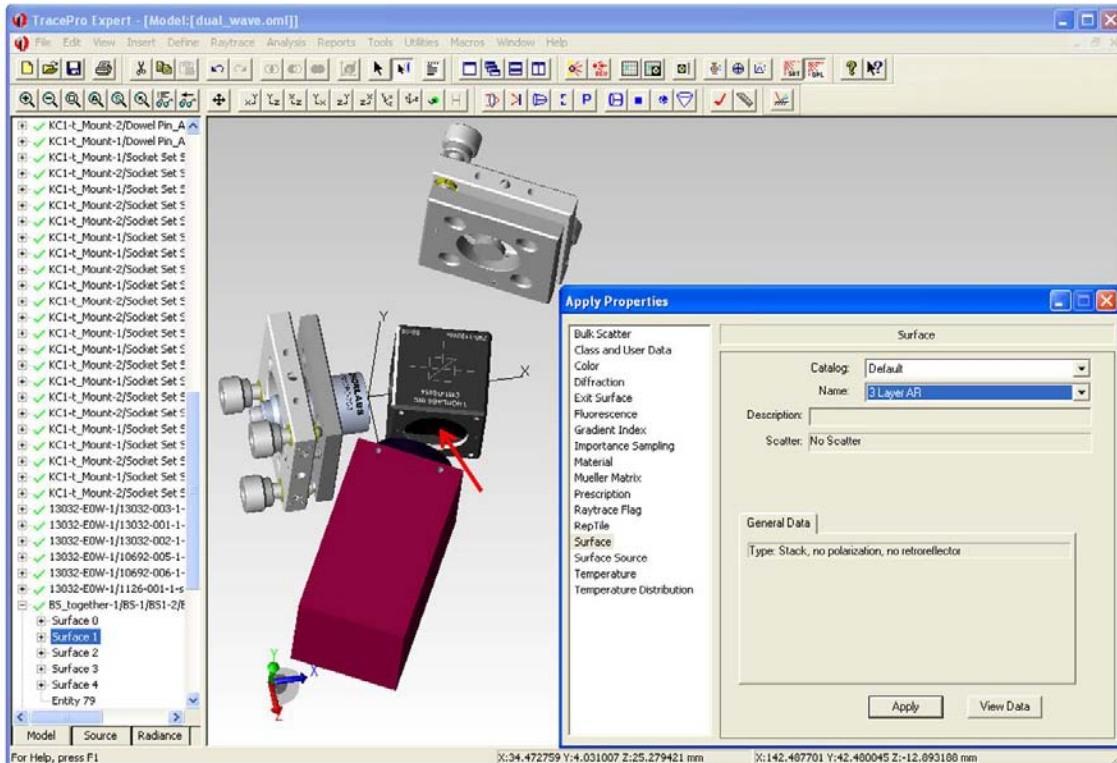
Then specify the light’s power, wavelength and ray volume.



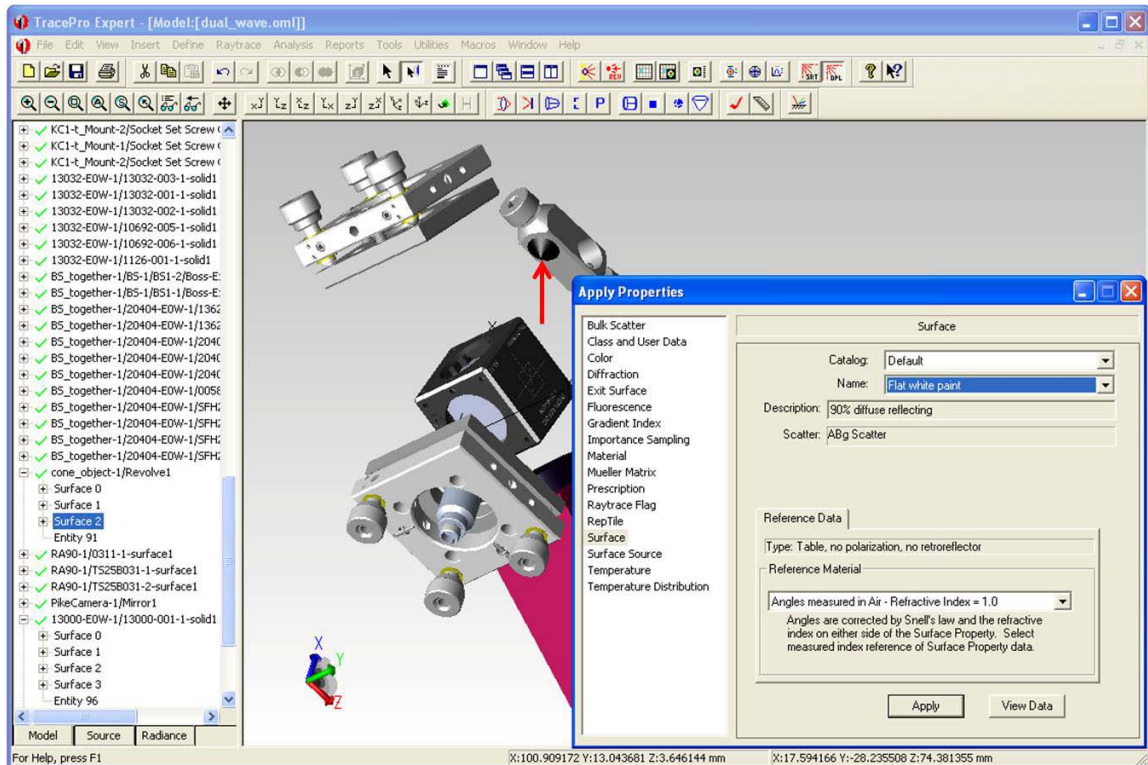
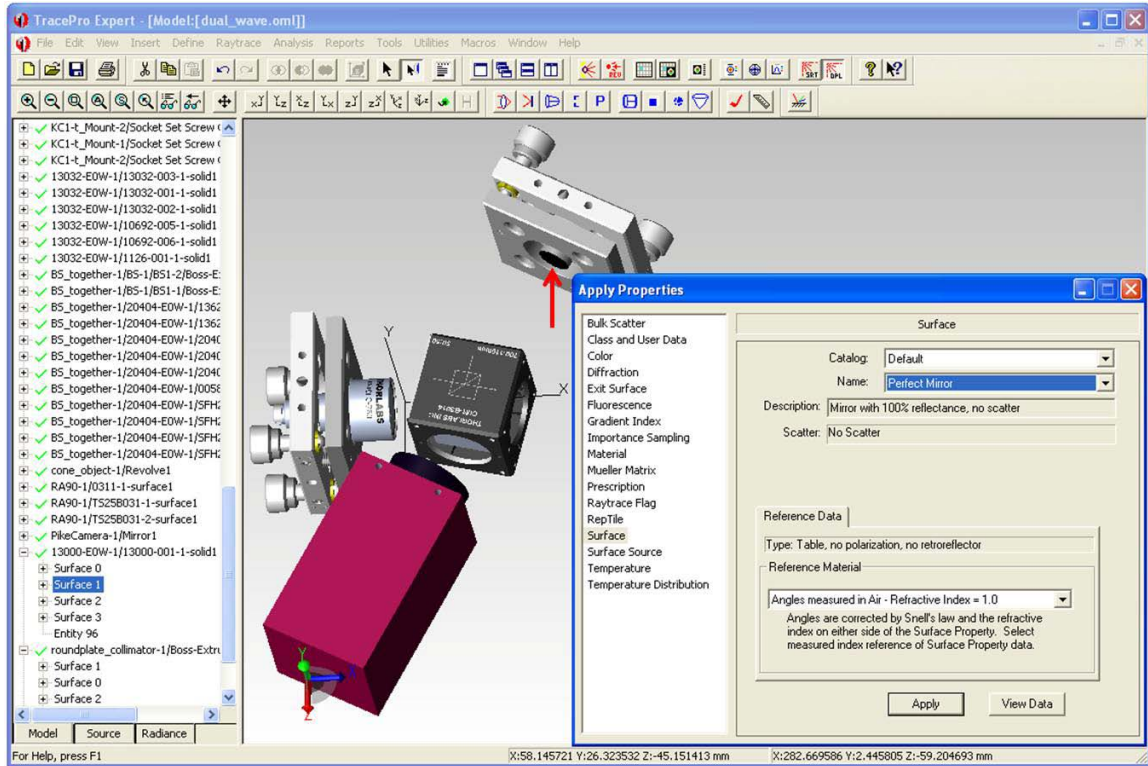
- Select the beamsplitter cube by the “Select object” cursor. Right click the object in model tree and select “Properties”. Define the “Material” properties of this beamsplitter cube.



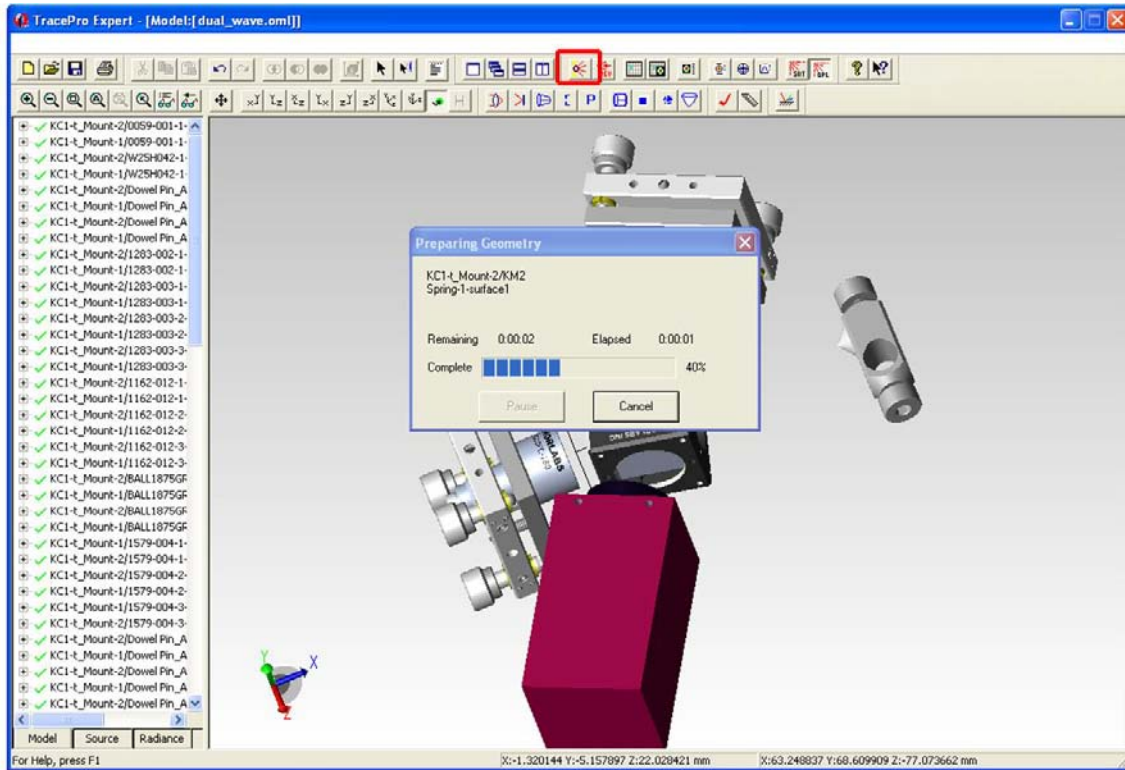
- Define the “Surface” type as “3 Layer AR” for the surfaces of this beamsplitter cube.



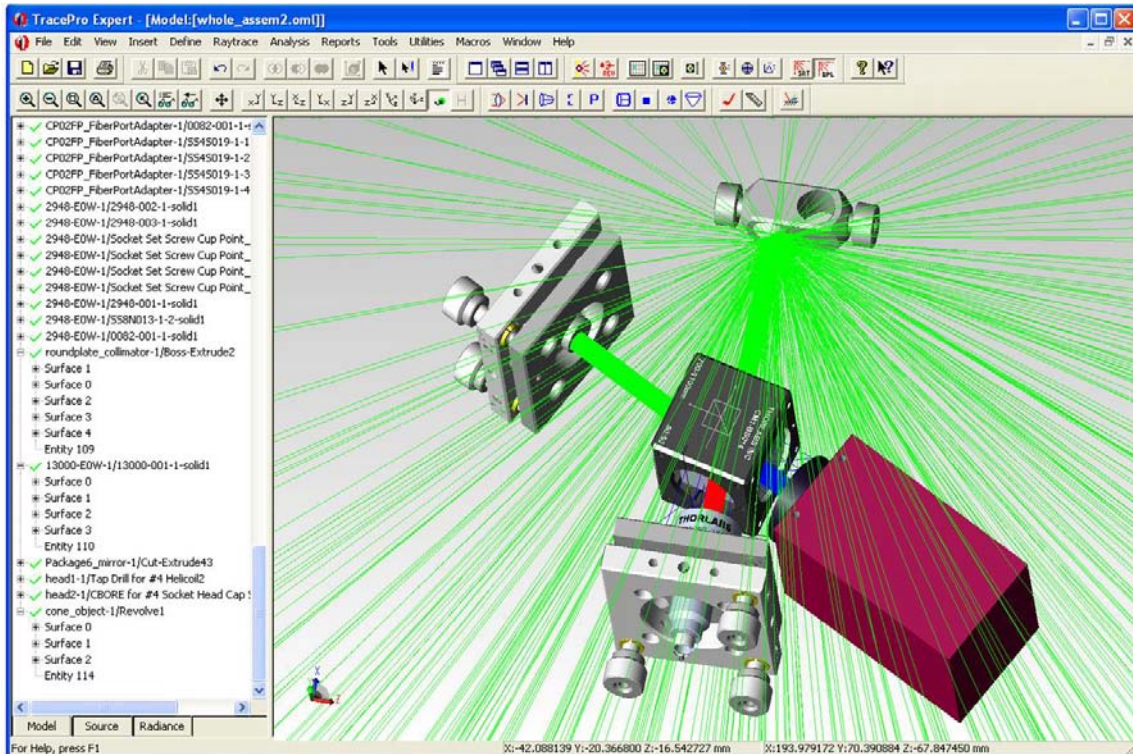
- Use the same method to define the surface type of the select mirror as “Perfect Mirror” and the tested object as “Flat white paint”.



7. The next step is to start the simulation. Click on “Trace Rays” button in Toolbar.



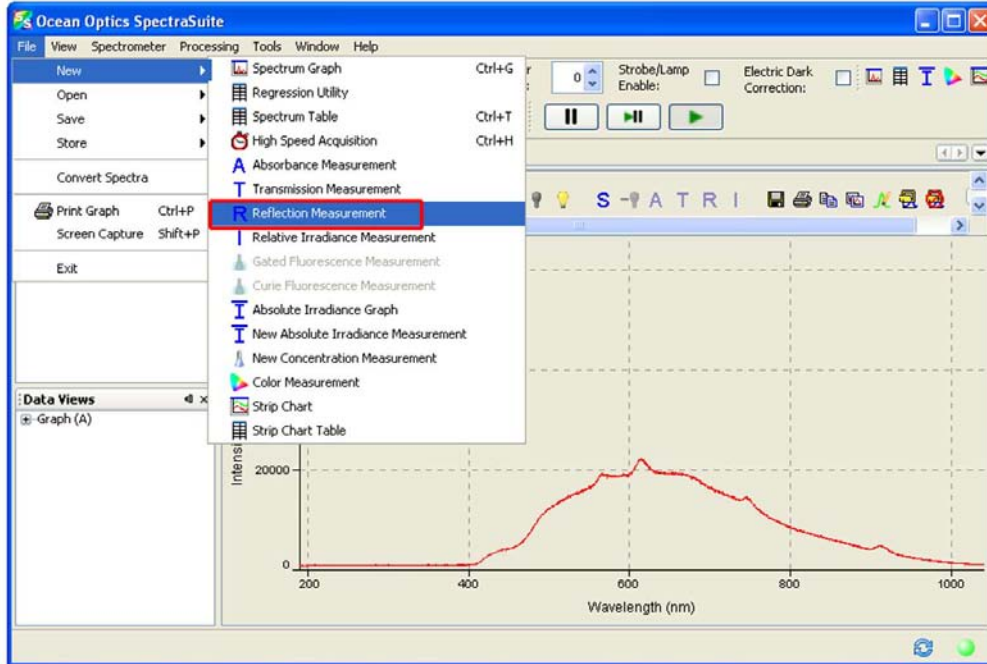
After a while, the light intensity distribution is plotted and is marked as different color. Light intensity is decreasing as the following order: red→green→blue.



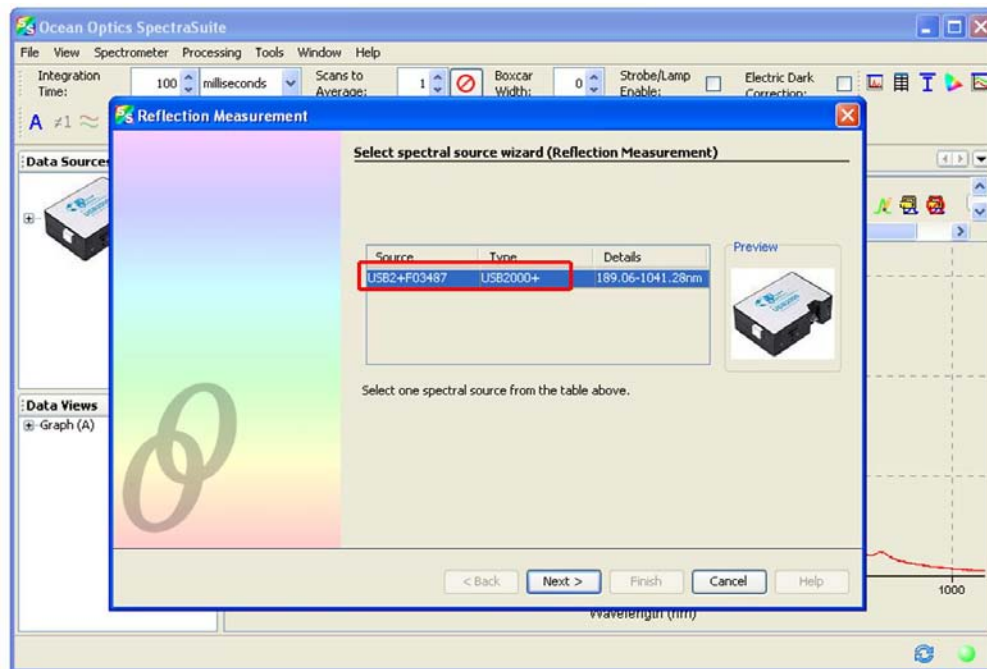
APPENDIX E: Spectroscopic analysis by Ocean Optics Spectrometer

Reflection measurements are performed by Ocean Optics Spectrometer (USB2000+XR) by using SpectraSuite as the following steps:

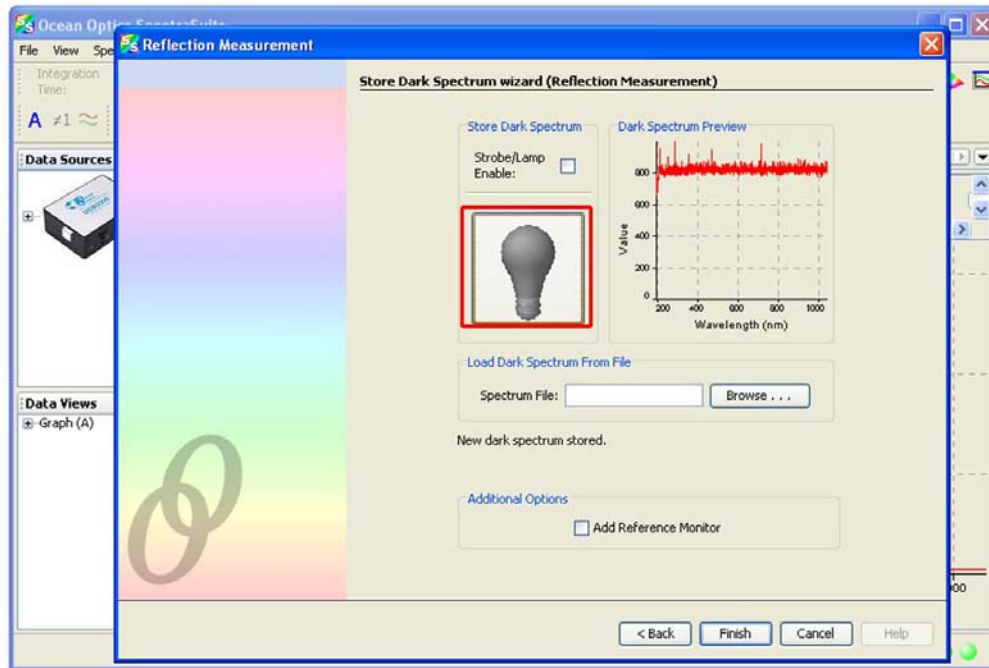
1. Start SpectraSuite, go to “File”→ “New” ”→ “Reflection Measurement”.



2. Make sure the spectrometer is highlighted in blue, and then click on “Next”.



5. Block the light path, and then take a dark spectrum by clicking on the gray light bulb. Click on “Next”.



6. Place the light source onto the tested target. Then the reflection graph is shown in the window.

